



UNIVERSIDADE ESTADUAL DE CAMPINAS

Faculdade de Engenharia Química

MAURO JUNIOR AIRES DE OLIVEIRA

MODELAGEM MATEMÁTICA E SIMULAÇÃO NUMÉRICA DE
REATORES DE LEITO FLUIDIZADO BORBULHANTE E
INCORPORAÇÃO EM SIMULADOR DE PROCESSOS COMERCIAL

MATHEMATICAL MODELING AND NUMERICAL SIMULATION OF
BUBBLING FLUIDIZED BED REACTORS AND INCORPORATION IN
COMMERCIAL PROCESS SIMULATOR

Campinas

2020

MAURO JUNIOR AIRES DE OLIVEIRA

MATHEMATICAL MODELING AND NUMERICAL SIMULATION OF
BUBBLING FLUIDIZED BED REACTORS AND COUPLING IN
COMMERCIAL PROCESS SIMULATOR

MODELAGEM MATEMÁTICA E SIMULAÇÃO NUMÉRICA DE
REATORES DE LEITO FLUIDIZADO BORBULHANTE E
INCORPORAÇÃO EM SIMULADOR DE PROCESSOS COMERCIAL

Tese apresentada à Faculdade de Engenharia Química da Universidade Estadual de Campinas como parte dos requisitos exigidos para a obtenção do título de Doutor na área de Engenharia Química.

Thesis presented to the School of Chemical Engineering of the University of Campinas in partial fulfillment of the requirements for the degree of Doctor, in the area of Chemical Engineering.

Supervisor:

Prof^a Dr^a Maria Teresa Moreira Rodrigues

ESTE TRABALHO CORRESPONDE À
VERSÃO FINAL DA TESE DEFENDIDA
PELO ALUNO MAURO JUNIOR AIRES
DE OLIVEIRA, E ORIENTADA PELA
PROFA. DRA. MARIA TERESA
MOREIRA RODRIGUES.

Campinas

2020

Ficha catalográfica
Universidade Estadual de Campinas
Biblioteca da Área de Engenharia e Arquitetura
Luciana Pietrosanto Milla - CRB 8/8129

OL4m Oliveira, Mauro Junior Aires de, 1988-
Mathematical modeling and numerical simulation of bubbling fluidized reactors and incorporation in commercial process simulator / Mauro Junior Aires de Oliveira. – Campinas, SP : [s.n.], 2020.

Orientador: Maria Teresa Moreira Rodrigues.
Tese (doutorado) – Universidade Estadual de Campinas, Faculdade de Engenharia Química.

1. Modelagem matemática. 2. Simulação. 3. Simulação de processos. 4. Fluidização. 5. Reatores químicos - Modelos matemáticos. I. Rodrigues, Maria Teresa Moreira, 1955-. II. Universidade Estadual de Campinas. Faculdade de Engenharia Química. III. Título.

Informações para Biblioteca Digital

Título em outro idioma: Modelagem matemática e simulação numérica de reatores de leito fluidizado borbulhante e incorporação em simulador de processos comercial

Palavras-chave em inglês:

Mathematical modeling

Simulation

Process simulation

Fluidization

Chemical reactors - Mathematical models

Área de concentração: Engenharia Química

Titulação: Doutor em Engenharia Química

Banca examinadora:

Maria Teresa Moreira Rodrigues [Orientador]

Andréa Selene Embirassú Xavier Stragevitch

Adilson José de Assis

Roger Josef Zemp

Raphael Soeiro Suppino

Data de defesa: 12-02-2020

Programa de Pós-Graduação: Engenharia Química

Identificação e informações acadêmicas do(a) aluno(a)

- ORCID do autor: <https://orcid.org/0000-0003-1950-7314>

- Currículo Lattes do autor: <http://lattes.cnpq.br/2313616370524296>

Folha de Aprovação da Defesa de Tese de Doutorado defendida por Mauro Junior Aires de Oliveira aprovada em 12 de fevereiro de 2020 pela banca examinadora constituída pelos seguintes doutores:

Profa. Dra. Maria Teresa Moreira Rodrigues - Presidente e Orientadora

FEQ / UNICAMP

Prof. Dr. Roger Josef Zemp

FEQ / UNICAMP

Prof. Dr. Raphael Soeiro Suppino

FEQ / UNICAMP

Dr. Adilson José de Assis

UFU /MG

Dra. Andréa Selene Embirassu Xavier Stragevitch

UFPE – Centro de Tecnologia/DEQ

ATA da Defesa com as respectivas assinaturas dos membros encontra-se no SIGA/Sistema de Fluxo de Dissertação/Tese e na Secretaria do Programa da Unidade.

ACKNOWLEDGMENTS

I wish to express my gratitude to the State University of Campinas (UNICAMP) for the facilities and equipments used in the work, and for the software license of the Aspen Plus Process Simulator. My respectful gratitude to the National Council for Scientific and Technological Development (CNPq) for its funding in this research under the process number 140463/2015-1. Special thanks to Professor Dr. José Roberto Nunhez, for my acception in the post-graduation program, to Professor Dr^a. Maria Teresa Moreira Rodrigues for her dedication as my supervisor, to Maria Teresa Casamassa and Aline Gomes Pinelli, Staff members of the Post-Graduation Secretary of the Unicamp school of Chemical Engineering, and to Fernando Belluomini, secretary of the Department of Chemical Systems Engineering, for their help on academic features.

Grateful thanks to my friends Diogo Jorqueira and Alex Vazzoler for their tips and helps on my research and writings.

RESUMO

Simuladores de processos têm a capacidade de realizar cálculos complexos de balanços de massa e energia simultâneos, porém, possuem limitações significativas a respeito dos modelos de reatores químicos que eles possuem. Geralmente tais módulos já codificados nos simuladores são modelos ideais (CSTR e PFR) ou apenas blocos de cálculo que utilizam estequiometria simples ou cálculos de equilíbrio termodinâmico, e esses modelos não representam o comportamento real dos reatores industriais. Por outro lado, modelos mais detalhados de reatores possuem complexidade matemática alta e geralmente são simulados a parte da simulação do resto da planta. Nessa tese é realizado o desenvolvimento de um modelo matemático para um reator químico complexo (reator de leito fluidizado borbulhante) com estratégia sequencial modular para solução numérica, a implementação do modelo desenvolvido em uma linguagem e software amplamente utilizados e difundidos (Excel / VBA) e é realizado o acoplamento desse código em um simulador de processos comercial (Aspen PlusTM) para que o modelo de reator seja simulado dentro da planta como um módulo programado pelo usuário. Devido às características do software e linguagem usados para codificar o modelo, ele também pode ser simulado como um módulo stand-alone, descrevendo o comportamento do reator desacoplado do simulador. Tanto o uso stand-alone quanto o uso acoplado ao simulador exige que dados termodinâmicos das espécies químicas e parâmetros cinéticos das reações químicas em questão sejam inseridos no módulo. Essa metodologia foi aplicada a um importante processo químico como estudo de caso, e os resultados obtidos apresentaram-se fisicamente compatíveis, de acordo com o comportamento esperado para reatores de leito fluidizado borbulhante.

PALAVRAS-CHAVE: Modelagem matemática. Simulação. Simulação de processos. Fluidização. Reatores químicos – modelos matemáticos.

ABSTRACT

Process simulators have the capability to solve simultaneously complex calculations for mass and energy balances. However, they have important limitations about the models for chemical reactors. Usually, such embedded modules are ideal models (CSTR and PFR) or just calculations blocks which uses simple stoichiometric relations or thermodynamic equilibrium calculations, and these models do not represent the industrial reactors real behavior. On other hand, more detailed models have high mathematical complexity and are usually simulated offline the flowsheet simulation. In this thesis is performed the development of a mathematical model for a complex chemical reactor (bubbling fluidized bed reactor) with sequential-modular strategy for numerical solution, the coding of the model using software and language widely used and available (Excel / VBA) and it is performed the coupling of the code into a commercial process simulator (Aspen PlusTM), so the model can be run into the flowsheet as a user programmed module. Due to the characteristics of the software and language used to code the model, it can also be simulated as a stand-alone module, describing the reactor behavior uncoupled with the process simulator. Both the stand-alone usage and the simulator coupled usage require thermodynamic data for the chemical species and kinetic parameters for the occurring chemical reactions to be inserted into the module. This methodology was applied to an important chemical process as case study, and results provided good physical match, according to the behavior expected to bubbling fluidized bed reactors.

KEYWORDS: Mathematical modeling. Simulation. Process simulation. Fluidization. Chemical reactors – mathematical models.

LIST OF FIGURES

	Page
Figure 2.1: Gazprom Neftekhim Ethylbenzene and Styrene plant.	16
Figure 2.2: Simplified flowsheet of a Styrene plant.	16
Figure 2.3: Flowsheet with recycle stream and one partition.	17
Figure 2.4: Usual structure of a modular process simulator.	18
Figure 2.5: Stand-alone and inside flowsheet reactor module.	19
Figure 2.6: Aspen Plus TM Reactors Modules.	19
Figure 2.7: Information required to model a chemical reactor.	21
Figure 2.8: Non-ideal flow in real reactors.	22
Figure 2.9: Usual paths for reactor simulation.	22
Figure 2.10: Proposition of this thesis.	23
Figure 2.11: Industrial CSTR for production of Polyethylene.	24
Figure 2.12: Tubular reactor (steam inlet at point 1 and outlet at point 2).	24
Figure 3.1: Fluidized Bed.	26
Figure 3.2: Erosion of pipe from a fluidized bed combustor inbed.	27
Figure 3.3: Geldart classification chart.	28
Figure 3.4: Pressure drop versus superficial velocity diagram.	29
Figure 3.5: Bubbling Fluidized Bed, with emulsion phase e bubble phase (bubble, cloud and wake).	29
Figure 3.6: Turbulent Fluidized Bed.	30
Figure 3.7-a: Fast Fluidized Bed with low and high feed rate of solids.	31
Figure 3.7-b: Pneumatic Conveying Bed.	31
Figure 3.8: General two-phase model.	32
Figure 3.9: Two-phase theory and real bubbling bed physical behavior.	34
Figure 3.10: Thesis objective for bubbling fluidized bed modeling.	34
Figure 3.11: User module structure.	35
Figure 3.12: Circulating Fluidized Bed Reactor Simulation in Aspen Plus TM in SOTUDEH-GHAREBAAGH et al. (1998).	36
Figure 3.13: Simulation of biomass gasification in fluidized bed reactor on Aspen Plus TM from NIKOO and MAHINPEY (2008).	37
Figure 3.14: Scheme for dual fluidized bed reactor simulation by ABDELOUAHED et al (2012).	37
Figure 3.15: Aspen simulation of dual fluidized bed reactor from ABDELOUAHED et al (2012).	38

Figure 3.16:	Simulation of biomass gasification from BEHESHTI, GHASSEMI and SHAHSAVAN-MARKADEH (2015).	38
Figure 3.17:	Simulation of biomass gasification in fluidized bed reactor from KAUSHAL and TYAGI (2017).	39
Figure 4.1:	Zones of a BFB.	40
Figure 4.2:	Perforated plate.	41
Figure 4.3:	Arrangement of directional nozzle tuyeres.	41
Figure 4.4:	Example of pipe grids.	42
Figure 4.5:	Gas recirculation between cloud and bubble.	43
Figure 4.6:	Bubble shape and comparison between models to predict cloud thickness.	44
Figure 4.7:	Bubbles assumed as spherical caps.	44
Figure 4.8:	Coalescence of bubbles.	47
Figure 4.9:	Splitting of bubbles.	47
Figure 4.10:	Proposed flowchart of the bubble-cloud-wake system.	49
Figure 4.11:	Material balance for the bubble as a stirred tank.	49
Figure 4.12:	Material balance for the catalytic CSTR.	51
Figure 4.13:	Comparison of the result of CSTRs in series and one PFR.	52
Figure 4.14:	Material balance for a series of catalytic CSTRs.	52
Figure 4.15:	Length of the path of gas and particles in the cloud.	53
Figure 4.16:	Solids fraction in dense zone of fluidized beds versus gas velocity.	57
Figure 4.17:	Proposed scheme of reactors combination in emulsion phase.	58
Figure 4.18:	Distinction between the bubbling bed and the freeboard.	59
Figure 4.19:	Decay rate versus particle diameter.	61
Figure 4.20:	Plot of aU_0 versus d_p .	62
Figure 4.21:	Measurements of a cyclone.	63
Figure 4.22:	High and medium efficiency Stairmand-Kelsey cyclones.	63
Figure 4.23:	Inlet structures of the cyclone.	64
Figure 4.24:	Model structure.	66
Figure 4.25:	Required input and output	67
Figure 5.1:	Process simulators options for user models languages.	78
Figure 5.2:	Chemical species selection.	80
Figure 5.3:	Thermodynamics package selection.	80
Figure 5.4:	Flowsheet with user module inserted.	80

Figure 5.5:	Excel template path specification.	81
Figure 5.6:	VBA code programming.	82
Figure 5.7:	Aspen Plus™ procedure to execute user model Excel spreadsheet.	82
Figure 6.1:	Molecular structure of the phthalic anhydride.	83
Figure 6.2:	Process Flow Diagram for the Sherwin-Williams / Badger Process.	83
Figure 6.3:	Simplified reactions network of the naphthalene oxidation.	84
Figure 6.4:	Reactions of coke formation and consumption.	85
Figure 6.5:	More detailed reactions network of the naphthalene oxidation.	85
Figure 6.6:	Reactions network as described by D'ALESSANDRO and FARKAS (1956) ³⁶ .	86
Figure 6.7:	Reactions network used on the estimation by PETERSON (1962) ³⁷ .	86
Figure 7.1:	Naphthalene conversion versus reactor height.	97
Figure 7.2:	Molar flow rate of phthalic anhydride at the reactor exit versus bed temperature and gas superficial velocity.	99
Figure 7.3:	Molar flow rate of maleic anhydride at the reactor exit versus bed temperature and gas superficial velocity.	100
Figure 7.4:	Selectivity of phthalic anhydride over maleic anhydride.	101
Figure 7.5:	Molar flow rate of naphthoquinone at the reactor exit versus bed temperature and gas superficial velocity.	102
Figure 7.6:	Selectivity of phthalic anhydride over naphthoquinone.	103
Figure 7.7:	Conversion of naphthalene.	104
Figure 7.8:	Carbon monoxide at the reactor exit versus bed temperature and gas superficial velocity.	105
Figure 7.9:	Carbon dioxide at the reactor exit versus bed temperature and gas superficial velocity.	106
Figure 7.10:	Temperature distribution along reactor height.	107
Figure 7.11:	Pressure distribution along reactor height.	107
Figure 7.12:	Cascade control of bed temperature.	108

LIST OF TABLES

	Page
Table 2.1: Example of chemical processes with fluidized bed reactors.	25
Table 4.1: Orifice coefficient versus Reynolds number.	42
Table 4.2: Cyclone measurements values for high and medium efficiency equipment.	63
Table 4.3: Deflector position and K value.	64
Table 6.1: Kinetics data obtained by PETERSON (1962) ³⁷ .	87
Table 6.2: Pseudo-first order constants for 320°C and 370°C and activation energy for reactions for both catalysts.	87
Table 6.3: Kinetic data obtained by non-linear regression of data from CARBERRY and WHITE (1969) ³⁹ .	88
Table 6.4: Kinetics data described by DUTTA and SUCIU (1989) ⁴³ .	88
Table 6.5: Coefficients for heat capacity equation.	89
Table 6.6: Standard heat of formation of the substances.	90
Table 6.7: Standard heats of reactions.	91
Table 6.8: Geometry parameters of the reactor.	92
Table 6.9: Operating conditions of the reactor.	92
Table 6.10: Particle parameters of the reactor.	92
Table 6.11: Air parameters of the reactor.	92
Table 7.1: Reactor experimental data.	94
Table 7.2: Optimized parameters for modified Arrhenius model.	95
Table 7.3: Comparison between model and experimental output.	95
Table 7.4: Values of bed temperature, gas superficial velocity and mass flow rate.	98

CONTENTS

	Page
1 INTRODUCTION	14
1.1 Motivation	14
1.2 Objectives	14
1.3 Contributions to Chemical Reactor Modeling	15
1.4 Thesis Structure	15
2 PROCESS SIMULATORS	16
3 FLUIDIZED BED REACTORS	26
4 MATHEMATICAL MODELING	40
4.1 Distributor	40
4.2 Bubbling Bed	43
4.2.1 Bubbles	43
4.2.2 Emulsion	55
4.3 Splash Zone	58
4.4 Freeboard	58
4.5 Cyclones	62
4.6 Model Structure	65
4.6.1 Required Input	66
4.6.2 Distributor Model	67
4.6.3 Preliminary Fluid Dynamics Calculations Block	68
4.6.4 Bubble-Cloud-Wake Model	71
4.6.5 Emulsion Model	74
4.6.6 Splash Zone Model	75
4.6.7 Freeboard Model	75
4.6.8 Cyclones Model	76
5 MODEL COUPLING	78
6 CASE STUDY	83
6.1 Phthalic Anhydride	83
6.1.1 Chemical Reactions	84
6.1.2 Chemical Kinetics	86
6.1.2 Case Thermodynamics	89
6.1.4 Reactor Geometry	91

7	RESULTS AND DISCUSSION	93
7.1	Model Calibration	93
7.1.1	Input-Output data fit	93
7.1.2	Internal Distributions	96
7.2	Simulations After Coupling in Aspen Plus™	97
7.2.1	Simulations Planning	97
7.2.2	Final Results	98
7.2.2.1	Phthalic Anhydride	99
7.2.2.2	Maleic Anhydride	100
7.2.2.3	Naphthoquinone	102
7.2.2.4	Naphthalene Conversion	104
7.2.2.5	Carbon Monoxide	105
7.2.2.6	Carbon Dioxide	106
7.2.2.7	Temperature Distribution	107
7.2.2.8	Bed Pressure Drop	107
8	CONCLUSIONS	110
9	SUGGESTIONS FOR FUTURE WORKS	112
	REFERENCES	113
APPENDICE A	Particle-to-gas Mass and Heat Transfer	120
APPENDICE B	Chemical Reactions Approach	125
APPENDICE C	Solids Distribution	127
APPENDICE D	Thermodynamics	129
APPENDICE E	VBA program structure	142

1 - INTRODUCTION

1.1 - Motivation

Process simulators are very useful tools for the design of chemical plants and operation of industrial processes. However, the development of process simulators had focus on the most conventional unit operations and thermodynamics models, and therefore models for chemical reactors do not deal with the real chemical reactors complexity, and this generates a problem: how to simulate a chemical plant with a higher degree of accuracy if models for chemical reactors do not match the real behavior of industrial reactors? This thesis proposes alternate approach for this problem.

The proposition described in the following pages has basically two parts: mathematical modeling of the chosen chemical reactor, and coupling of the developed model in a commercial chemical process simulator. Mathematical modeling was performed with several basic concepts of chemical engineering, such as fluid mechanics analysis, fluidization, mass and heat transfers, chemical reactions catalyzed by solids and advanced mathematics. The coupling of the model was done using computational programming techniques and specific guidelines of the process simulator in use.

The developed model was then applied to an important petrochemical process as a case study, in order to analyze results and conclude whether it has or not physically consistent behavior.

1.2 – Objectives

- Development of a detailed model for bubbling fluidized bed chemical reactor and implementation using programming language and software widely used in industrial environment (Microsoft Excel/VBA).
- Coupling of the developed model coded in VBA/Excel in a commercial process simulator of wide usage in the chemical industry (Aspen PlusTM).

1.3 – Contributions to Chemical Reactor Modeling

Several models for Bubbling Fluidized Bed Reactors have been developed and published along the time. However, they usually are based on a theory which does not match the real physical behavior of the bubbling fluidization, and usually are suitable only for simple and elementary chemical reactions. Also, existing models, when coupled with process simulators, are usually separated into modules from the simulator library and the subroutines are implemented with programming languages for specific modules, i.e., such models may not be run outside the flowsheet from the simulator.

The model developed in this thesis accounts for non-ideal flow pattern of the fluidization phenomenon, allows multiple chemical reactions to be analyzed and deals with heat and mass transfer between gas and particles, while existing models usually do not. Furthermore, it is programmed as a whole user module, which may be run coupled with the process simulator or stand-alone, as an independent spreadsheet. All these features may characterize the work as original contribution.

1.4 – Thesis Structure

This thesis is structured in the following way: chapter two deals with process simulators, what they are, how they work and their limitations, and also deals with the motivation for the type of chemical reactor chosen for modeling. Chapter three deals with the description of the chosen type of reactor (the fluidized bed reactor). Chapter four describes the full mathematical modeling. Chapter five shows how the developed model was coupled in the Aspen PlusTM process simulator and the motivation for this choice of simulator and programming language (Visual Basic for Applications – VBA). Chapter six shows the chemical process used as case study (Naphthalene oxidation to produce phthalic anhydride). Results with analysis, conclusions and suggestions for future works are provided in chapters seven, eight and nine respectively.

2 – PROCESS SIMULATORS

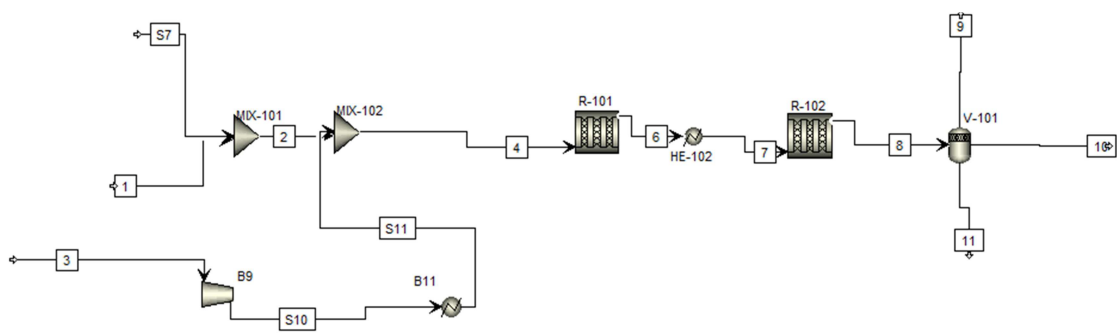
A chemical process is represented by a *flowsheet*, which is a diagram with the streams network and equipment arrangement in a process (figure 2.2). The mathematical solution of the flowsheet material and energy balances is called *process simulation* or *flowsheeting*. The computer code used to solve the material and energy balances of the flowsheet is a *process simulator* or *flowsheeting code*.¹

Figure 2.1 – Gazprom Neftekhim Ethylbenzene and Styrene plant.



Source: Gazprom Neftekhim.

Figure 2.2 – Simplified flowsheet of a Styrene plant.

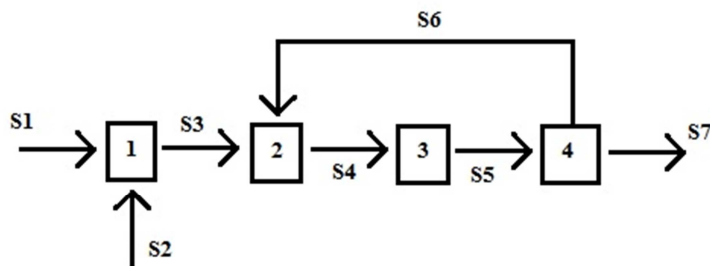


Process simulators usually work with two approaches of solution: *equation-oriented* method or *modular* method. In the equation-oriented method, the entire set of equation is organized and solved simultaneously, while in the modular method the process is represented by a collection of modules which contains the models (material and energy balance equations) for each equipment or subsystem.¹

In equation-oriented approach flowsheet equations are solved simultaneously. However, such mode of simulation requires a large-scale non-linear equation solver for the whole flowsheet and careful initialization for a successful solution, which is often problem specific.²

Modular method of flowsheeting is the most common in commercial process simulators. The modules usually have the formulation of input-output model. In other words, given the input values, the module calculates the output values. The modules represent individual equipments (such pumps, reactors, flash drums, and so on) and can be coded, analyzed, debugged and interpreted by itself.¹

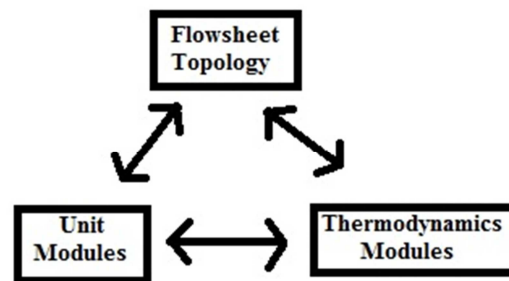
Figure 2.3 – Flowsheet with recycle stream and one partition.



The mode that streams and equipments are connected in the flowsheet is called *flowsheet topology*. From the flowsheet topology it is possible to find groups of modules which must be solved together due to recycle streams. Such groups are called *partitions*, as in figure 2.3, and the procedure to find them is called *partitioning*. As the modules are solved in sequence, one of the streams of the partition, which is called *tear stream*, must be estimated for the solution to begin, and after the modules being calculated and the loop close, the calculated value of the tear stream is compared with the estimated value till convergence.¹

The structure of a modular simulator generally consists of three levels: the flowsheet topology, the unit operations models (unit modules) and the physical properties models (thermodynamics modules). These levels exchange calculated data between them (figure 2.4 shows these relationships). Flowsheet topology provides input streams and equipment parameters for the unit modules, in addition to the sequence of unit modules to be solved. Unit modules call thermodynamics modules to calculate physical properties used in material and energy balances calculations, and finally provide output streams to the flowsheet. Flowsheet also call thermodynamics modules for some stream calculations.²

Figure 2.4 – Usual structure of a modular process simulator.

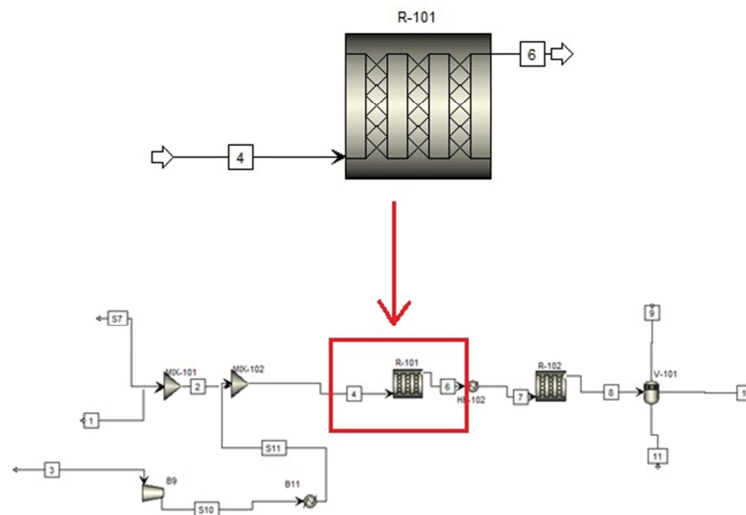


Modular simulation has the advantage to allow addition and removing of modules from the flowsheet without affecting other modules. However, they are not flexible to provide input values from output, as equation-oriented simulation do. This input-output structure also makes the simulation inflexible to calculate design specifications, and additional calculation loops are often required to satisfy such specifications.^{1,2}

Convergence of tear streams is achieved by numerical methods, usually fixed-point methods. Although such methods do not have strong convergence properties like Newton-type methods have, they are suitable when the calculations of derivatives are difficult, like in modular simulation. However, for problems with complex recycle loops, the Broyden method is often a better alternative.²

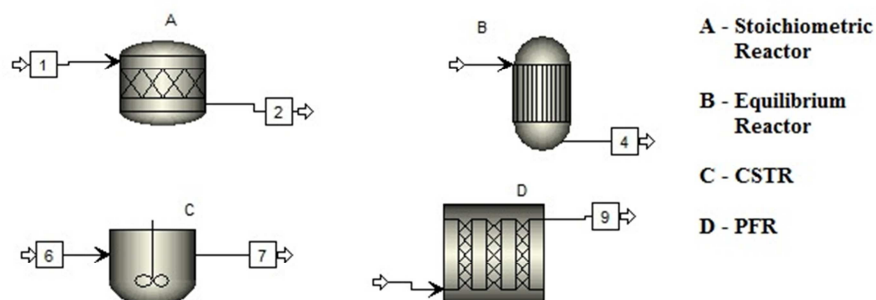
The modules may be run as a part of the flowsheet or in stand-alone mode (figure 2.5). This capability is useful for the design of individual equipments, such as distillation towers and heat exchangers. Some commercial process simulators have additional packages for design of heat exchangers and for energy integration.

Figure 2.5 – Stand-alone and inside flowsheet reactor module.



Modules for separation processes, fluid flow (pumps, compressors and expanders) and heat exchangers are based on thermodynamics, fluid mechanics or heat transfer calculations, and process simulators deal finely with these features. However, this is not suitable for chemical reactors. Models for chemical reactors in process simulators are often very much simplified, and are generally of three types: stoichiometric reactors, equilibrium reactors and specific kinetic reactors (usually CSTR and PFR ideal models), as in figure 2.6.

Figure 2.6 – Aspen Plus™ Reactors Modules.



Chemical reactors usually deal simultaneously with several phenomena, which may result in models with mathematical complexity that turn them computationally expensive and their solution may compromise the flowsheet convergence, since the modular simulation converges tear streams iteratively. Therefore, more detailed reactor models are often used as stand-alone modules out of process simulators for off-line studies and design procedures rather than integrated into the flowsheet.

The use of detailed reactor models as stand-alone computer programs has a great drawback: the modular simulator structure allow the calling of thermodynamics modules by the unit operations modules, and for this calling to occur in the stand-alone reactor module, the program usually must have a large amount of thermodynamics data to be collected and stored, while in process simulators such task already has been done. Although modules inside the flowsheet can use the thermodynamic database inside the process simulator data for physical properties calculations, it is usually true only for modules created by the process simulator developers, and much more difficult (and often not possible) for user modules, because the procedure to call the computational subroutine which calculate these properties are usually not shared by the development team. Therefore, even for a module which will be inserted into a process simulator, it is necessary to feed the module with a thermodynamic database.

An alternative for the problem of thermodynamics data collection is the CAPE-OPEN standards. CAPE-OPEN standards allow data transfer between chemical engineering softwares. Although such methodology was not used in this thesis, it is a good option to avoid computational programming of thermodynamics methods.

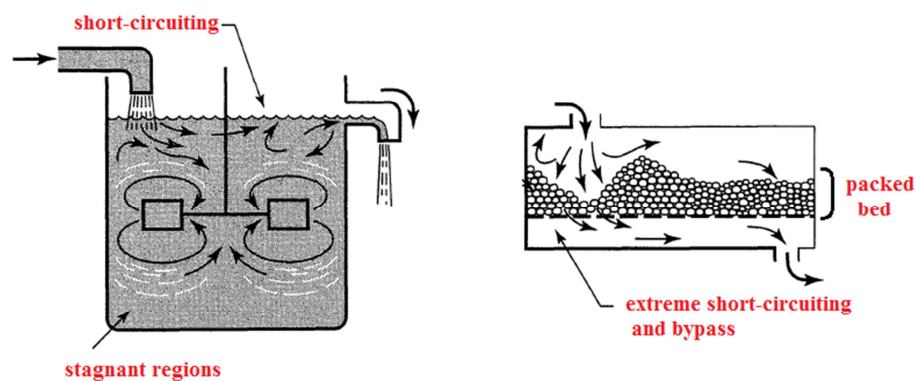
Although thermodynamics database is a major problem for stand-alone reactor models, they can provide important results, like internal distributions (such as concentration, pressure and temperature) for non-ideal flow patterns, which are not performed from the ideal models in the process simulators.

CSTR and PFR models, are models for ideal reactors running homogeneous reactions (one phase only). CSTR model consider fluids under perfect mix, while PFR model considers plug flow of fluid (no radial variation of velocity and concentrations). They try to represent, respectively, the Stirred Tank Reactor and the

Tubular Reactor. For reactions catalyzed by solids, the ideal reactor model is the ideal Packed Bed Reactor (ideal PBR), which is a mathematical model similar to the PFR model.

Although, PFR and CSTR models are used to represent chemical reactors in process simulators, such models do not represent the real behavior of industrial reactors. Industrial reactors usually have stagnant regions, channeling of fluid, or both and this reduce the volume of reactor available for chemical reactions to occur and therefore provide a performance worse than the estimated by ideal models (figure 2.7). Furthermore, industrial reactors, under industrial operating conditions, usually are highly influenced by mass transfer, and this phenomenon is not accounted in ideal models.

Figure 2.7 – Non-ideal flow in real reactors.



Source: Adapted from LEVENSPIEL (1999).³

The prediction of a non-ideal chemical reactor outlet is not a simple task, and it relies very much on the contacting patterns and on the chemical kinetics. Contacting patterns depend on the set of chemical reactions the reactor is running, and may be described by fluid mechanics (for homogeneous reactions), multiphase flow (for heterogeneous fluid-fluid reactions), fluidization and flow through packed beds (for heterogeneous solid-fluid reactions and reactions catalyzed by solids), as in figure 2.8.

In other words, the rigorous description of industrial chemical reactors behavior is done only by detailed models. However, as seen before, inclusion of more detailed models in process simulators is problematic due to the mathematical complexity of such models (usually systems of differential equations, ordinary or

partial) which has a trend to crash the simulation. The usual solution for this situation is a two options choice: choice of simple model and flowsheeting, or the choice of detailed model and stand-alone simulation out of process simulators (figure 2.9).

Figure 2.8 – Information required to model a chemical reactor.

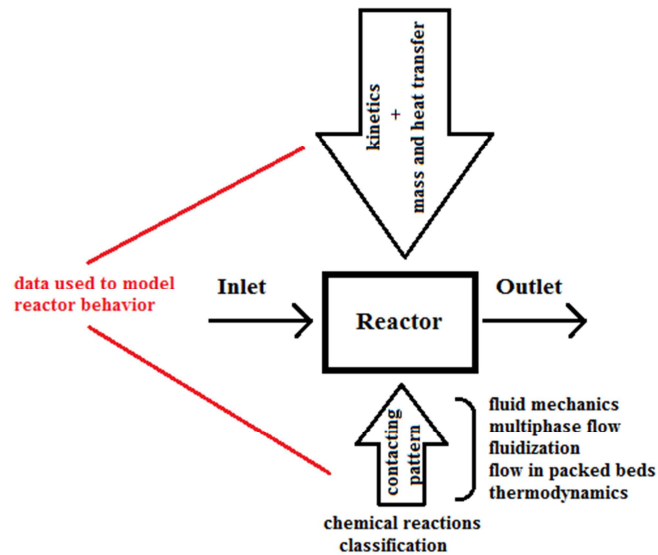
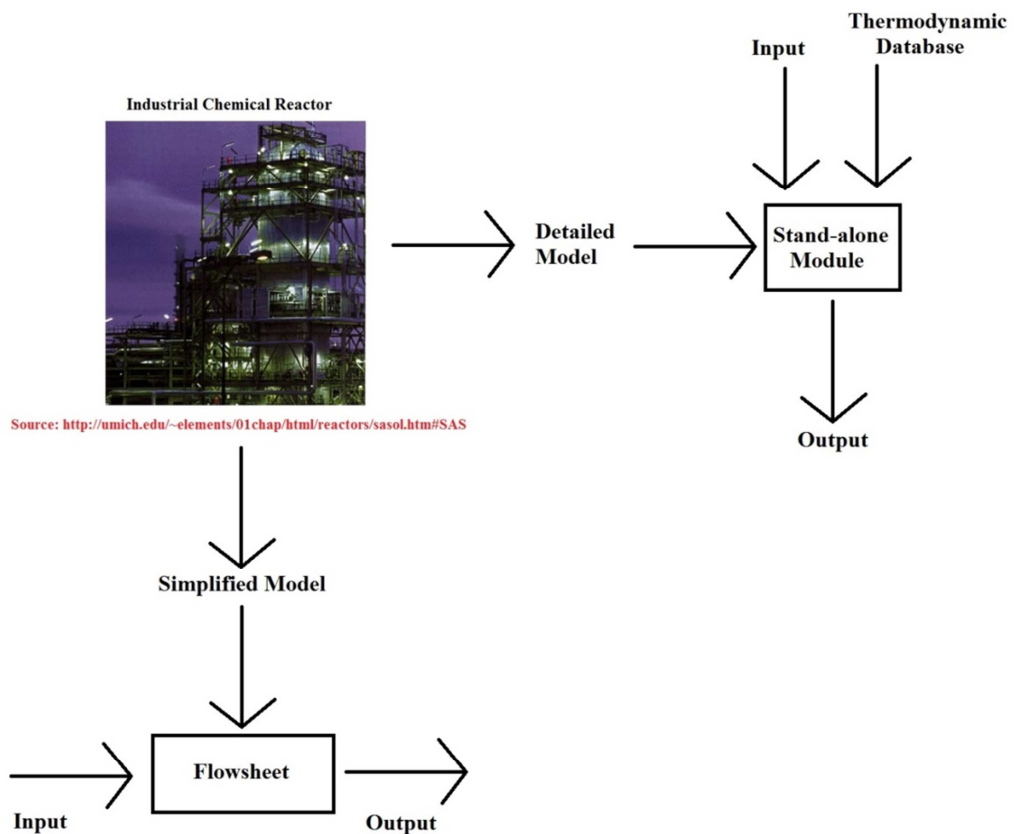


Figure 2.9 – Usual paths for reactor simulation.



According to the type of chemical reactor is being modeled, involved mathematics is more or less complex, and the level of simplification of the simultaneous transport phenomena also has effect on the difficulty of the solution.

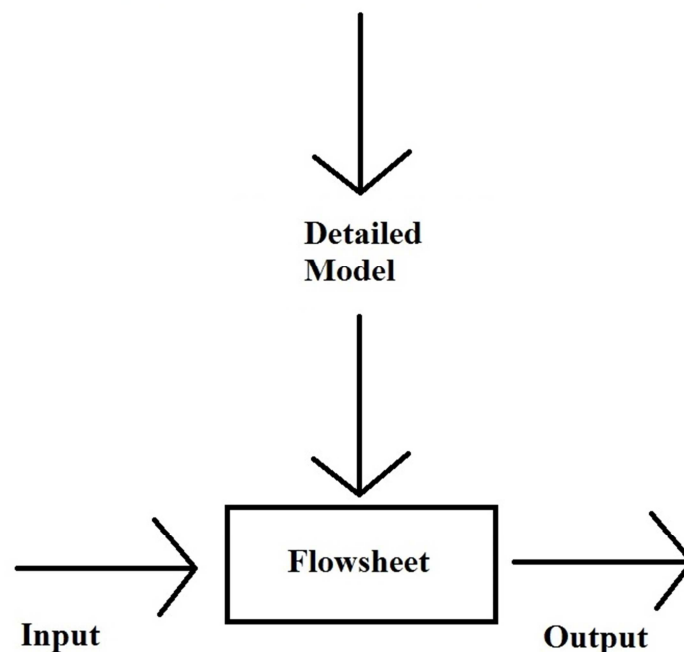
The main objective of this thesis is the development of a detailed model for a complex kind of chemical reactor with mathematical simplicity enough to allow simulation into the flowsheet and still provide good and reliable results (figure 2.10). This proposition allow the simulation of complex reactors with the advantage of good results for the entire chemical plant mass and energy balances and avoid the need for external thermodynamics database.

Figure 2.10 – Proposition of this thesis.

Industrial Chemical Reactor



Source: <http://umich.edu/~elements/01chap/html/reactors/sasol.htm#SAS>



Industrial reactors may be designed for homogeneous reactions, for heterogeneous reactions or for reactions catalyzed by solids. For homogeneous reactions in liquid phase, the most common reactor is the stirred tank (figure 2.11), and for homogeneous reactions in gas phase, the tubular reactor is usually used (figure 2.12). For fluid-fluid heterogeneous reactions, bubbling tanks and spray towers are common options. For fluid-solid heterogeneous reactions, the types of reactors are the same for reactions catalyzed by solids: packed bed, moving bed and fluidized bed reactors.

Figure 2.11 – Industrial CSTR for production of Polyethylene.



Source: essentialchemicalindustry.org

Figure 2.12 – Tubular reactor (steam inlet at point 1 and outlet at point 2).



Source: essentialchemicalindustry.org

Among these varieties of reactors, the type chosen to model was the fluidized bed reactor, because it requires more complex calculations due to the nature of the fluidization and the incorporation of such model in a commercial process simulator is interesting since fluidized bed reactors are very much used in chemical industries.

Table 2.1 – Example of chemical processes with fluidized bed reactors.

Year	Product of Reaction	Company
1945	Phthalic Anhydride	Sherwin-Williams-Badger
1955	Fischer-Tropsch Synthesis	Kellogg, SASOL
1956	Vinyl Acetate	Nihon Gosei
1960	Acrylonitrile	Sohio
1961	Ethylene Dichloride	Monsanto
1965	Chloromethane	Asahi Chemical
1970	Maleic Anhydride	Mitsubishi Chemical
1977	Low Density Polyethylene	Union Carbide
1984	Polypropylene	Mitsui Petrochemical
1984	o-cresol and 2,6-xyleneol	Asahi Chemical

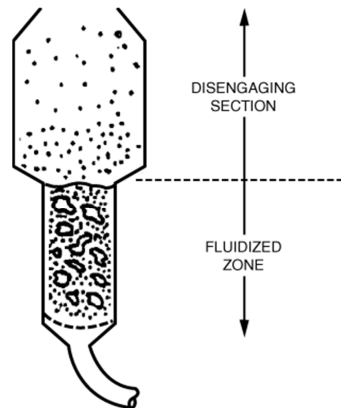
Source: KUNII and LEVENSPIEL (1991) ⁴.

Then, the secondary objective of this thesis is the development of a mathematical model for bubbling fluidized bed reactors which may be run into a commercial process simulator and still provide good and reliable results.

3 – FLUIDIZED BED REACTORS

Fluidized Bed Reactors (FBRs) are chemical reactors which operate with fluid-solid contact under fluidization conditions.

Figure 3.1 - Fluidized Bed.



Source: FOGLER (2006).⁵

The particles move freely through the fluid upward flow, and this motion allow them to be easily removed from the bed. Therefore, fluidized bed reactors are useful for reactions that need frequently removal of solids, such as processes with very fast catalytic deactivation.⁶

Another advantage of the fluidized bed is the fast mixing of solids, which brings the system to an almost isothermal operation, turning easier the control of the unit. The well-mixed solids also respond slowly to sudden changes in the operating conditions, avoiding temperature runaways and providing more safety to the process.

4

Other important advantages are that the pressure drop is independent of flow rate, and good catalytic effectiveness can be achieved by smaller catalyst size usage. However, there are also drawbacks. The entrainment of fine particles and attrition may provide significant losses of catalyst. Moreover, portion of feed gas may escape without contact with catalyst, since the bubbles act as a bypassing mechanism and the most amount of catalytic particles is found in the emulsion and wake regions.⁷

As the fluid mechanics of Fluidized Bed Reactors is complex, there are difficulties to describe the gas flow in fine particles bed, resulting in problems to describe systems that require high gas conversion or high selectivity of an intermediate. Furthermore, erosion of pipes and vessels due to the abrasion of solids may become significant (figure 3.2).⁴

Figure 3.2 – Erosion of pipe from a fluidized bed combustor inbed.



Source: Hydro Alunorte inc.

The gas-solid contact in FBRs is very efficient, with large external surface area. Therefore, when compared to packed bed reactor, reactions limited by intraparticle diffusion will give higher conversion.⁸

One of the earliest and most important applications of FBR is the Fluid Catalytic Cracking, a process widely used in oil refineries around the world and responsible for the production of almost half of the global amount of gasoline. Another important application is the coal gasification, for industries which use coal as the primary source of chemical raw material feedstocks.⁹

As FBRs process chemical reactions under fluidization condition, according to the fluidization regime the hydrodynamic behavior of the reactor will vary. Therefore, it will be explored the features of the fluidization for better understanding.

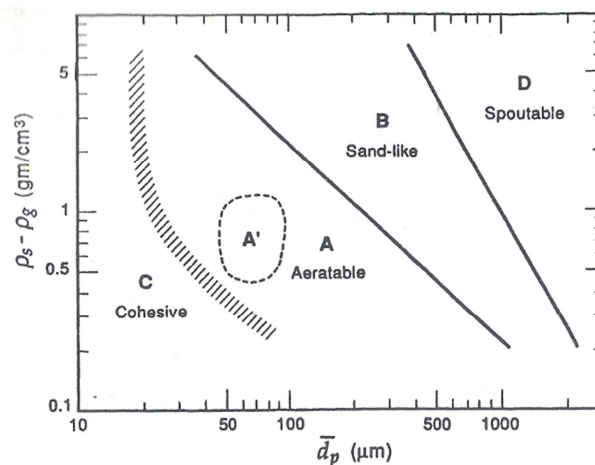
Fluidization is the operation which particulate solids behave in a liquid-like state through contact with a gas or liquid under specific conditions. ¹⁰ There are basically five fluidization regimes: minimum, bubbling, turbulent, fast and pneumatic conveying. They depend on the superficial velocity of gas and on the classification of the particles (Geldart groups).

In 1973, Geldart ¹¹, developed a classification of four kinds of powders:

- *Group A*: after the beginning of the minimum fluidization and before bubbling fluidization starts, the bed expands and the bubbles appear in the minimum bubbling velocity.
- *Group B*: minimum fluidization velocity and minimum bubbling velocity are the same, *i.e.*, the particles begin to fluidize in bubbling regime.
- *Group C*: very fine powders which are cohesive and difficult to fluidize.
- *Group D*: large and dense particles which spout.

Figure 3.3 shows a chart which allows to classify solids according to its mean diameter and densities.

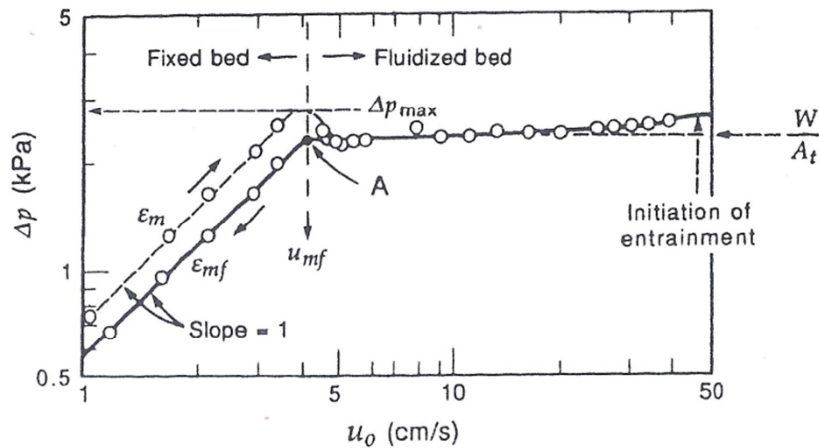
Figure 3.3 – Geldart classification chart.



Source: KUNII and LEVENSPIEL (1991) ⁴.

The minimum fluidization occurs when the superficial velocity (U_0) achieves the value of the *minimum fluidization velocity* (U_{mf}), in which the drag force of upflowing gas equals the total bed weight. In a chart of pressure drop versus superficial velocity (figure 3.4), the minimum fluidization velocity is the velocity in which the pressure drop becomes constant. ⁴

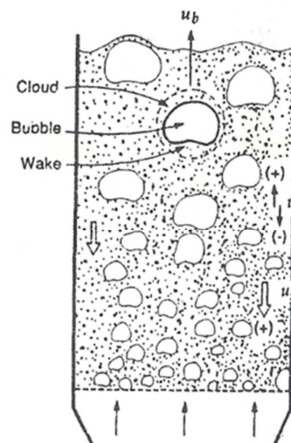
Figure 3.4 – Pressure drop versus superficial velocity diagram.



Source: KUNII and LEVENSPIEL (1991).⁴

As the gas velocity rises, bubbles are formed when the velocity known as *minimum bubbling velocity* (U_{mb}) is reached, and the fluidization regime called *Bubbling Fluidization* starts. In this regime, two distinct phases are observed: a *bubble phase* and an *emulsion phase* (region of gas-solids suspension around the bubbles and elsewhere in the bed), as shown in figure 3.5.⁴

Figure 3.5 – Bubbling Fluidized Bed, with emulsion phase e bubble phase (bubble, cloud and wake).

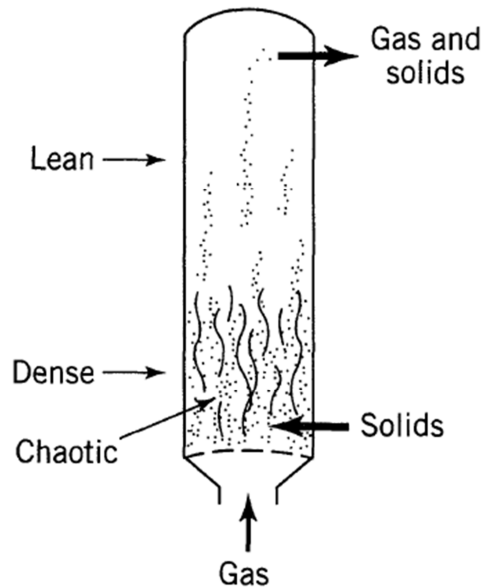


Source: KUNII and LEVENSPIEL (1991).⁴

For Geldart A solids, the minimum bubbling velocity is higher than the minimum fluidization velocity, and a physical expansion occurs in the bed between these velocities. For Geldart B solids, the minimum bubbling velocity is approximately equal to the minimum fluidization velocity, and therefore the bed of this kind of powder does not expand.⁴

As the superficial velocity U_0 increases, the bubbling bed becomes different, with no more distinct bubbles and chaotic movement of solids, clusters of particles together with elongated and distorted voids and more solids are continuously ejected in the freeboard region. This is the *Turbulent Fluidization* Regime, represented in figure 3.6.^{3,5}

Figure 3.6 – Turbulent Fluidized Bed.



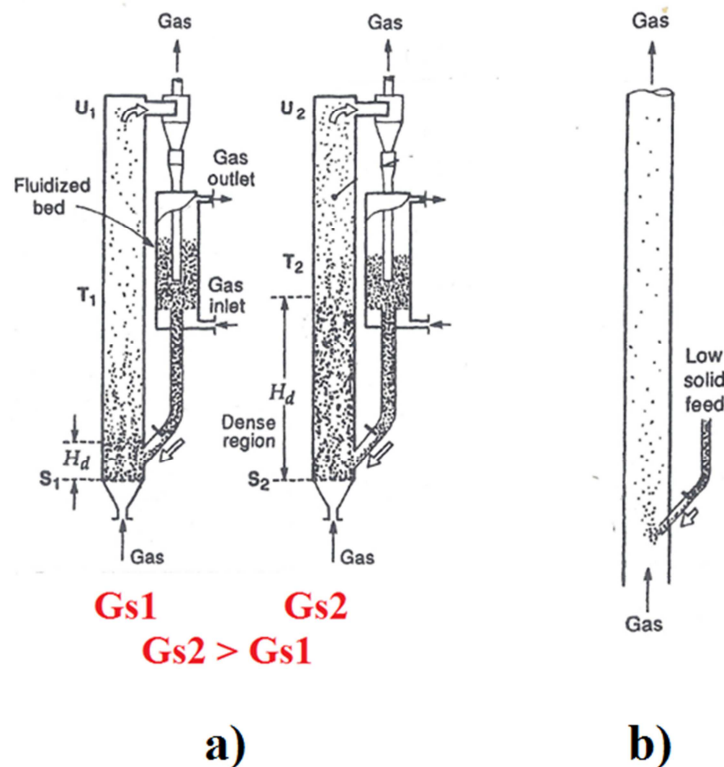
Source: LEVENSPIEL (1999).³

Higher velocities make the transition from turbulent to *Fast Fluidization*. The fast fluidized bed shows a denser region at the bottom, and a leaner region above the denser zone, both for low solids feed rates and for higher feed rates. However, for higher feed rates, the denser region is higher than the same region at lower feed rates, and the leaner region has a higher density of solids than for lower feed rates, as in figure 3.7-a.⁴

Fast fluidization usually occurs when superficial velocities are higher than twenty times the terminal velocity of the solids, i.e., $U_0 > 20 U_t$, with very fine powders. In this regime, the denser zone seems to be composed by a lean core of solids and a wall zone with downflow of solids.^{3,4}

The upflow of gas with velocity high enough and particles feed rate small enough consists of the *Pneumatic Conveying* regime (figure 3.7-b). This regime occurs usually at $U_0 = 20U_t$ and mass flow ratio between solids and gas is usually 1/20. If gas velocity is decreased or the flow rate of solids is increased, a condition that represents the limit of the pneumatic conveying (the *choking condition*) is reached and the pneumatic conveying bed falls to the fast fluidized bed. ⁴

Figure 3.7 – a) Fast Fluidized Bed with low and high feed rate of solids, b) Pneumatic Conveying Bed.



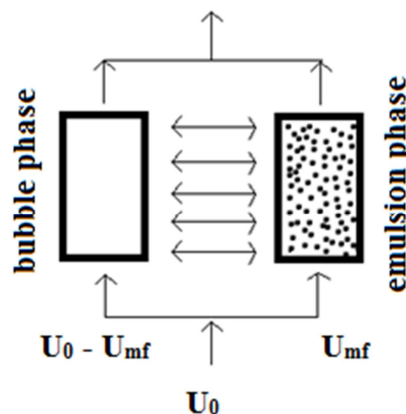
Source: Modified from KUNII and LEVENSPIEL (1991). ⁴

Fluidized beds operating in turbulent, fast and pneumatic conveying regimes need external cyclones to recover the solids entrained out of the bed, in order to avoid the reduction the solids holdup inside the vessel. Therefore, these beds are usually called Circulating Fluidized Beds (CFBs).

Fluidized Bed Reactors (FBRs) have been modeled by two main kinds of models: pseudohomogeneous models and two-phase models.

- **Pseudohomogeneous models:** These models consider the gas and particles as one single phase, using ideal or simple one-parameter models, like plug flow, complete mixing, tanks-in-series models, and among others. As fluidized bed presents a complex fluid dynamics, such models are inaccurate and were dropped by many researchers.¹²
- **Two-phase models:** they are based on the two-phase theory, *i.e.*, they assume that all gas in excess to fluidize the bed is bypassed as bubbles. So, the fluidized bed has two distinct phases: a bubble phase and an emulsion phase (figure 3.8). Both are described by separated governing equations of mass, energy and momentum balances.¹²

Figure 3.8 – General two-phase model.



Many researchers have proposed different versions for two-phase model. However, the model proposed by Kunii and Levenspiel provided the best overall representation of experimental data for the profile of bubble and emulsion phases.¹² It was observed that the bubble gas penetrates only a small length into the emulsion, and flows back to the bubble. Since the penetrated region surrounds the bubbles, it is called *cloud*. It was also observed that as the bubbles flow upward, a low pressure region behind them is formed, called *wake* and this zone drags a substantial amount of solids. Models that consider the cloud and wake are called *Three-phase models*.¹²

The Kunii-Levenspiel model accounts for a thin cloud surrounding the bubbles for fine particles beds, and for a wake of solids dragged up by each rising gas bubble, generating a circulation of solids in the bed (upward behind bubbles and downward elsewhere). Furthermore, it also considers mass transfer between the bubbles and the clouds, and between the clouds and the emulsion.³

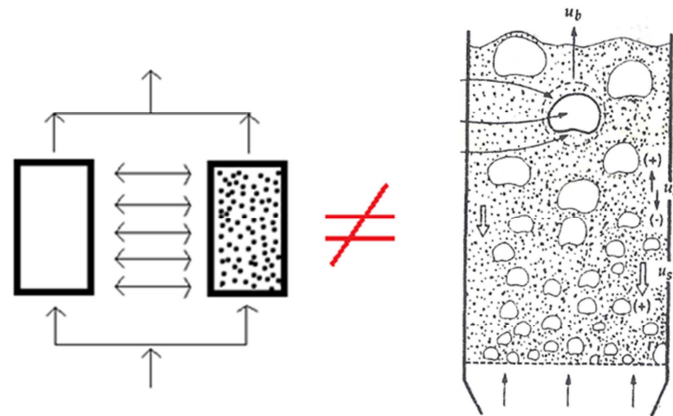
Although the Kunii-Levenspiel model provides good results, it does not account for the effects observed near the distributor (grid region) and in the freeboard (space above the bed surface). It was noticed high reaction rates in the grid region and temperature increase in the freeboard (indicating additional reactions running). Then, this behavior is associate to a more intense heat and mass transfer at such regions.¹²

The fluid dynamics of the grid region and the freeboard are very different from the bubbling bed, so the same models for the bed does not fit for other regions, and a realistic modeling of FBRs must account for three distinct regions in the bed: grid region, bed region and freeboard region. These models are called *Multiple-region Models*.¹²

Two-phase models, three-phase models and multiple-region models have at least one similitude, they consider the bubble (or bubble-cloud-wake system) as a continuous phase. However, the bubbles physically consist in a dispersed phase, and such behavior is in reality different from the one treated mathematically (figure 3.9).

For Circulating Fluidized Beds (CFBs) there are no clear contours for bubbles, so the two-phase theory is a more suitable start point for mathematical modeling of CFBs. However, for Bubbling Fluidized Beds (BFBs), this is not true, and a more realistic modeling may be achieved if the bubbles are modeled with transient physics.

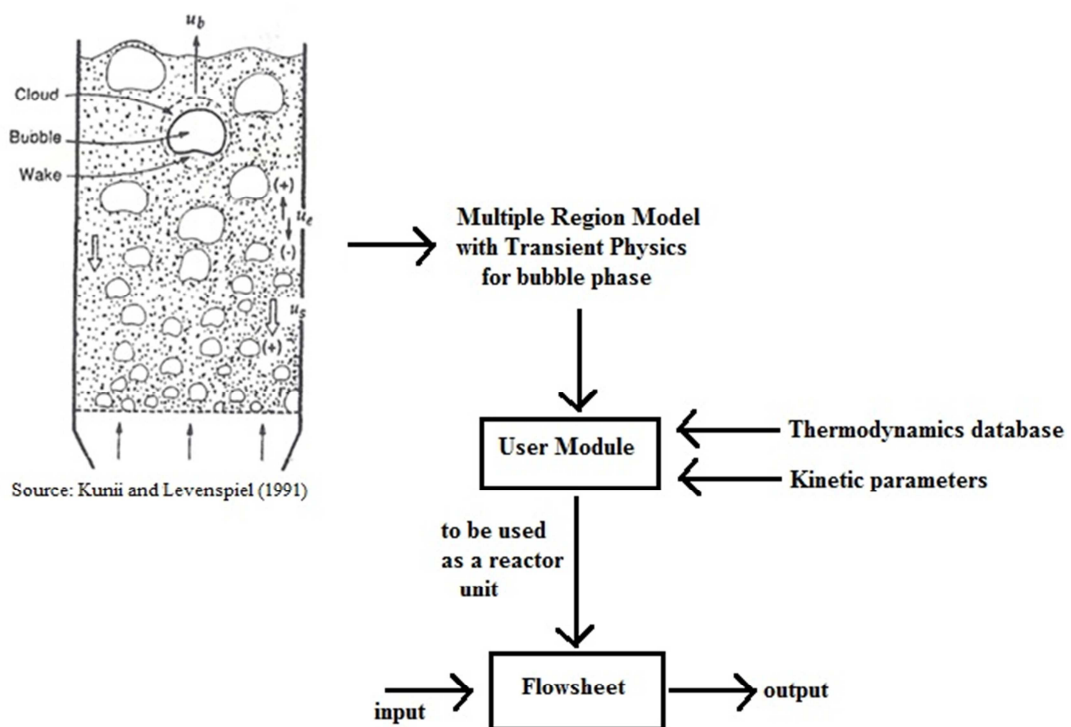
Figure 3.9 – Two-phase theory and real bubbling bed physical behavior.



Source: Adapted from KUNII and LEVENSPIEL (1991).⁴

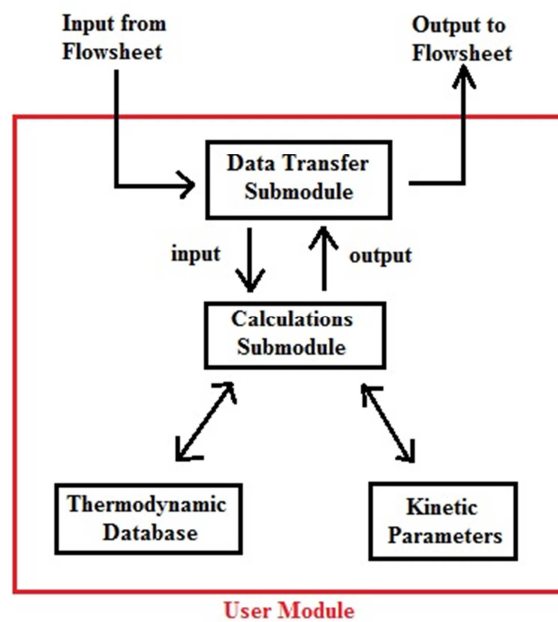
Therefore, this thesis proposes a new mathematical approach for bubbling fluidized bed reactors, which treats the system bubble-cloud-wake as a dispersed phase with transient changes of composition and temperature, and it considers coalescence and splitting of bubbles and chemical reactions controlled by mass transfer. Furthermore, the approach proposed is also mathematically simple enough to satisfy the main objective of this thesis, the coupling of the FBR model in a commercial process simulator (figure 3.10).

Figure 3.10 – Thesis objective for bubbling fluidized bed modeling.



The model developed must be inserted in the process simulator as a user module to be used as chemical reactor unit inside the flowsheet. Thermodynamic database and kinetic parameters have to be included in the user module programming, and therefore the user module structure is similar to the three-level structure of the modular process simulators (figure 3.11).

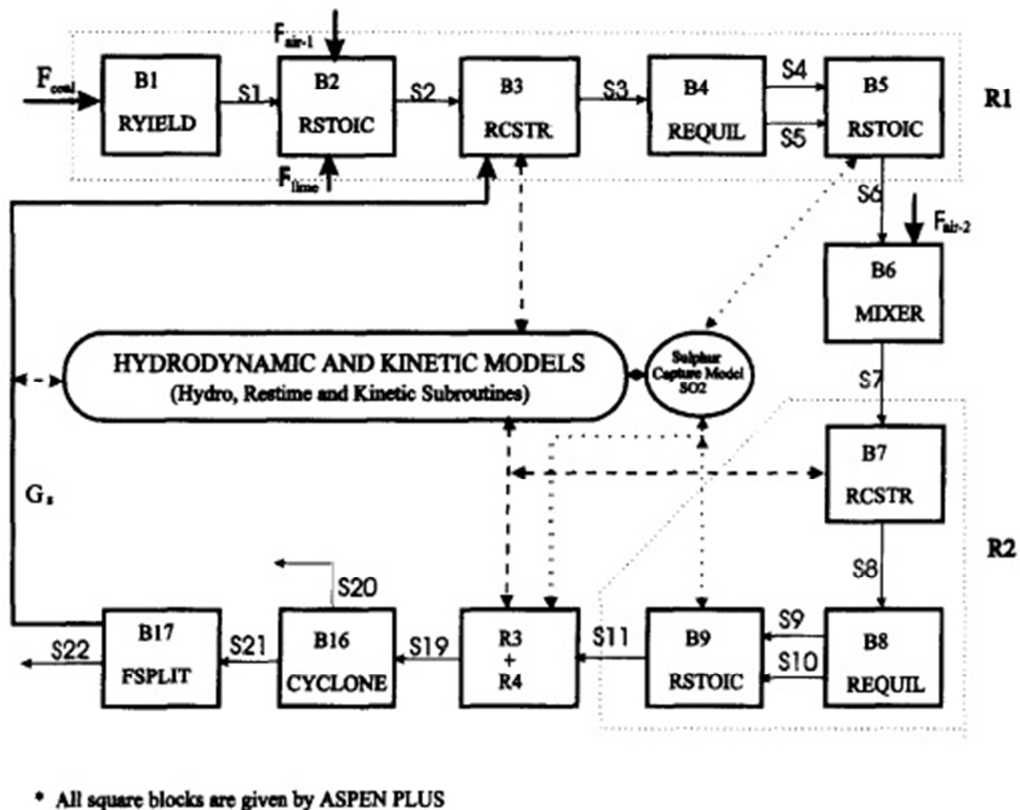
Figure 3.11 – User module structure.



In this mode, thermodynamic database and kinetic parameters may be included in the user module programming without compromise the calculations procedures. Such feature also allows the user module to be used for different chemical systems which use the same reactor type. For example, a Phthalic Anhydride plant and a High Temperature Fischer-Tropsch plant, both plants utilize bubbling fluidized bed reactors, however, the reactive systems are completely different and therefore kinetic parameters and thermodynamics models too. For this example, such data can be changed without effect over the reactor main calculations.

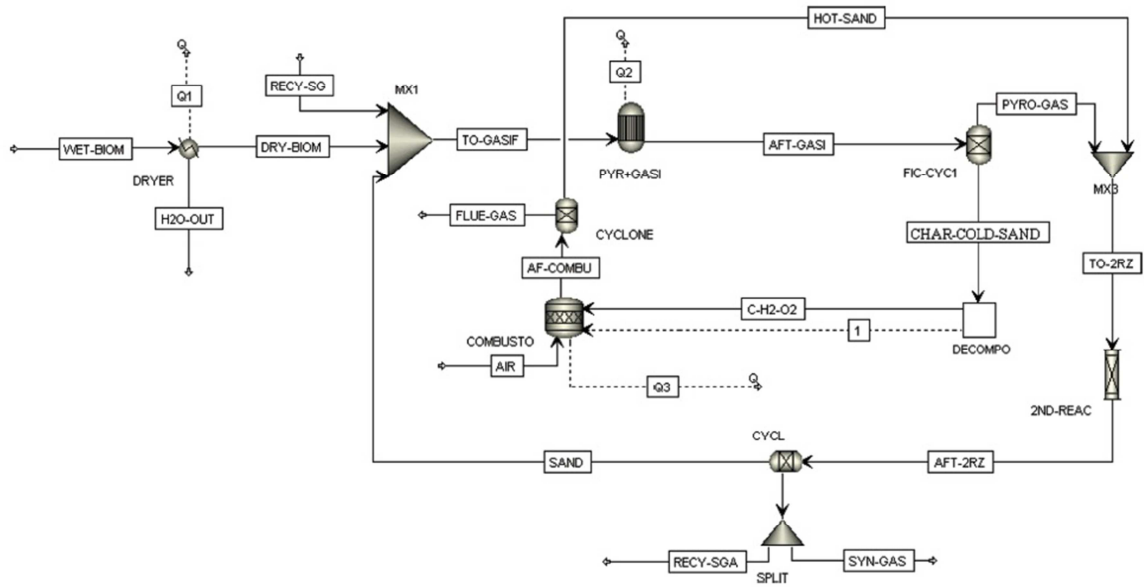
Some researchers published papers dealing with fluidized bed reactors and coupling of such models in Aspen Plus™. However, such works usually use the model of Kunii-Levenspiel, model some regions or phenomena inside the reactor with modules from the simulator and couple user subroutines only at specific modules. SOTUDEH-GHAREBAAGH et al (1998)¹³, figure 3.12, performed in this way for Circulating Fluidized Bed Reactors. NIKOO and MAHINPEY (2008)¹⁴, figure 3.13, also performed this way for biomass gasification in fluidized bed reactor. ABDELOUAHED et al (2012)¹⁵, figures 3.14 and 3.15, performed this way for a dual fluidized bed to operate biomass gasification too. BEHESHTI, GHASSEMI and SHAHSAVAN-MARKADEH (2015)¹⁶, figure 3.16, published a work similar to NIKOO and MAHINPEY (2008). KAUSHAL and TYAGI (2017)¹⁷, figure 3.17, performed similar work.

Figure 3.12 – Circulating Fluidized Bed Reactor Simulation in Aspen Plus™ in SOTUDEH-GHAREBAAGH et al. (1998)¹³.



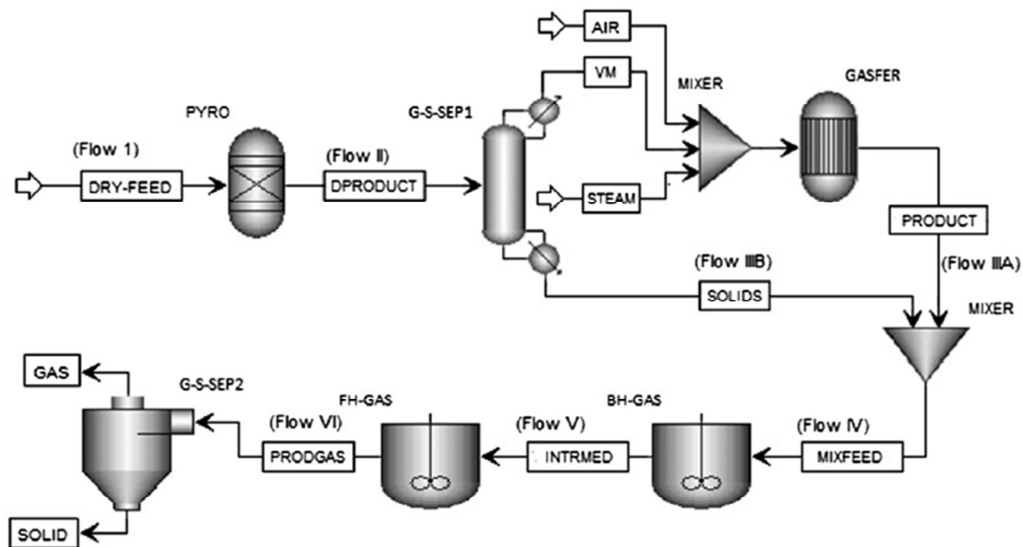
Source: SOTUDEH-GHAREBAAGH et al. (1998)¹³.

Figure 3.15 – Aspen simulation of dual fluidized bed reactor from ABDELOUAHED et al (2012)¹⁵.



Source: ABDELOUAHED et al (2012)¹⁵.

Figure 3.16 – Simulation of biomass gasification from BEHESHTI, GHASSEMI and SHAHSAVAN-MARKADEH (2015)¹⁶.

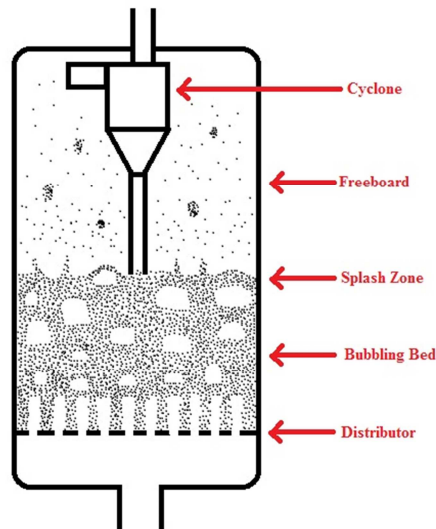


Source: BEHESHTI, GHASSEMI and SHAHSAVAN-MARKADEH (2015)¹⁶.

4 – MATHEMATICAL MODELING

A Bubbling Fluidized Bed (BFB) usually consists of five regions: distributor, bubbling bed, splash zone, freeboard and cyclones. Each region has its own fluid dynamic behavior.

Figure 4.1 – Zones of a BFB.



4.1 - Distributor

The gas distributor is the part of a fluidized bed responsible for the gas injection in the bed of particles. There are four basic types of distributors: porous plates, perforated plates, tuyeres and pipe grids. ⁴

Porous plates are usually used for most small-scale fluidized beds, being made of ceramic or sintered metal. They provide high pressure drop, and therefore give the best gas-solid contact, with uniform distribution of gas across the bed. Although, the high pressure drop increases the pumping power requirements, and this represent a serious drawback for industrial scale. Furthermore, porous plates have low resistance against thermal stresses, low mechanical strength and high cost for some materials. ⁴

Perforated plates (figure 4.2), in other hand, are cheap and easy to fabricate, and therefore are widely used in industry. However, due to the orifices, the plate cross-section is lower and it results in a weaker structure, suitable to deflection under heavy load, and the necessity to reinforcement support. ⁴

Figure 4.2 – Perforated plate.



Source: INDIAMART.COM

Tuyeres are segments of pipes fixed in the bottom of the bed, which gas is blown through them to provide the fluidization. There are two basic types of tuyeres: nozzles and bubble caps. Nozzle tuyeres (figure 4.3) can be simple, consisting of orifices at the top of the tuyere, or directional, to direct the flow of solids to a drain region. Under severe operating conditions (high temperature or highly reactive environment), perforated plates cannot be used, and tuyeres are used in these conditions. Due to the complicated construction, tuyeres are more expensive than perforated plates.⁴

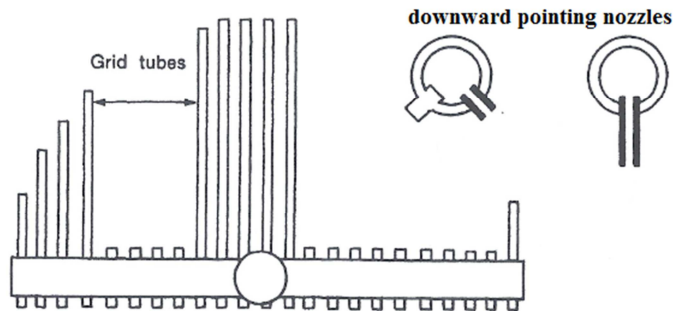
Figure 4.3 – Arrangement of directional nozzle tuyeres.



Source: Basu (2006).¹⁰

Pipe grids, or spargers (figure 4.4), are pipes with orifices or nozzles to insert gas in the fluidized bed. Internals improve gas-solid contact due to the break-up of growing bubbles, so pipe grids may be used to insert reactant gas in a bed fluidized by gas coming from a perforated plate or tuyere distributor below. Furthermore, Downward pointing nozzles avoid clogging when gas flow ceases.⁴

Figure 4.4 – Example of pipe grids.



Source: adapted from Kunii and Levenspiel (1991).⁴

For perforated plates and tuyeres, the pressure drop can be calculated directly by orifice theory:

$$A_{or} = N_{or} \cdot \frac{\pi d_{or}^2}{4} \quad (4.1)$$

$$U_{or} = \frac{U_0}{A_{or}} \quad (4.2)$$

$$\Delta P_d = \frac{\rho_g}{2} \left(\frac{U_{or}}{C_{d,or}} \right)^2 \quad (4.3)$$

In equation (4.1), N_{or} is the number of orifices, d_{or} is the orifice diameter (m) and A_{or} is the area of orifices (m^2). In equation (4.2), U_{or} is the orifice velocity of gas ($m s^{-1}$), and U_0 is the superficial gas velocity ($m s^{-1}$). In equation (4.3), ρ_g is the gas density ($kg m^{-3}$), $C_{d,or}$ is the orifice coefficient and ΔP_d is the distributor pressure drop (Pa).

The orifice coefficient is a non-dimensional parameter dependent on the Reynolds number of the vessel. KUNII and LEVENSPIEL (1991)⁴ provide the table (4.1) with values of $C_{d,or}$ for different Reynolds numbers. For this thesis, these data were fit to an equation by non-linear regression, resulting in equation (4.5).

Table 4.1 – Orifice coefficient versus Reynolds number.

Re	$C_{d,or}$
100	0.68
300	0.7
500	0.68
1000	0.64
2000	0.61
>3000	0.6

Source: KUNII and LEVENSPIEL (1991).⁴

$$Re = \frac{D_t U_0 \rho_g}{\mu} \quad (4.4)$$

$$C_{d,or} = 0.59991 \cdot e^{\left(\frac{50.53866}{Re}\right)}, \text{ for } 100 < Re \leq 3000 \quad (4.5)$$

$$C_{d,or} = 0.6, \text{ for } Re > 3000, \quad R^2 = 0.999198$$

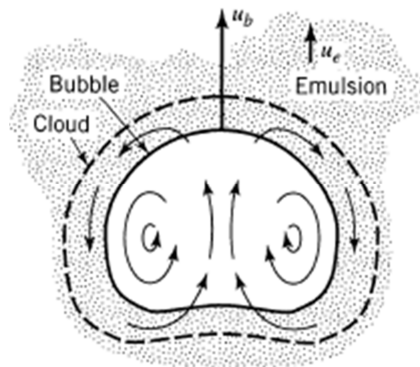
4.2 – Bubbling Bed

The bubbling bed region contains gas and particles in two different contact patterns: bubbles and emulsion. Bubbles have more gas than particles and emulsion more particles than gas.

4.2.1 - Bubbles

Bubbles flow upward along the reactor height and their fluid dynamics have been widely studied since the 1960's. The gas inside the bubbles flow out of them, pass through the clouds and return to the bubble (figure 4.5). Moreover, the faster the bubble rises, more gas stays within the bubbles in vortex motion, and thinner the cloud becomes. ¹⁸

Figure 4.5 – Gas recirculation between cloud and bubble.



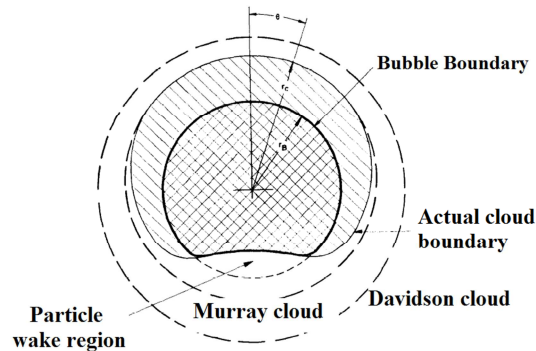
Source: LEVENSPIEL (1999).³

The volume flowrate of gas recirculated between cloud and bubble can be calculated by equation (4.6) ¹⁸:

$$q = \frac{3}{4} U_{mf} \pi d_b^2 \quad (4.6)$$

In equation (4.6), U_{mf} is the minimum fluidization velocity (m s^{-1}), d_b is the bubble diameter (m) and q is the volume flow rate of gas recirculated ($\text{m}^3 \text{s}^{-1}$). Previous investigations and experimental observations show that bubbles do not have a perfectly spherical shape, they are kidney-shaped (figure 4.6).¹⁹

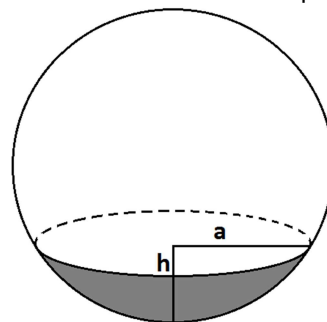
Figure 4.6 – Bubble shape and comparison between models to predict cloud thickness.



Source: adapted from ROWE, PARTRIDGE and LYALL (1964).¹⁹

In order to model the behavior of the physical phenomena, we propose in this work that the bubbles have a spherical cap shape (figure 4.7), similar to the kidney-shape they present in reality. Using geometry proportion, it is proposed that the parameter h from the spherical cap bubble is around 16.33 percent of the bubble diameter.

Figure 4.7 – Bubbles assumed as spherical caps.



Other important hypothesis is the existence of a gap between the cloud and wake, through which the gas flows from the cloud to the wake. Such gap must be thin enough for the bubbles do not lose shape and stability and still allow the gas to flow from one region to other. In this work, it is proposed a gap of *ca.* five percent of the bubble diameter.

The inferior spherical cap (shaded region in figure 4.7) volume is calculated by equation (4.7):

$$V_{spherical\ cap} = \frac{\pi h}{6}(3a^2 + h^2) \quad (4.7)$$

The parameters h and a are related through the following equation:

$$a = [h(d_b - h)]^{0.5} \quad (4.8)$$

As $h = 0.1633 d_b$, implies that:

$$a = 0.3696 \cdot d_b \quad (4.9)$$

The bubble gas circulates between bubble, cloud and wake, so, for the mass transfer calculations it is necessary to estimate the gas velocity in each of these regions. As the volume flow rate of gas is known, the area of the top exit of gas from the bubble, the gap surface and the surface of the bubble bottom must be calculated.

The bubble bottom surface is calculated by equation (4.10), which is simply a circle with radius equal to the parameter a :

$$S_{bottom} = \pi a^2 \quad (4.10)$$

The gap surface is equivalent to a rectangular surface which one side is equal to the bottom circumference and other side is equal to the gap:

$$S_{gap} = 2\pi a \cdot gap \quad (4.11)$$

The outlet of gas from the bubble has a surface of ca. one percent of the bubbles surface:

$$S_{out} = 0.01 \cdot \pi d_b^2 \cdot N_b \quad (4.12)$$

In equation (4.12), N_b represents the number of bubbles at the height and is calculated by the following equation:

$$N_b = \frac{A_{cs} H_{max} \delta}{0.486152 \cdot d_b^3} \quad (4.13)$$

Numerator of equation (4.13) represents the total volume of bed occupied by the bubbles, and denominator represents the volume which one single bubble occupies.

Many researchers provided data which made possible the prediction of the rise velocity of a single bubble as a function of its diameter ⁴:

$$U_{br} = 0.711\sqrt{gd_b} , \frac{d_b}{D} < 0.125 \quad (4.14)$$

$$U_{br} = 1.2 \cdot [0.711\sqrt{gd_b}] e^{(-1.49\frac{d_b}{D})} , 0.125 < \frac{d_b}{D} < 0.6 \quad (4.15)$$

Based on this hypothesis, the bubble velocity can be calculated by the following equation:

$$U_b = K + U_{br} \quad (4.16)$$

For Geldart A solids, it was proposed that ^{4, 20}:

$$K = 1.55 \cdot D^{0.32} [(U_0 - U_{mf}) + 14.1(d_b + 0.005)] \quad (4.17)$$

For Geldart B solids, it was proposed that ^{4, 20}:

$$K = 1.6 \cdot D^{1.35} [(U_0 - U_{mf}) + 1.13d_b^{0.5}] \quad (4.18)$$

For Geldart D solids, it was proposed that ¹⁸:

$$K = U_0 - U_{mf} \quad (4.19)$$

Many researchers have proposed different models for the cloud thickness. However, according to ROWE, PARTRIDGE and LYALL (1964) ¹⁹, the model proposed by MURRAY (1965) ²¹ fits better for the cloud thickness. Such model is described by the followings equations:

$$\frac{d_c}{d_b} = \left(\frac{U_q}{U_q - 1} \right)^{1/3} \quad (4.20)$$

$$U_q = \frac{U_{br}}{U_f} \quad (4.21)$$

$$U_f = \frac{U_{mf}}{\epsilon_{mf}} \quad (4.22)$$

The diameters of the cloud and the bubble are represented respectively by d_c and d_b . In this sense, the cloud width w_c can be calculated by the following equation:

$$w_c = 0.5 \cdot d_b \left[\left(\frac{U_q}{U_q - 1} \right)^{1/3} - 1 \right] \quad (4.23)$$

Bubbles grow by coalescence till a maximum size due to the equilibrium between coalescence and splitting. Coalescence happens when two bubbles are rising, the leader one and the trailing one, the trailing one accelerates when it get close to the wake of the leader one and then drawn into it (figure 4.8).²² Splitting occurs when the roof of the bubble starts to split and this cusp divides the bubble in two, which later or immediately (depending if they are equal or one bigger than the other) get together (figure 4.9).¹⁹ Although many models for bubble growth account for coalescence and splitting were developed, the model proposed by HORIO and NONAKA (1987)²³ is of wide use because it can be used for all range of particles, from Group A to D. Some researchers concluded this is the best model to fit experimental data.²⁴

Figure 4.8 – Coalescence of bubbles.

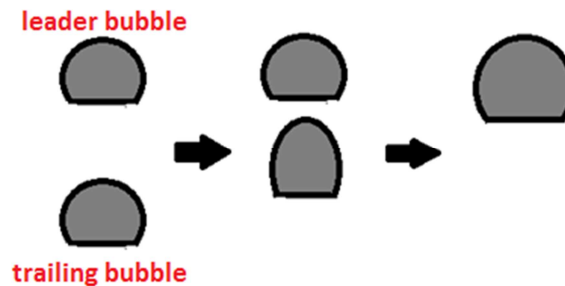


Figure 4.9 – Splitting of bubbles.



The Horio and Nonaka bubble growth model calculates the bubble diameter with the following equations (4.24) to (4.30):

$$d_b^{max} = 2.59 \cdot [A_{ts}(U_0 - U_{mf})]^{0.4} \cdot g^{-0.2} \quad (4.24)$$

$$d_b^{min} = 1.38 \cdot \left[A_{ts} \frac{(U_0 - U_{mf})}{N_{or}} \right]^{0.4} \cdot g^{-0.2} \quad (4.25)$$

$$C_1 = 2.56 \cdot 10^{-2} \frac{(D/g)^{0.5}}{U_{mf}} \quad (4.26)$$

$$C_2 = \left[C_1^2 + 4 \frac{d_b^{max}}{D} \right]^{0.5} \quad (4.27)$$

$$C_3 = 0.25 \cdot D \cdot (C_1 + C_2)^2 \quad (4.28)$$

$$d_b^{eq} = 0.25 \cdot D \cdot [C_2 - C_1]^2 \quad (4.29)$$

$$\left(\frac{\sqrt{d_b} - \sqrt{d_b^{eq}}}{\sqrt{d_b^{min}} - \sqrt{d_b^{eq}}} \right)^{\frac{(1-C_1)}{C_2}} \left(\frac{\sqrt{d_b} + \sqrt{C_3}}{\sqrt{d_b^{min}} + \sqrt{C_3}} \right)^{\frac{(1+C_1)}{C_2}} = e^{\left[\frac{0.3 \cdot (z-z_0)}{D} \right]} \quad (4.30)$$

Equation (4.30) can be successfully solved with the bisection method described by CHAPRA and CANALE (2006) ²⁵.

As the bubbles rise in the bed, they occupy some fraction of the bed volume. The bubble volume fraction (δ) can be calculated by the following equations (4.31) to (4.34) ⁴:

$$\text{for } U_b < U_f, \quad \delta = \frac{U_0 - U_{mf}}{U_b + 2 \cdot U_{mf}} \quad (4.30)$$

$$\text{for } U_b = U_f, \quad \delta = \frac{U_0 - U_{mf}}{U_b + U_{mf}} \quad (4.31)$$

$$\text{for } U_b = x \cdot U_f, \quad \delta = \frac{U_0 - U_{mf}}{U_b + a \cdot U_{mf}} \quad (4.32)$$

$$a = 1.25 - 0.25 \cdot x, \quad 1 < x < 5$$

$$\text{for } U_b = 5 \cdot U_f, \quad \delta = \frac{U_0 - U_{mf}}{U_b} \quad (4.33)$$

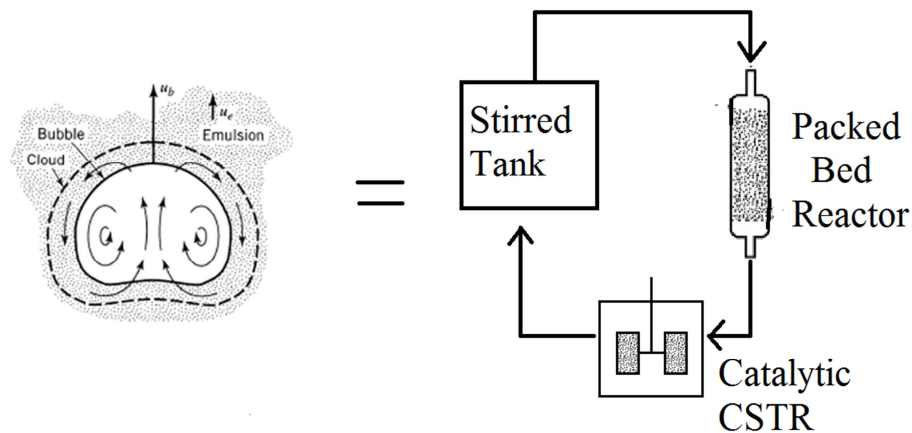
$$\text{for } U_b > 5 \cdot U_f, \quad \delta = \frac{U_0 - U_{mf}}{U_b - U_{mf}} \quad (4.34)$$

Once the cloud and the wake zones carry solids with them, and as the catalytic reactions occur only when the gas reactant contacts such solids, the cloud and wake zones must be included in the reactions calculations.

The gas inside the bubbles circulates in vortex motion until a fraction of gas exit the bubbles by the top. This vortex motion provides a mixture similar to a stirred tank, in which the rotating impeller provides turbulent flow and the outlet composition can be considered equal to the mean composition of the vessel holdup.

Furthermore, the solids in cloud flow down together with the gas, and this behavior can be compared to a plug flow of gas through a bed of particles. As the gas reaches the wake zone a mixture of solids coming from the cloud and dragged by the wake from the bottom of the bed occur, and this mixed flow of solids can be compared to a continuous flow of gas through a stirred tank with catalytic solids on the impeller, in which the gas get perfectly mixed and reacted.

Figure 4.10 – Proposed flowchart of the bubble-cloud-wake system.

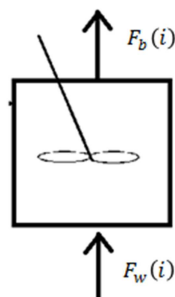


Source: adapted from LEVENSPIEL (1999).³

The model for the bubble-cloud-wake system proposed in this paper consists of a compartment model, with the bubble represented by a stirred tank model, the cloud represented by a packed bed reactor model and the wake represented by a catalytic continuous stirred tank reactor, with gas recirculation through them (figure 4.10).

Considering the bubble to behave as a stirred tank, there are two streams to account: one inlet and one outlet (figure 4.11).

Figure 4.11 – Material balance for the bubble as a stirred tank.



The material balance applied over the tank is:

$$\text{accumulation} = \text{inlet} - \text{outlet} \quad (4.35)$$

For the i -th substance:

$$\frac{dn(i)}{dt} = F_w(i) - F_b(i) \quad (4.36)$$

In equation (4.36), $n(i)$ represents the number of mols, $F_w(i)$ represents the molar flow rate from the wake, and $F_b(i)$ means the molar flow rate out of the bubble, all for the i -th substance.

The number of moles for the i -th substance can be represented by the multiplication of the molar flow rate out of the bubble ($F_b(i)$), by the time the gas takes to circulate, which is the ratio between the volume of bubbles and the volume flow rate:

$$n(i) = F_b(i) \cdot \frac{V_b}{q} \quad (4.37)$$

Substituting $n(i)$ in equation (3.36), it gives:

$$\frac{dF_b(i)}{dt} = [F_w(i) - F_b(i)] \cdot \frac{q}{V_b} \quad (4.38)$$

The equation (4.38) is a first order linear ordinary differential equation, and can be solved by separation and substitution of variables ²⁶:

$$\frac{dF_b(i)}{F_w(i) - F_b(i)} = dt \cdot \frac{q}{V_b} \quad (4.39)$$

$$u = F_w(i) - F_b(i), du = -dF_b(i) \quad (4.40)$$

$$\frac{du}{u} = -dt \cdot \frac{q}{V_b} \quad (4.41)$$

The integration of equation (4.41) from $t = 0$ to t gives:

$$\ln \left[\frac{F_w(i) - F_b(i)}{F_w(i) - F_{b0}(i)} \right] = -\frac{q}{V_b} \cdot t \quad (4.42)$$

And algebraic manipulations finally result in the following equation:

$$F_b(i) = F_w(i) + [F_{b0}(i) - F_w(i)] \cdot e^{-\frac{q}{V_b} \cdot t} \quad (4.43)$$

Equation (4.43) describes the change of the substances molar flow rate in the bubble along the time. Such time is the residence time of bubbles inside the bed of fluidized particles, and is calculated as the ratio between the maximum height of bed H and the bubble velocity:

$$t_R = \frac{H_{max}}{U_b} \quad (4.44)$$

As the bubble velocity is a function of the bubble diameter, and the bubble diameter varies along the height, it is necessary to solve the bed fluid dynamics repeated times.

The material balance applied to the wake zone is done considering the wake as a catalytic Continuous Stirred Tank Reactor (CSTR) operation in steady-state (figure 4.12):

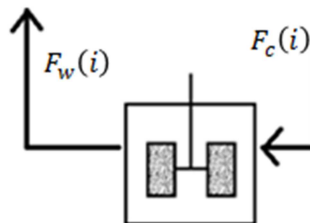
$$inlet - outlet = 0 \quad (4.45)$$

The inlet streams in the wake zone can be considered as $F_c(i)$, the molar flow of the i -th substance coming from the cloud zone, and $F_{cd}(i)$, the molar flow of the i -th substance which counter-diffuses from the catalyst surface. The outlet streams are $F_w(i)$, the molar flow of the i -th substance out of the wake and $F_d(i)$, the molar flow rate of the i -th substance which diffuses to the catalyst surface. This considerations result in the following equation:

$$F_w(i) = F_c(i) - F_d(i) + F_{cd}(i) \quad (4.46)$$

For chemical reactions, in this work is considered that reactants only diffuse to the catalyst and do not counter-diffuse from the solids, and products only counter-diffuse from the catalyst and do not diffuse back. Intermediate products are formed and consumed on the catalyst surface, and the remainder of them is considered to only counter-diffuse from the solids to the gas bulk.

Figure 4.12 – Material balance for the catalytic CSTR.



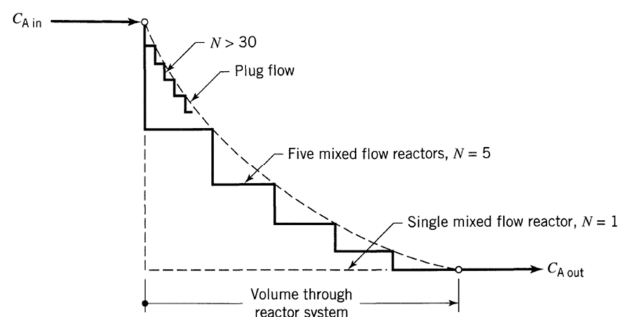
A physical constraint must be included in the material balance, because it is not possible to remove more substance than the quantity that exists in the region of interest. in the case that molar flow rate which diffuses to the catalyst, $F_d(i)$, has a calculated value greater than the molar flow rate coming from the cloud, $F_c(i)$, the

value of $F_d(i)$ must be set as equal to $F_c(i)$, because it is the maximum quantity that can be removed from the gas flow.

The flow of gas and solids in parallel along the cloud can be compared to a plug flow of gas through a Packed Bed Reactor (PBR). Mathematical models for packed bed reactors usually consist of one or more differential equations, seldom linear due to the usually non-linear nature of the kinetics of catalytic reactions. However, for the purpose of this work, a simpler model for the cloud zone is developed. First, it is assumed that the reactions are controlled by mass transfer instead of by the kinetics. Second, according to LEVENSPIEL (1999)³, a high number of CSTRs in series can provide a behavior similar to a plug flow reactor (figure 4.13), and the same can be applied to the catalytic CSTRs and PBR (figure 4.14).

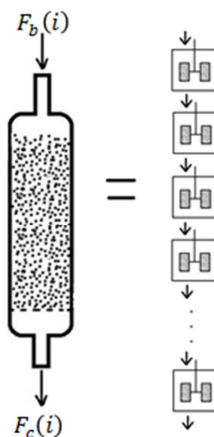
This work propose a series of catalytic CSTRs (the same model described for the wake zone) to describe the cloud zone, as expressed in figure.

Figure 4.13 – Comparison of the result of CSTRs in series and one PFR.



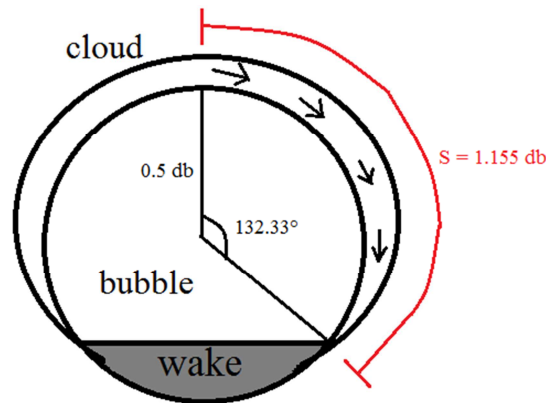
Source: LEVENSPIEL (1999).³

Figure 4.14 – Material balance for a series of catalytic CSTRs.



In order to achieve a more accurate result, it is necessary to use a number of catalytic CSTRs high enough to provide a behavior closer to one PBR. For this purpose, it is necessary to calculate the length of the path of gas and particles in the cloud (figure 4.15), and divide this value by a small enough increment to give a big number of divisions. Each of these divisions is then modeled as one catalytic CSTR and the calculations of the molar flow rates for all substances is performed and repeated till the total number of divisions is reached. It was assumed an increment of 0.01.

Figure 4.15 – Length of the path of gas and particles in the cloud.



For the energy balance, it is assumed that all bubbles have the same temperature, so the energy balance can be performed on one single bubble and the temperature for all the bubbles is obtained. The energy balance is given:

$$\dot{Q} - \dot{W}_s = \Delta\dot{H} + \Delta\dot{E}_k + \Delta\dot{E}_p + \frac{dE}{dt} \quad (4.47)$$

The term of shaft work (\dot{W}_s) is null, the terms for enthalpy variation ($\Delta\dot{H}$), kinetic energy ($\Delta\dot{E}_k$) and potential energy ($\Delta\dot{E}_p$) are all negligible compared to the heat transfer term (\dot{Q}). This results in the following equation:

$$\dot{Q} = \frac{dE}{dt} \quad (4.48)$$

The thermal energy (E), is assumed as dependent only of temperature:

$$E = \frac{\rho}{\bar{M}} \cdot A_{cs} \cdot U_b \cdot \bar{C}_p \cdot T \quad (4.49)$$

In equation (4.49), ρ means the gas density (kg m^{-3}), \bar{M} represents the mean molecular weight (kg kmol^{-1}), A_{cs} is the vessel cross-section area (m^2), U_b is the bubble velocity (m s^{-1}), \bar{C}_p represents the mean molar heat capacity, which is a

function of the temperature T (K). The time derivative of the thermal energy, though, results in the following expression:

$$\frac{dE}{dt} = \frac{\rho}{\bar{M}} \cdot A_{cs} \cdot U_b \cdot \bar{C}_p \cdot \frac{dT}{dt} \quad (4.50)$$

The heat transfer term is described by the next equation:

$$\dot{Q} = h \cdot a_v \cdot A_{cs} \cdot \Delta z \cdot \delta \cdot (T_{oper} - T) \quad (4.51)$$

In equation (4.52), h represents the heat transfer coefficient ($\text{W m}^{-2} \text{K}^{-1}$), a_v is the bubble surface for bubble volume and equal to $\frac{6}{d_b}$ (m^{-1}), Δz is the height increment (m), δ represents the bubble fraction of the bed (m^3 bubbles per m^3 of bed), and T_{oper} is the bed temperature (K), which is controlled by internal bundle of tubes.

In this way, the energy balance becomes:

$$\frac{dT}{dt} = \frac{h \cdot a_v \cdot \Delta z \cdot \delta \cdot \bar{M}}{\rho \cdot U_b \cdot \bar{C}_p} \cdot (T_{oper} - T) \quad (4.53)$$

Equation (4.53) is a first order ordinary differential equation. The mean molar heat capacity is function of the bubble temperature, and the heat transfer coefficient depends on the composition of the Prandtl number and the mean molar heat capacity. Therefore, the equation (4.53) has coefficients dependents of the temperature and could be solved by integrating factors.²⁶ However, the mathematical form of the mean heat capacity is unknown and may be different for each particular reactive system, so a general solution for equation (4.53) is not practical.

Furthermore, fluidized beds with very exothermic reactions usually have a very steep increase on the bubble gas temperature. So, numerical solutions of these stiff problems by explicit methods are expected to fail. Implicit methods of higher order are needed to solve stiff problems with the necessary accuracy.²⁷ However, such numerical methods represent higher computational effort and can turn the model coupling in commercial process simulator difficult due to the possible long time the model would waste to run.

In this work a hybrid approach was performed. First, it was assumed that all coefficients are constants and the equation (4.53) was solved analytically:

$$\theta = \frac{h \cdot a_v \cdot \Delta z \cdot \delta \cdot \bar{M}}{\rho \cdot U_b \cdot \bar{C}_p} \quad (4.54)$$

$$\frac{dT}{T_{oper} - T} = \theta \cdot dt \quad (4.55)$$

$$\ln\left(\frac{T_{oper} - T}{T_{oper} - T_0}\right) = -\theta \cdot t \quad (4.56)$$

$$t = \frac{z}{U_b} \quad (4.57)$$

$$T = T_{oper} - (T_{oper} - T_0) \cdot e^{-\frac{h \cdot a_v \cdot \Delta z \cdot \delta \cdot \bar{M}}{\rho \cdot U_b^2 \cdot C_p} z} \quad (4.58)$$

Second, the algebraic equation (4.58) is now assumed to have the parameter θ , dependent on the temperature, and the equation (4.59) is solved numerically, with T_0 assumed as the temperature at the previous node.

$$T_{z+\Delta z} = T_{oper} - (T_{oper} - T_z) \cdot e^{-\frac{h \cdot a_v \cdot \Delta z \cdot \delta \cdot \bar{M}}{\rho \cdot U_b^2 \cdot C_p} z} \quad (4.59)$$

4.2.2 - Emulsion

The general two-phase theory proposes that the emulsion gas stays at minimum fluidization condition. However, this hypothesis was proven to be false, and it was proposed that the emulsion gas velocity can be calculated from the minimum bubbling conditions and the solids downward velocity ⁴.

The cloud volume fraction in relation to bubble volume (f_c) is defined by the following equation ¹⁸:

$$f_c = \frac{3}{U_{br} \frac{\epsilon_{mf}}{U_{mf}} - 1} \quad (4.60)$$

From the assumption of the spherical cap shape for the bubbles, it is proposed that the wake volume fraction in relation to bubble volume (f_w) is equal to 0.07129. Therefore, the volume fraction of emulsion in relation to the bed volume (f_e), excluding the wakes, is expressed in Equation (4.61):

$$f_e = 1 - \delta - f_w \delta \quad (4.61)$$

The solids downward velocity is calculated by the following equation ⁴:

$$U_{s,down} = \frac{f_w}{f_e} \cdot \delta \cdot U_b \quad (4.62)$$

The emulsion gas velocity is then defined as ⁴:

$$U_e = \frac{U_{mb}}{\epsilon_{mb}} - U_{s,down} \quad (4.63)$$

The solids are dragged up by the wake below the bubbles, and in the emulsion the solids flow downward. In commercial-scale operations with Geldart A solids, the solids downflow can be faster than the gas upflow and the emulsion gas is forced to flow downward.⁴

The pressure drop for packed beds can be estimated by the Ergun equation²⁸:

$$\frac{\Delta P}{L} = 150 \cdot \frac{\mu(1-\epsilon)^2}{\epsilon^3(\varphi_s \bar{d}_p)^2} \cdot U_0 + 1.75 \cdot \frac{(1-\epsilon)\rho_g}{\epsilon^3 \varphi_s \bar{d}_p} \cdot U_0^2 \quad (4.64)$$

As before fluidization begins the bed is originally a packed bed, the minimum fluidization conditions can be calculate from a combination of the Ergun equation and the fluidization condition of drag force equal the bed weight, resulting in the equation (4.65). When the minimum fluidization velocity is determined from experiments, the minimum fluidization porosity (ϵ_{mf}) can be calculated by equations (4.65) to (4.67).

$$\frac{1.75}{\epsilon_{mf}^3 \varphi_s} \cdot Re_{p,mf}^2 + \frac{150(1-\epsilon_{mf})}{\epsilon_{mf}^3 \varphi_s^2} \cdot Re_{p,mf} = Ar \quad (4.65)$$

$$Re_{p,mf} = \frac{\bar{d}_p U_{mf} \rho_g}{\mu} \quad (4.66)$$

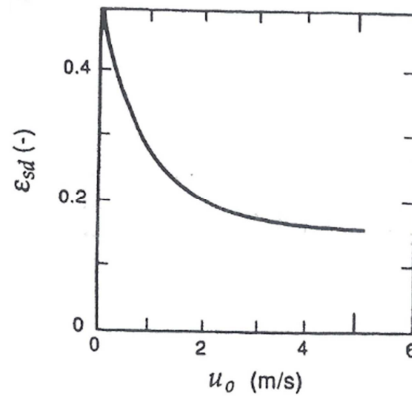
$$Ar = \frac{\bar{d}_p^3 \rho_g (\rho_s - \rho_g)}{\mu^2} \quad (4.67)$$

Researchers have proposed an equation to calculate the emulsion porosity of fine (Group A) powders in function of the minimum fluidization conditions and the emulsion velocity²⁹.

$$\left(\frac{\epsilon_e}{\epsilon_{mf}} \right)^3 \left(\frac{1-\epsilon_{mf}}{1-\epsilon_e} \right) = \left(\frac{U_e}{U_{mf}} \right)^{0.7} \quad (4.68)$$

KUNII and LEVENSPIEL (1991)⁴, provided a plot (figure 4.16) to correlate the solids fraction on dense zone of fluidized beds with data from SCHNITZLEIN (1987)³⁰.

Figure 4.16 – Solids fraction in dense zone of fluidized beds versus gas velocity.



Source: KUNII and LEVENSPIEL (1991).⁴

Non-linear regression done over these data provided the following equation to describe the solids fraction in dense zone:

$$\epsilon_{sd} = 0.121182 + \frac{0.163087}{U_0^{1.039231}} \quad R^2 = 0.998707 \quad (4.69)$$

The bubbling bed pressure drop along the height is approximately equal to the static head of bed solids.^{4,10}

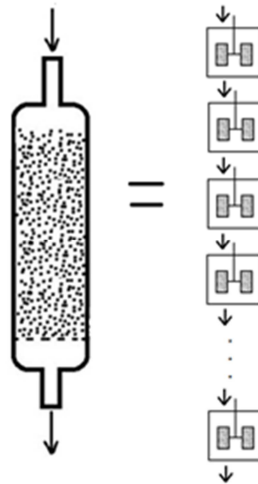
$$\Delta P_b = \rho_b \cdot g \cdot \Delta z \quad (4.70)$$

$$\rho_b = \rho_s \cdot \epsilon_{sd} \quad (4.71)$$

In equation (4.70), ρ_b is the bulk density of the bed (kg m^{-3}), g is the gravity acceleration (m s^{-2}) and Δz is the height increment (m). In equation (4.71), ρ_s is the solids density (kg m^{-3}).

Chemical reactions in the emulsion gas phase are proposed to follow the same model which rules the cloud zone in the bubble-cloud-wake system, i.e., a series of catalytic CSTRs (figure 4.17).

Figure 4.17 – Proposed scheme of reactors combination in emulsion phase.



4.3 – Splash Zone

In the splash zone, the bubbles pop up and the gases at the bubble, cloud and wake zones get mixed. Meanwhile, two possibilities may occur:

1 - Gas mix from the bubbles pop get mixed with the upflowing gas from the emulsion.

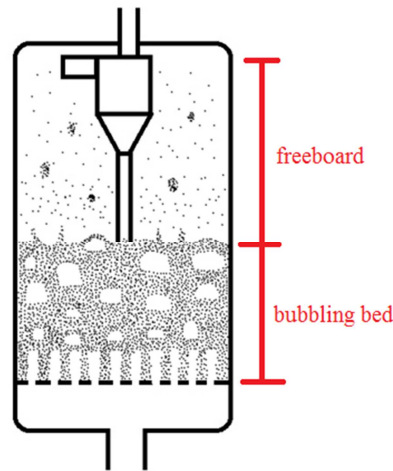
2 - Circa two thirds of the mixed gas flows back the bed as emulsion gas. This emulsion gas flows downward the fluidized bed and gets mixed with gas bubbles at the distributor exit.

The second possibility occurs often with Geldart A solids in commercial-scale operations.⁴

4.4 – Freeboard

The freeboard is the region above the bubbling bed surface. Particles are sprayed up the freeboard mainly by three reasons: As the gas inside the bubbles has pressure higher than the bed surface, they pop and eject clumps of solids; Bubbles are usually faster than the surrounding medium, so the solids dragged in the wake are thrown upward the freeboard; and for last, very energetic ejections of solids occur when two bubbles coalesce just as they reach the surface of the bed.⁴

Figure 4.18 – Distinction between the bubbling bed and the freeboard.



In fluidized beds, as solids are thrown to the freeboard, some larger particles fall back to the bed and some finer particles are carried out of the vessel. This separation of fines from a mixture of solids is called *elutriation*, and depends on the velocity of gas and the size distribution of particles. ⁴

Elutriation of solids can be calculated by the terminal velocity of each size of particle of the particles size distribution. For each fraction of solids with terminal velocity equal or greater than the velocity of gas, this fraction of solids is not elutriated, in other words, particles of such size fall back to the bed after being ejected to the freeboard. This way, the size distribution of the elutriated particles can be estimated and the cyclones can be designed for more efficient recover of fines.

The terminal velocity of particles, U_t , can be calculated by the equation:

$$U_t = \left[\frac{4d_p(\rho_s - \rho_g)g}{3\rho_g C_D} \right]^{0.5} \quad (4.72)$$

The drag coefficient, C_D , is experimentally determined. HAIDER and LEVENSPIEL (1989) ³¹, proposed an equation for the C_D (-):

$$C_D = \frac{24}{Re_p} \left[1 + (8.1716 \cdot e^{-4.0655 \cdot \phi_s}) Re_p^{0.0964 + 0.5565 \phi_s} \right] + \frac{73.69 \cdot (e^{-5.0748 \cdot \phi_s}) Re_p}{Re_p + 5.378 \cdot e^{6.2122 \phi_s}} \quad (4.73)$$

With:

$$Re_p = \frac{d_p U_0 \rho_g}{\mu} \quad (4.74)$$

φ_s is the particle sphericity (from zero to one).

The terminal velocity can also be calculated by the following equations³¹:

$$d_p^* = d_p \left[\frac{\rho_g(\rho_s - \rho_g)g}{\mu^2} \right]^{1/3} \quad (4.75)$$

$$U_t^* = \left[\frac{18}{(d_p^*)^2} + \frac{2.335 - 1.744\varphi_s}{(d_p^*)^{0.5}} \right]^{-1}, \quad 0.5 < \varphi_s < 1 \quad (4.76)$$

$$U_t = U_t^* \left[\frac{\mu(\rho_s - \rho_g)g}{\rho_g^2} \right]^{1/3} \quad (4.77)$$

Larger particles fall back to the bubbling bed. However, particles with larger diameters have higher terminal velocity and therefore tend to reach only till lower heights of the freeboard, while particles with smaller diameters have lower terminal velocity and therefore tend to reach until higher heights of the freeboard and even be elutriated. This behavior provides a distribution of the bulk density of solids along the freeboard and it has significant impact over the reactor performance.

One of the parameters used for diffusion calculations is the catalyst surface, which depends on the mass of solids. Along the freeboard height, the bulk density of solids varies, and therefore the mass of solids and the catalyst surface also vary.

These calculations rely primary on three variables: the differential volume of the freeboard $V_{\Delta z}$, the mass of one particle m_{1p} , and the catalyst surface of one particle $S_{cat_{1p}}$, described respectively by equation (4.78) to (4.79).

$$V_{\Delta z} = A_{cs}\Delta z \quad (4.78)$$

$$m_{1p} = \rho_s \cdot \frac{1}{6}\pi(\varphi_s d_p)^3 \quad (4.79)$$

$$S_{cat_{1p}} = \pi(\varphi_s d_p)^2 \quad (4.80)$$

The mass of solids at the freeboard height z m_{s_z} , is the differential volume of freeboard multiplied by the bulk density of solids at the height z ρ_{b_z} , as in equation (4.81):

$$m_{s_z} = \rho_{b_z} V_{\Delta z} \quad (4.81)$$

The number of particles at the freeboard height z Np_{fb_z} , is the mass of solids at the freeboard height z divided the mass of one particle m_{1p} , as in equation (4.82):

$$Np_{fb_z} = \frac{m_{s_z}}{m_{1p}} \quad (4.82)$$

The catalyst surface at the freeboard height z is the number of particles at the freeboard height z multiplied by the catalyst surface of one particle, as in equation (4.83):

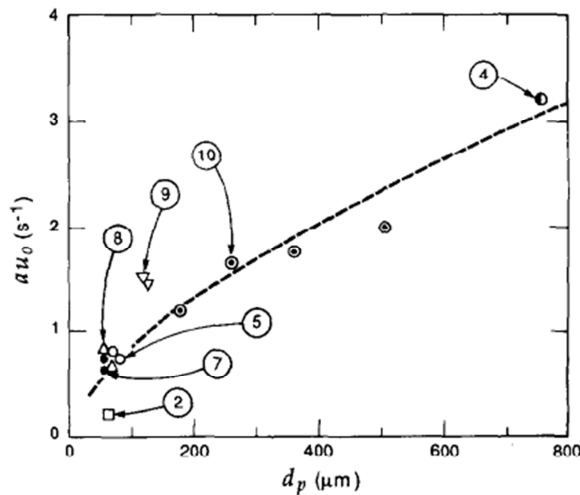
$$S_{cat_z} = Np_{fb_z} S_{cat_{1p}} \quad (4.83)$$

According to KUNII and LEVENSPIEL (1990)³², the bulk density of solids in the freeboard falls off exponentially from the value at the bed surface, which in this paper is considered the same at the dense bed.

$$\rho_{b_z} = \rho_b e^{-a \cdot z} \quad (4.84)$$

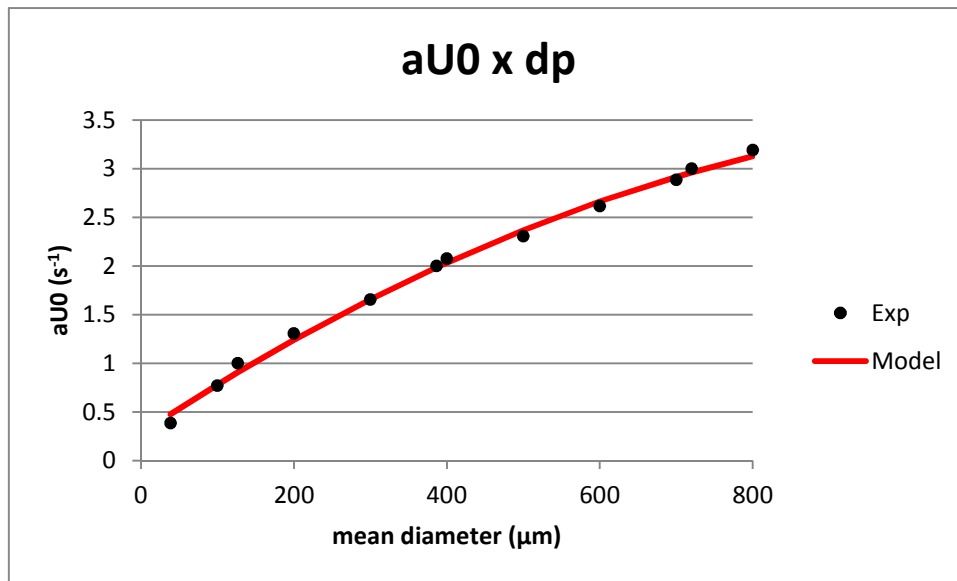
In the same paper, the authors provided a chart (figure 4.19) for the decay constant a from equation (4.84). Such chart shows the dependency of the decay rate aU_0 with the particle diameter, in micra.

Figure 4.19 – Decay rate versus particle diameter.



Source: KUNII and LEVENSPIEL (1990)³².

Data were collected from this chart, plotted and fit to a quadratic equation by multiple linear regression, as described by MONTGOMERY and RUNGER (1999)³³. The equation (4.85) and figure 4.20 is the result of this fit.

Figure 4.20 – Plot of aU_0 versus d_p .

$$aU_0 = 0.27791664 + 0.00521358 \cdot d_p - 2.06684377 \cdot 10^{-6} (d_p)^2 \quad (4.85)$$

$$R^2 = 0.996016$$

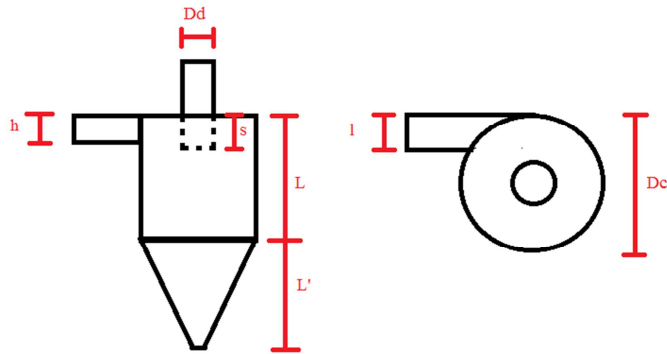
4.5 – Cyclones

Cyclone is an equipment that is used for separation of solids or liquid droplets from a gas stream by use of a centrifugal force. It is made by a vertical cylinder with conical bottom, a tangential inlet near the top, and an outlet for dust at the bottom of the cone. The clean gas outlet is at the top of the cyclone and is a pipe extended into the cylinder body to avoid short-circuiting of air from inlet to outlet. ³⁴

Cyclones can operate with dry or humid gas, from low to high temperature and pressure. Collection efficiency is high for particles bigger than 10 micra, and for particles smaller the cyclone diameter must be very small and therefore provides a high pressure drop. ³⁵

According to MACINTYRE (1990) ³⁶, the pressure drop on a cyclone can be calculated based on its measurements. Measurements for high and medium efficiency cyclone are on the table (4.2) and are related to the figures 4.21 and 4.22. GOMIDE (1980) ³⁵, describes such cyclones as *Stairmand-Kelsey* cyclones.

Figure 4.21 – Measurements of a cyclone.



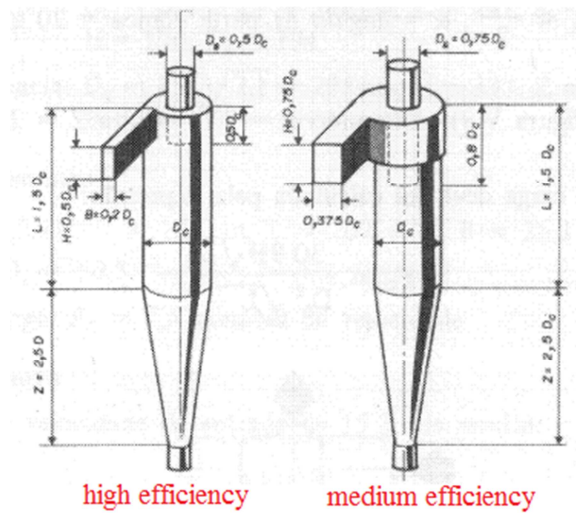
Source: Made based on data from MACINTYRE (1990).³⁶

Table 4.2 – Cyclone measurements values for high and medium efficiency equipment.

Measurement	High Eff.	Medium Eff.
h	0.5 D _c	0.75 D _c
l	0.2 D _c	0.375 D _c
D _d	0.5 D _c	0.875 D _c
s	0.5 D _c	0.75 D _c
L	1.5 D _c	1.5 D _c
L'	2.5 D _c	2.5 D _c

Source: MACINTYRE (1990).³⁶

Figure 4.22 – High and medium efficiency Stairmand-Kelsey cyclones.



Source: adapted from GOMIDE (1980).³⁵

The pressure drop calculation begins with the measurements values calculated in feet from the value of the cyclone diameter (the cyclone already installed in the fluidized bed). Next, the following equation is used to calculate the pressure drop in inches of water (inW):

$$\Delta P(inW) = \frac{12 \cdot l \cdot h}{K \cdot D_d^2 \sqrt{\frac{L}{D_c}} \sqrt{\frac{L'}{D_c}}} \quad (4.86)$$

In equation (4.86), K represents a factor which depends on the inlet structure: it equals 0.5 for a no deflector inlet, it equals 1 for straight deflector and it equals 2 for expanding deflector (figure 4.23).

Figure 4.23 – Inlet structures of the cyclone.³⁵

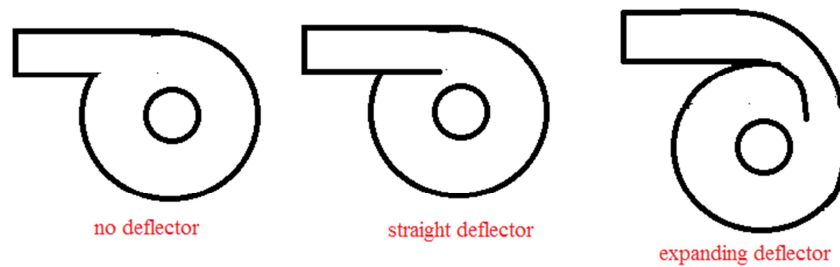


Table 4.3 – Deflector position and K value.

Position	K
No deflector	0.5
Straight	1
Expanding	2

Source: MACINTYRE (1990).³⁶

After calculated, the pressure drop in inches of water can be converted to kilopascals (kPa):

$$\Delta P (kPa) = \frac{101.3}{407.1} \cdot \Delta P(inW) \quad (4.87)$$

4.6 – Model Structure

The multiple-region model proposed has a sequential structure (figure 4.24). The algorithm begins with the distributor model processing the required input from the data transfer submodule, followed by a preliminary fluid dynamics calculation block, in which the main fluidization parameters for the entire algorithm are calculated.

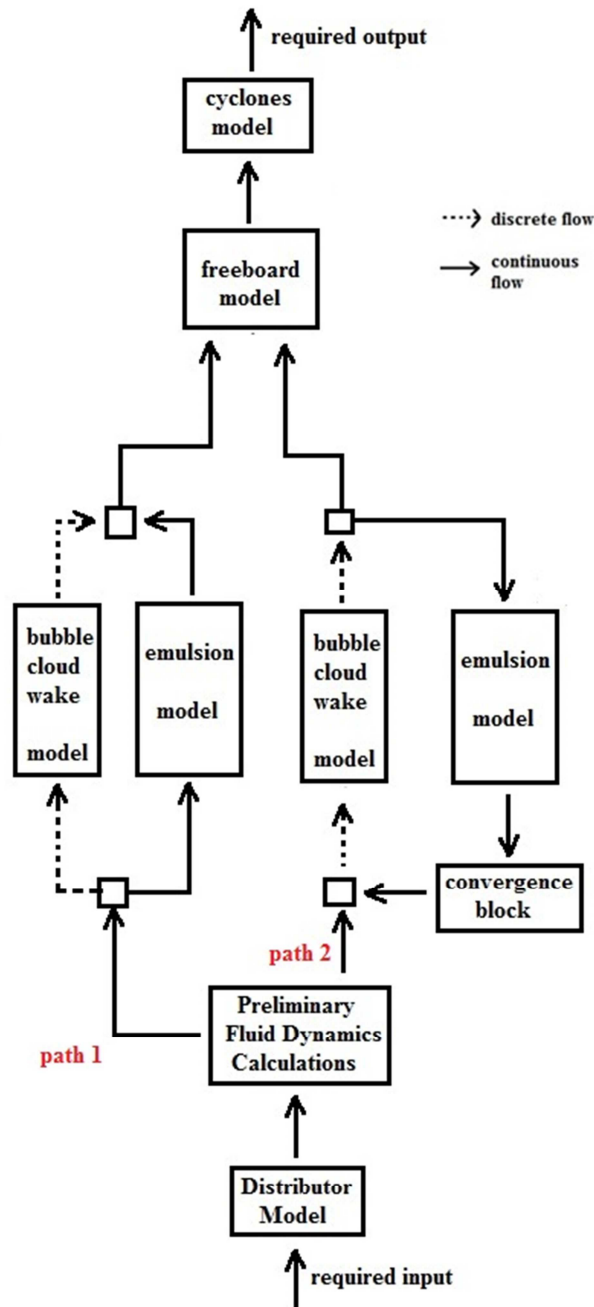
After then, there are two possible calculation paths, which are chosen based on the emulsion gas velocity calculated in the preliminary fluid dynamics block. In the case the emulsion gas velocity is positive (i.e., the emulsion gas flows upward), the algorithm calculates through path one, otherwise, it calculates through path two.

Path one is a more sequential calculation route, and it consists of two parallel blocks: the bubble-cloud-wake model and the emulsion model. Feed for models are the bubble gas flow rate for bubble-cloud-wake model and emulsion gas flow rate for emulsion model. Both flow rates are calculated at the preliminary fluid dynamics calculations block.

Path two is a closed-loop structure due to the downward emulsion gas flow. Therefore, this recycled gas is adopted as a *tear stream* and a convergence block is used to compare the estimated recycled gas composition and flow rate with the calculated. The same strategy to converge flowsheets in modular simulation is used to converge the composition in the calculation path two.

Then, the algorithm calculates the freeboard model and the cyclones model in sequence, providing the required output to the data transfer submodule.

Figure 4.24 – Model structure.



4.6.1 - Required Input

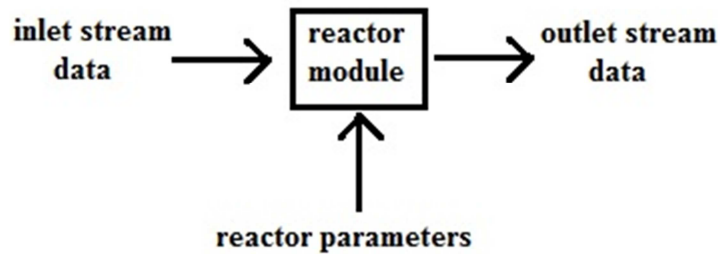
Some important data is necessary to initialize the model and start mathematical solution. Such data is divided in two categories: stream variables and reactor parameters (figure 4.25). Stream variables are extracted from the inlet streams, and consist of temperature, pressure and species molar flow rate. Reactor parameters are divided in five subcategories: particles, gas, geometry, reactions and operation parameters.

Particles parameters consist of mean particle diameter (\bar{d}_p), particle density (ρ_s), particle sphericity (φ_s) and minimum fluidization velocity (U_{mf}). Gas parameters consist of gas density (ρ_g), viscosity (μ), diffusivity (D_{dif}), thermal conductivity (k_g) and number of chemical species (N_{comp}).

The geometry parameters are essentially the physical dimensions of the industrial reactor, and consist of the diameter (D), height (H), bed height (H_b), for perforated plate distributor, the number of orifices (N_{or}) and the orifice diameter (d_{or}), and for tuyeres distributor, number of orifices for tuyere ($N_{or/ty}$), number of tuyeres (N_{ty}), and tuyere height (z_0) in addition to the orifice diameter.

Reactions parameters consist basically in the number of chemical reactions in the reactive system (N_{rxn}), for the correct indexing of reactions and calls of kinetic model functions. Operation parameters are the superficial velocity of gas (U_0) and the bed operation temperature (T_{oper}), which is controlled by heat transfer.

Figure 4.25 – Required input and output



4.6.2 - Distributor Model

The distributor model consists of equations (4.1) to (4.5).

$$A_{or} = N_{or} \cdot \frac{\pi d_{or}^2}{4} \quad (4.1)$$

$$U_{or} = \frac{U_0}{A_{or}} \quad (4.2)$$

$$\Delta P_d = \frac{\rho_g}{2} \left(\frac{U_{or}}{C_{d,or}} \right)^2 \quad (4.3)$$

$$Re = \frac{D_t U_0 \rho_g}{\mu} \quad (4.4)$$

$$C_{d,or} = 0.59991 \cdot e^{\left(\frac{50.53866}{Re} \right)}, \text{ for } 100 < Re \leq 3000 \quad (4.5)$$

$$C_{d,or} = 0.6, \text{ for } Re > 3000, \quad R^2 = 0.999198$$

4.6.3 - Preliminary Fluid Dynamics Calculations Block

This calculation block consists of two stages: the first with constant parameters calculated by fluidization correlations, and the second with variables dependent of the bed height. In stage one, the reactor cross-section area (A_{cs}), gas flow rate (Q_t), the dense bed porosity (ϵ_{sd}), the bed bulk density (ρ_b), the bubbling bed pressure drop (ΔP_b) and the minimum fluidization porosity are calculated.

$$A_{cs} = \frac{\pi(D)^2}{4} \quad (4.88)$$

$$Q_t = U_0 A_{cs} \quad (4.89)$$

$$\epsilon_{sd} = 0.121182 + \frac{0.163087}{U_0^{1.039231}} \quad R^2 = 0.998707 \quad (4.69)$$

$$\rho_b = \rho_s \cdot \epsilon_{sd} \quad (4.71)$$

$$\Delta P_b = \rho_b \cdot g \cdot \Delta z \quad (4.70)$$

$$\frac{1.75}{\epsilon_{mf}^3 \varphi_s} \cdot Re_{p,mf}^2 + \frac{150(1 - \epsilon_{mf})}{\epsilon_{mf}^3 \varphi_s^2} \cdot Re_{p,mf} = Ar \quad (4.65)$$

$$Re_{p,mf} = \frac{\bar{d}_p U_{mf} \rho_g}{\mu} \quad (4.66)$$

$$Ar = \frac{\bar{d}_p^3 \rho_g (\rho_s - \rho_g)}{\mu^2} \quad (4.67)$$

Equation 4.65 is solved numerically by Newton method.

Some parameters for the solids distribution are also calculated: the number of particles in the cloud ($Np_{cloud_{\Delta z, \Delta s}}$), in the wake ($Np_{wake_{\Delta z, \Delta s}}$) and in the emulsion ($Np_{emulsion_{\Delta z}}$). Such equations are found in the Appendix C.

The second stage consists of calculations of height-dependent parameters at the distributor exit. Such parameters are bubble diameter (d_b), bubble rise velocity (U_{br}), bubble velocity (U_b), solids downward velocity ($U_{s,down}$) and emulsion gas velocity (U_e). Equations for this stage are the following:

$$d_b^{max} = 2.59 \cdot [A_{ts}(U_0 - U_{mf})]^{0.4} \cdot g^{-0.2} \quad (4.24)$$

$$d_b^{min} = 1.38 \cdot \left[A_{ts} \frac{(U_0 - U_{mf})}{N_{or}} \right]^{0.4} \cdot g^{-0.2} \quad (4.25)$$

$$C_1 = 2.56 \cdot 10^{-2} \frac{(D/g)^{0.5}}{U_{mf}} \quad (4.26)$$

$$C_2 = \left[C_1^2 + 4 \frac{d_b^{max}}{D} \right]^{0.5} \quad (4.27)$$

$$C_3 = 0.25 \cdot D \cdot (C_1 + C_2)^2 \quad (4.28)$$

$$d_b^{eq} = 0.25 \cdot D \cdot [C_2 - C_1]^2 \quad (4.29)$$

$$\left(\frac{\sqrt{d_b} - \sqrt{d_b^{eq}}}{\sqrt{d_b^{min}} - \sqrt{d_b^{eq}}} \right)^{\frac{(1-C_1)}{C_2}} \left(\frac{\sqrt{d_b} + \sqrt{C_3}}{\sqrt{d_b^{min}} + \sqrt{C_3}} \right)^{\frac{(1+C_1)}{C_2}} = e^{\left[\frac{-0.3 \cdot (z-z_0)}{D} \right]} \quad (4.30)$$

$$U_{br} = 0.711 \sqrt{g d_b}, \quad \frac{d_b}{D} < 0.125 \quad (4.14)$$

$$U_{br} = 1.2 \cdot [0.711 \sqrt{g d_b}] e^{\left(-1.49 \frac{d_b}{D} \right)}, \quad 0.125 < \frac{d_b}{D} < 0.6 \quad (4.15)$$

$$U_b = K + U_{br} \quad (4.16)$$

For Geldart A solids, it was proposed that ^{4,20}:

$$K = 1.55 \cdot D^{0.32} [(U_0 - U_{mf}) + 14.1(d_b + 0.005)] \quad (4.17)$$

For Geldart B solids, it was proposed that ^{4,20}:

$$K = 1.6 \cdot D^{1.35} [(U_0 - U_{mf}) + 1.13 d_b^{0.5}] \quad (4.18)$$

For Geldart D solids, it was proposed that ¹⁸:

$$K = U_0 - U_{mf} \quad (4.19)$$

$$f_w = 0.07129 \quad (4.90)$$

$$U_f = \frac{U_{mf}}{\epsilon_{mf}} \quad (4.22)$$

$$\text{for } U_b < U_f, \quad \delta = \frac{U_0 - U_{mf}}{U_b + 2 \cdot U_{mf}} \quad (4.30)$$

$$\text{for } U_b = U_f, \quad \delta = \frac{U_0 - U_{mf}}{U_b + U_{mf}} \quad (4.31)$$

$$\text{for } U_b = x \cdot U_f, \quad \delta = \frac{U_0 - U_{mf}}{U_b + a \cdot U_{mf}} \quad (4.32)$$

$$a = 1.25 - 0.25 \cdot x, \quad 1 < x < 5$$

$$\text{for } U_b = 5 \cdot U_f, \quad \delta = \frac{U_0 - U_{mf}}{U_b} \quad (4.33)$$

$$\text{for } U_b > 5 \cdot U_f, \quad \delta = \frac{U_0 - U_{mf}}{U_b - U_{mf}} \quad (4.34)$$

$$f_e = 1 - \delta - f_w \delta \quad (4.61)$$

$$U_{s,down} = \frac{f_w}{f_e} \cdot \delta \cdot U_b \quad (4.62)$$

$$U_e = \frac{U_{mb}}{\epsilon_{mb}} - U_{s,down} \quad (4.63)$$

For Geldart A solids, ABRAHAMSEN and GELDART (1980)²⁹, proposed an equation to calculate the minimum bubbling velocity of solids:

$$\frac{U_{mb}}{U_{mf}} = 2300 \cdot \frac{\rho_g^{0.126} \mu^{0.523} e^{(0.716 \cdot w_{45\mu m})}}{\bar{d}_p^{0.8} g^{0.954} (\rho_s - \rho_g)^{0.934}} \quad (4.91)$$

In equation (4.91), ρ_g is the gas density (kg m^{-3}), ρ_s is the solid density (kg m^{-3}), μ is the gas viscosity (Pa s), \bar{d}_p is the particle mean diameter (m), g is the gravity acceleration (m s^{-2}), U_{mf} is the minimum fluidization velocity (m s^{-1}), U_{mb} is the minimum bubbling velocity (m s^{-1}) and $w_{45\mu m}$ is the mass fraction of particles lower than 45 micra.

Another equation proposed by GELDART and ABRAHAMSEN (1978)³⁷, also predicts the minimum bubbling velocity:

$$\frac{U_{mb}}{U_{mf}} = 4.125 \cdot 10^4 \cdot \frac{\mu^{0.9} \rho_g^{0.1}}{(\rho_s - \rho_g) \cdot g \cdot \bar{d}_p} \quad (4.92)$$

For Geldart B solids, the minimum fluidization and bubbling velocities are equal. The minimum bubbling porosity ϵ_{mb} is calculated by the same way as the minimum fluidization porosity ϵ_{mf} .

In the case the emulsion gas velocity is positive, i.e., $U_e > 0$, the algorithm chooses path one, otherwise, it chooses the path two.

4.6.4 - Bubble-Cloud-Wake Model

This model treats the bubbles as a discrete phase and calculates parameters and variables in transient mode, because bubbles stay in the reactor since the time zero (at the bottom of the bed) to the mean residence time (at the top of the bed).

As the calculated quantities are changing with height and are dependents of fluidization parameters which vary with height, the model must perform some fluid dynamics calculations performed in the block before. Such equations are the bubble diameter (d_b), the bubble rise velocity (U_{br}), the bubble velocity (U_b), bubble volume fraction (δ), and the volume of bubbles (V_b). For each increment of height, the following equations are solved:

$$d_b^{max} = 2.59 \cdot [A_{ts}(U_0 - U_{mf})]^{0.4} \cdot g^{-0.2} \quad (4.24)$$

$$d_b^{min} = 1.38 \cdot \left[A_{ts} \frac{(U_0 - U_{mf})}{N_{or}} \right]^{0.4} \cdot g^{-0.2} \quad (4.25)$$

$$C_1 = 2.56 \cdot 10^{-2} \frac{(D/g)^{0.5}}{U_{mf}} \quad (4.26)$$

$$C_2 = \left[C_1^2 + 4 \frac{d_b^{max}}{D} \right]^{0.5} \quad (4.27)$$

$$C_3 = 0.25 \cdot D \cdot (C_1 + C_2)^2 \quad (4.28)$$

$$d_b^{eq} = 0.25 \cdot D \cdot [C_2 - C_1]^2 \quad (4.29)$$

$$\left(\frac{\sqrt{d_b} - \sqrt{d_b^{eq}}}{\sqrt{d_b^{min}} - \sqrt{d_b^{eq}}} \right)^{\frac{(1-C_1)}{C_2}} \left(\frac{\sqrt{d_b} + \sqrt{C_3}}{\sqrt{d_b^{min}} + \sqrt{C_3}} \right)^{\frac{(1+C_1)}{C_2}} = e^{\left[\frac{0.3 \cdot (z-z_0)}{D} \right]} \quad (4.30)$$

$$U_{br} = 0.711 \sqrt{g d_b}, \quad \frac{d_b}{D} < 0.125 \quad (4.14)$$

$$U_{br} = 1.2 \cdot [0.711 \sqrt{g d_b}] e^{\left(-1.49 \frac{d_b}{D} \right)}, \quad 0.125 < \frac{d_b}{D} < 0.6 \quad (4.15)$$

$$U_b = K + U_{br} \quad (4.16)$$

For Geldart A solids, it was proposed that ^{4,20}:

$$K = 1.55 \cdot D^{0.32} [(U_0 - U_{mf}) + 14.1(d_b + 0.005)] \quad (4.17)$$

For Geldart B solids, it was proposed that ^{4,20}:

$$K = 1.6 \cdot D^{1.35} [(U_0 - U_{mf}) + 1.13d_b^{0.5}] \quad (4.18)$$

For Geldart D solids, it was proposed that ¹⁸:

$$K = U_0 - U_{mf} \quad (4.19)$$

$$f_w = 0.07129 \quad (4.90)$$

$$U_f = \frac{U_{mf}}{\epsilon_{mf}} \quad (4.22)$$

$$\text{for } U_b < U_f, \delta = \frac{U_0 - U_{mf}}{U_b + 2 \cdot U_{mf}} \quad (4.30)$$

$$\text{for } U_b = U_f, \delta = \frac{U_0 - U_{mf}}{U_b + U_{mf}} \quad (4.31)$$

$$\text{for } U_b = x \cdot U_f, \delta = \frac{U_0 - U_{mf}}{U_b + a \cdot U_{mf}} \quad (4.32)$$

$$a = 1.25 - 0.25 \cdot x, \quad 1 < x < 5$$

$$\text{for } U_b = 5 \cdot U_f, \delta = \frac{U_0 - U_{mf}}{U_b} \quad (4.33)$$

$$\text{for } U_b > 5 \cdot U_f, \delta = \frac{U_0 - U_{mf}}{U_b - U_{mf}} \quad (4.34)$$

$$f_e = 1 - \delta - f_w \delta \quad (4.61)$$

$$V_b = A_{cs} \cdot H_{max} \cdot \delta \quad (4.93)$$

$$S = 1.155 \cdot d_b \quad (4.63)$$

After the fluid dynamics calculations, the model for the bubble stage solves the following equations:

$$\Delta t = \frac{\Delta z}{U_b} \quad (4.94)$$

$$t = t + \Delta t \quad (4.95)$$

$$\alpha = \frac{q}{V_b} \quad (4.96)$$

$$F_b(i) = F_w(i) + [F_{b0}(i) - F_w(i)] \cdot e^{-\alpha t} \quad (4.43)$$

$$t_R = \frac{H_{max}}{U_b} \quad (4.44)$$

Then, the calculations begin for the cloud stage, with the initialization of the initial values:

$$F_s(i) = F_b(i) \quad (4.97)$$

Then, the diffused molar flow rates $F_d(i)$ are calculated by particle-to-gas mass transfer correlations stated at appendice A. The counter-diffused molar flow rates $F_{cd}(i)$ are calculated at the particle temperature and by chemical reactions calculations. Procedure for such calculations are stated at appendice B. The cloud subdivision outlet molar flow rate is calculated from the material balance:

$$F_{s+\Delta s}(i) = F_s(i) - F_d(i) + F_{cd}(i) \quad (4.98)$$

A physical constrain must be added to this equation in order to avoid the result to be negative. Such constrain is that if the diffused molar flow rate $F_d(i)$ has a calculated value higher than the inlet molar flow rate $F_s(i)$, than the diffused molar flow rate is set as equal to the inlet molar flow rate, because it is not possible to remove more material than the available.

Next step is the cloud path increment and evaluation:

$$s = s + \Delta s \quad (4.99)$$

$$\text{if } s < S: F_s(i) = F_{s+\Delta s}(i) \quad (4.100)$$

$$\text{if } s \geq S: F_c(i) = F_{s+\Delta s}(i) \quad (4.101)$$

While the condition $s < S$ is true, equation (4.100) is solved and the calculations loop to $F_d(i)$ and $F_{cd}(i)$. Otherwise, the cloud outlet molar flow rate $F_c(i)$ is set by equation (4.101).

Once the loop is bypassed, the calculations at the wake stage begin. The diffused and counter-diffused molar flow rates are calculated by the same procedures at the cloud stage. After such calculations, the wake outlet molar flow rate is then calculated by equation (4.46):

$$F_w(i) = F_c(i) - F_d(i) + F_{cd}(i) \quad (4.46)$$

The height coordinate z is then incremented and the bed height is evaluated.

$$z = z + \Delta z \quad (4.102)$$

Also, the bubble gas temperature is numerically calculated by the equation (3.59) through the fixed-point iteration method, due to the dependency of the heat transfer coefficient h and the mean molar heat capacity $\overline{C_p}$ on the temperature $T_{z+\Delta z}$:

$$T_{z+\Delta z} = T_{oper} - (T_{oper} - T_z) \cdot e^{-\frac{h \cdot a_p \cdot \Delta z \cdot \delta \cdot \overline{M}}{\rho \cdot U_b^2 \cdot \overline{C_p}} \cdot z} \quad (4.59)$$

Bed Pressure is also calculated at this point of the model, by the following equation:

$$P_{z+\Delta z} = P_z - \Delta P_b \quad (4.103)$$

If the height z is lower than the bed height, the whole block of equations is solved again from the fluid dynamics parameters. Otherwise, the bubble-cloud-wake system outlet molar flow rate for each chemical species is then calculated.

$$\text{if } z < H_{max}: T_z = T_{z+\Delta z}, P_z = P_{z+\Delta z} \quad (4.104)$$

$$\text{otherwise: } F_{bcw}(i) = F_b(i) + F_c(i) + F_w(i) \quad (4.105)$$

The flow rate $F_{bcw}(i)$ is set to be the bubble-cloud-wake model output.

4.6.5 - Emulsion Model

The emulsion model consists of the same equations of the cloud stage of the bubble-cloud-wake model.

$$F_{E_{z+\Delta z}}(i) = F_{E_z}(i) - F_d(i) + F_{cd}(i) \quad (4.46)$$

As done before, diffused and counter-diffused molar flow rate are calculated following procedures at appendices A and B respectively.

Initialization depends on the path the algorithm chooses. For path one, at $z = 0$, values for F_E are calculated from the flow rate splitting.

$$q_E = U_e A_{cs} (1 - \delta) \quad (4.106)$$

$$q_t = U_0 A_{cs} \quad (4.107)$$

$$\theta = \frac{q_E}{q_t} \quad (4.108)$$

$$F_{E_{z=0}}(i) = \theta \cdot F_0(i) \quad (4.109)$$

$$F_{E_{z+\Delta z}}(i) = F_{E_z}(i) - F_d(i) + F_{cd}(i) \quad (4.110)$$

$$z = z + \Delta z \quad (4.111)$$

$$\text{if } z < H_{max}: F_{E_z}(i) = F_{E_{z+\Delta z}}(i) \quad (4.112)$$

While condition $z < H_b$ is true, the calculation loop continues.

For path two, at $z = 0$, values for F_E are estimated and added to the gas from distributor. After the bubble-cloud-wake model is run, two-thirds of the gas returns downward in the emulsion and the model is solved upside down. The output of the emulsion model is compared to the estimated values for F_E in the convergence block. While the absolute difference between calculated and estimated F_E is not equal or lower than a tolerance of 0.00001 the calculated values substitute the estimated values and the calculations proceed to the bubble-cloud-wake model.

$$z = H_b \quad (4.113)$$

$$F_{E_{z-\Delta z}}(i) = F_{E_z}(i) - F_d(i) + F_{cd}(i) \quad (4.114)$$

$$z = z - \Delta z \quad (4.115)$$

$$\text{if } z > 0: F_{E_z}(i) = F_{E_{z-\Delta z}}(i) \quad (4.116)$$

4.6.6 - Splash Zone Model

For path one, the splash zone model consist of the summation of the bubble-cloud-wake system outlet and the emulsion outlet. Meanwhile for path two, the model consists of one stream with around forty percent the material from the bubble-cloud-wake system outlet.

$$\text{for path 1: } F_{splash}(i) = F_{bcw}(i) + F_E(i) \quad (4.117)$$

$$\text{for path 2: } F_{splash}(i) = 0.4 \cdot F_{bcw}(i) \quad (4.118)$$

4.6.7 - Freeboard Model

The freeboard model calculations begin with the following equations:

$$z = 0 \quad (4.119)$$

$$H_{free} = H - H_b \quad (4.120)$$

$$aU_0 = 0.27791664 + 0.00521358 \cdot d_p - 2.06684377 \cdot 10^{-6}(d_p)^2 \quad (4.85)$$

$$V_{\Delta z} = A_{cs}\Delta z \quad (4.78)$$

$$m_{1p} = \rho_s \cdot \frac{1}{6}\pi(\varphi_s d_p)^3 \quad (4.79)$$

$$S_{cat_{1p}} = \pi(\varphi_s d_p)^2 \quad (4.80)$$

$$F_{free_{z=0}}(i) = F_{splash}(i) \quad (4.121)$$

After these equations are solved, the height-dependent calculations begin:

$$\rho_{b_z} = \rho_b e^{-a \cdot z} \quad (4.84)$$

$$m_{s_z} = \rho_{b_z} V_{\Delta z} \quad (4.81)$$

$$Np_{fb_z} = \frac{m_{s_z}}{m_{1p}} \quad (4.82)$$

$$S_{cat_z} = Np_{fb_z} S_{cat_{1p}} \quad (4.83)$$

The value of S_{cat_z} is important for the calculation of the diffused molar flow rate of the species in the freeboard zone. The material balance at the freeboard follows the same structure for the cloud stage and emulsion model:

$$F_{free_{z+\Delta z}}(i) = F_{free_z}(i) - F_d(i) + F_{cd}(i) \quad (4.122)$$

$$z = z + \Delta z \quad (4.102)$$

$$\text{if } z < H_{free}: F_{free_z}(i) = F_{free_{z+\Delta z}}(i) \text{ and repeat calculations} \quad (4.123)$$

$$\text{Otherwise: } F_{free_{out}}(i) = F_{free_{z+\Delta z}}(i)$$

4.6.8 - Cyclones Model

The final stage of the Bubbling Fluidized Bed Reactor mathematical model is the model for cyclones. The model needs the input of the cyclone diameter and type (high or medium efficiency, and deflector position) to calculate pressure drop:

Table 4.2 – Cyclone measurements values for high and medium efficiency equipment.

Measurement	High Eff.	Medium Eff.
h	0.5 Dc	0.75 Dc
l	0.2 Dc	0.375 Dc
Dd	0.5 Dc	0.875 Dc
s	0.5 Dc	0.75 Dc
L	1.5 Dc	1.5 Dc
L'	2.5 Dc	2.5 Dc

Source: MACINTYRE (1990).³⁶

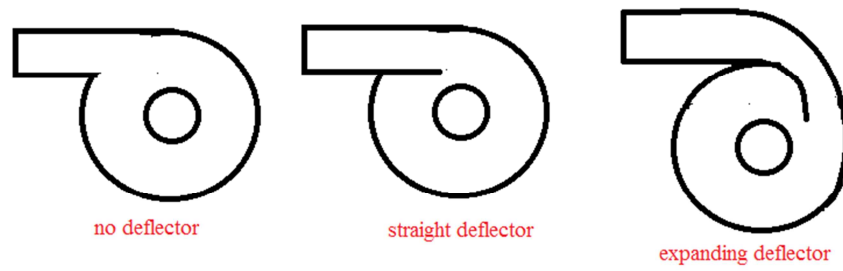
Figure 4.23 – Inlet structures of the cyclone. ³⁵

Table 4.3 – Deflector position and K value.

Position	K
No deflector	0.5
Straight	1
Expanding	2

Source: MACINTYRE (1990).³⁶

$$\Delta P(\text{inW}) = \frac{12 \cdot l \cdot h}{K \cdot D_d^2 \sqrt{\frac{L}{D_c}} \sqrt{\frac{L'}{D_c}}} \quad (4.86)$$

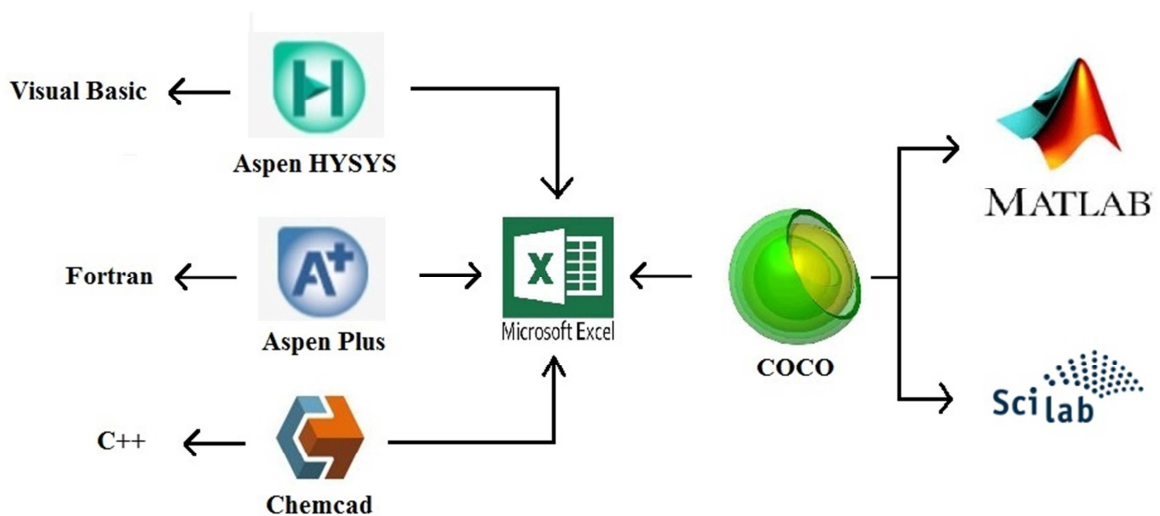
$$\Delta P(\text{kPa}) = \frac{101.3}{407.1} \cdot \Delta P(\text{inW}) \quad (4.87)$$

5 – MODEL COUPLING

The usage of commercial process simulators is limited by the license available. The School of Chemical Engineering from University of Campinas (FEQ-UNICAMP) has the license for the Aspen package, which includes Aspen Hysys™ and Aspen Plus™ simulators. The process simulator used in this thesis is the Aspen Plus™.

Commercial process simulators usually have more than one option for users to insert their own models (figure 5.1). Aspen Hysys™ (from Aspen Tech) allows Visual Basic modules, Aspen Plus™ (also from Aspen Tech) allows FORTRAN subroutines and ChemCAD™ (from Chemstations) allows C++ codes. As second option, all these cited process simulators also allow the insertion of user models written as Microsoft Excel spreadsheets. The free license process simulator COCO (Cape Open to Cape Open) also allows, as first option, Excel spreadsheets as user models.

Figure 5.1 – Process simulators options for user models languages.



There are advantages and disadvantages, for both FORTRAN subroutines and Excel spreadsheets, in the user model incorporation into Aspen Plus™ flowsheet. FORTRAN main advantage is that the code is compiled, so the subroutine is executed quickly. However, for insertion of FORTRAN code, Aspen Tech demands a specific compiler, with specific setup, and specific way to write the code. In the end, write a FORTRAN subroutine for Aspen requires more effort than usual FORTRAN programming.

On other hand, Excel spreadsheets have easy programming steps, do not require nothing else then Microsoft Excel and therefore are much more available (Microsoft Excel is a software widely available and used in industry). Other advantage is that, with the required input of thermodynamics data, it is possible to execute the user model as a stand-alone module, with no link to Aspen PlusTM. However, the stand-alone possibility brings two important pitfalls: the necessity to input thermodynamics data (which may not be simple to obtain), and the necessity to program functions to calculate thermodynamic properties (such as enthalpy, and so on). However, these pitfalls may be bypassed using CAPE-OPEN standards.

Other important disadvantage of Excel spreadsheets is that the Visual Basic for Applications (VBA), the programming language of Excel procedures, is an interpreted language (instead of the FORTRAN, which is compiled), so the execution is much slower than a FORTRAN code. Based on such advantages, it was chosen to use an Excel spreadsheet as the user model for the reactor unit.

For the Excel spreadsheet to be compatible with the Aspen PlusTM user unit operation, it must follow some guidelines, and this template, called *userxltemplate.xls*, is available in the installed directory *user*, inside the directory *engine* of the Aspen Plus files.³⁸ The template *userxltemplate.xls* consists of sheets with data in the structure used by Aspen Plus. The procedure consists in the following steps:

1. Copy the Excel template to the working directory. The file must be renamed for convenience.
2. The Aspen PlusTM interface must be started up. The components must be chosen (figure 5.2) and an adequate thermodynamic package must also be chosen (figure 5.3). Then, place a user2 block (the user unit operation block in the Aspen PlusTM features) and connect the inlet and outlet streams with the whole flowsheet (figure 5.4).

Figure 5.2 – Chemical species selection.

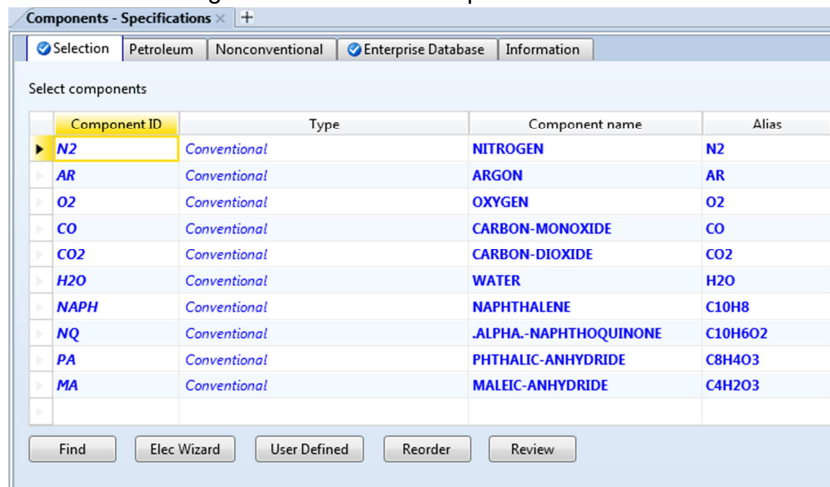


Figure 5.3 – Thermodynamics package selection.

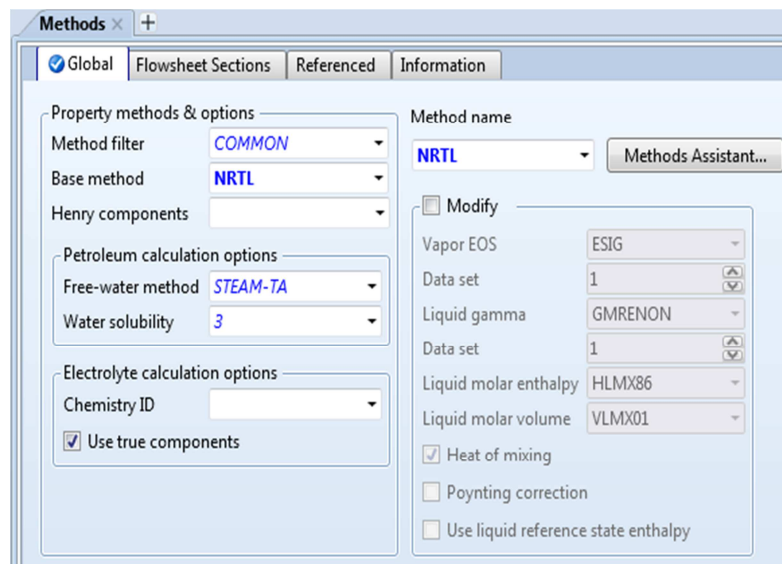
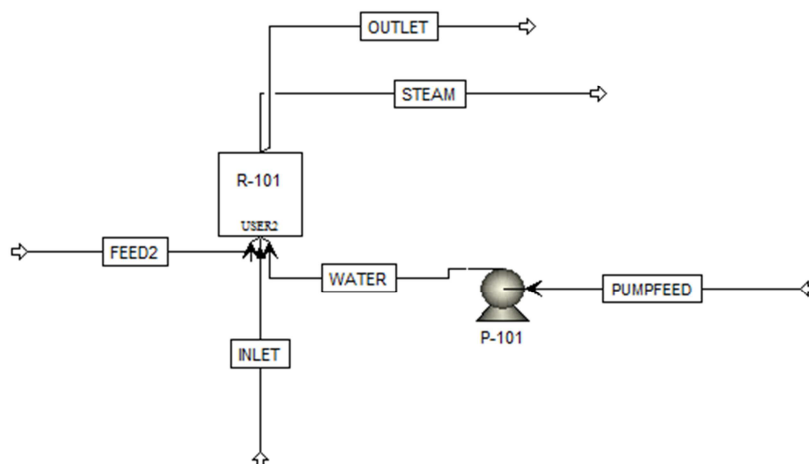
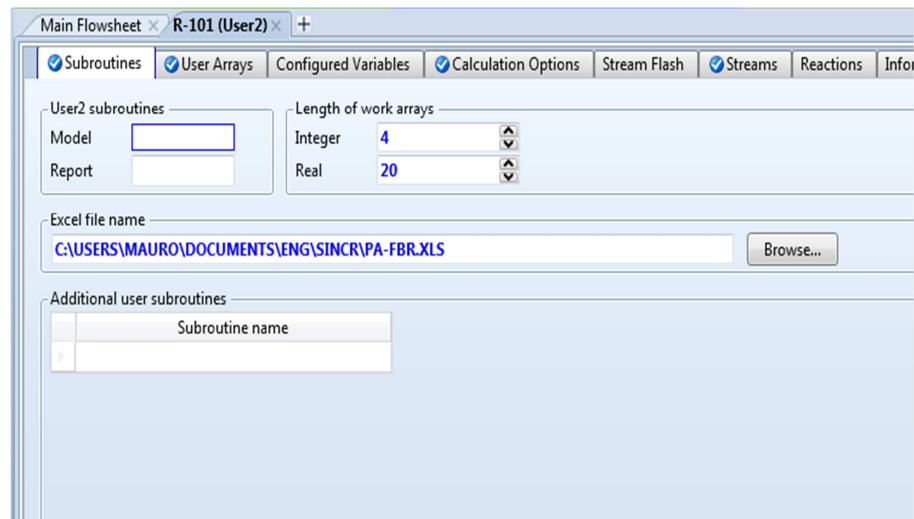


Figure 5.4 – Flowsheet with user module inserted.



- The inlet streams must be specified with composition, temperature and pressure. The user block must be specified with the path for the Excel template (figure 5.5), as with the numbers of integer and decimal parameters (in the Aspen Plus vocabulary, decimals are called *real*, because it is based on Fortran programming language).

Figure 5.5 – Excel template path specification.



- Run the simulation to build the tables into the Excel spreadsheet. By running the simulation, the spreadsheet is filled with data at specific zones, from which it is possible to load them to the VBA code.
- Bring up the spreadsheet and insert the VBA code in the Visual Basic Editor. Retrieve input data from the *Aspen_Input* sheet (for the inlet streams data), and from the *Aspen_IntParams* and *Aspen_RealParams* sheets (for the integer and decimal parameters). Store the results in the *Aspen_Output* sheet. The Excel template has a module, called *AspenHooks*, with pre-programmed functions and subroutines. The function *ahGetValue* is used to retrieve data from the sheets, and the subroutine *ahSetValue* is used to store data into the sheets. More info about how to deal with these procedures is available in the *AspenHooks* module as comments.

Figure 5.6 – VBA code programming.

```

Microsoft Visual Basic for Applications - PA-FBR.xls - [Módulo1 (Código)]
Arquivo  Editar  Exibir  Inserir  Formatar  Depurar  Ejecutar  Herramientas  Suplementos  Janela  Ayuda

Proyecto - VBAProject
Microsoft Excel Objeto
Plan1 (Aspen_O)
Sheet1 (Aspen_)
Sheet2 (Aspen_)
Sheet3 (Aspen_)
Sheet4 (Sheet1)
Sheet5 (Sheet2)
Sheet6 (Sheet3)
Sheet8 (Aspen_)
ThisWorkbook
Módulos

Propiedades
Alfabético  Categorizado

'input
Ncomp = ahGetValue([Aspen_IntParams], 1, 1)
Nrxn = ahGetValue([Aspen_IntParams], 2, 1)
Ncr = ahGetValue([Aspen_IntParams], 3, 1)
Nt = ahGetValue([Aspen_IntParams], 4, 1)

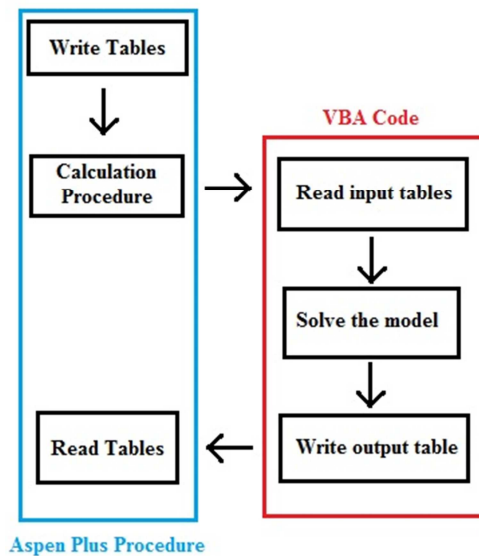
dp = ahGetValue([Aspen_RealParams], 1, 1)
rho_s = ahGetValue([Aspen_RealParams], 2, 1)
phi = ahGetValue([Aspen_RealParams], 3, 1)
Umf = ahGetValue([Aspen_RealParams], 4, 1)
ks = ahGetValue([Aspen_RealParams], 5, 1)
Cps = ahGetValue([Aspen_RealParams], 6, 1)
d = ahGetValue([Aspen_RealParams], 7, 1)
Hmax = ahGetValue([Aspen_RealParams], 8, 1)
dcr = ahGetValue([Aspen_RealParams], 9, 1)
z0 = ahGetValue([Aspen_RealParams], 10, 1)
Dc = ahGetValue([Aspen_RealParams], 11, 1)
dT = ahGetValue([Aspen_RealParams], 12, 1)
dtin = ahGetValue([Aspen_RealParams], 13, 1)
Lc = ahGetValue([Aspen_RealParams], 14, 1)
UO = ahGetValue([Aspen_RealParams], 15, 1)
rho = ahGetValue([Aspen_RealParams], 16, 1)
visc = ahGetValue([Aspen_RealParams], 17, 1)
diff = ahGetValue([Aspen_RealParams], 18, 1)
Kg = ahGetValue([Aspen_RealParams], 19, 1)
Toper = ahGetValue([Aspen_RealParams], 20, 1)

For i = 1 To Ncomp Step 1
  Fin(i) = ahGetValue([Aspen_Input], i, 2)
  FinA(i) = ahGetValue([Aspen_Input], i, 1)
Next i
FTin = ahGetValue([Aspen_Input], Ncomp + 1, 2)
FTinA = ahGetValue([Aspen_Input], Ncomp + 1, 1)
Tin = ahGetValue([Aspen_Input], Ncomp + 2, 2)
TinA = ahGetValue([Aspen_Input], Ncomp + 2, 1)
Fin = ahGetValue([Aspen_Input], Ncomp + 3, 2)

```

6. When Aspen Plus™ runs the Excel spreadsheet from within the flowsheet, the input data is written into the file and a function from AspenHooks module is called to solve the model, the *AspenCalculate* function. It is necessary to edit this function inside the AspenHooks module, inserting a statement to call the subroutine which solves the models (the one programmed by the user).

Figure 5.7 – Aspen Plus™ procedure to execute user model Excel spreadsheet.



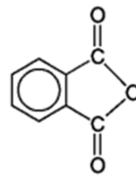
With the subroutines programmed, it is now possible to run the Excel file from within the Aspen Plus™ Flowsheet.

6 – CASE STUDY

6.1 – Phthalic anhydride

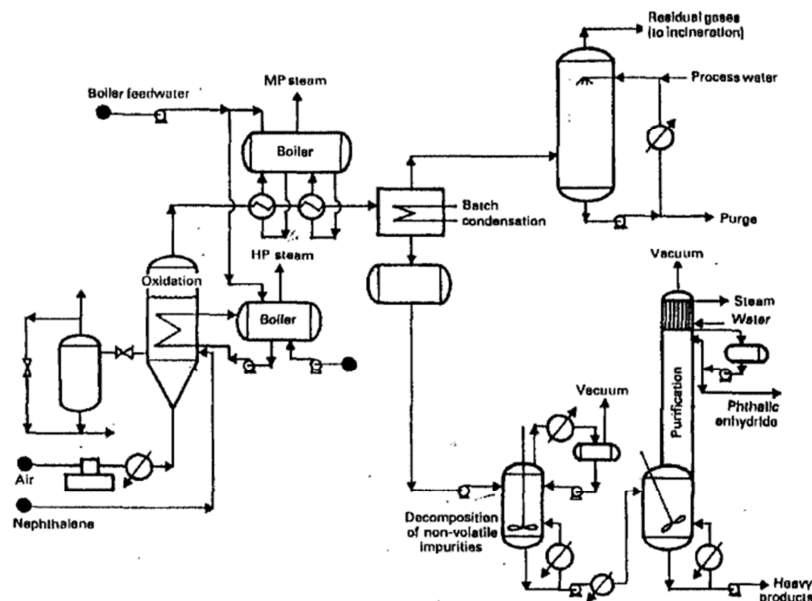
Phthalic anhydride (figure 6.1), is a chemical substance that may be derived from the naphthalene or from o-xylene, and is an important commodity used for alkyd resins, unsaturated polyester resins and plasticizers.³⁹ In 1993, the worldwide production of phthalic anhydride was circa 3.5 millions of metric tons.⁴⁰

Figure 6.1 – Molecular structure of the phthalic anhydride.



Either via o-xylene or naphthalene, the chemical reactions are highly exothermic and can be operated in fixed bed multi-tubular reactor, with 5000 to 20000 tubes, or in fluidized bed reactor, cooled by internal coils to produce high pressure steam. In both reactors, the catalyst consists of supported vanadium pentoxide and titanium dioxide. The commercial process Sherwin-Williams/Badger (figure 6.2) uses a fluidized bed reactor for the production of phthalic anhydride.³⁹

Figure 6.2 – Process Flow Diagram for the Sherwin-Williams / Badger Process.



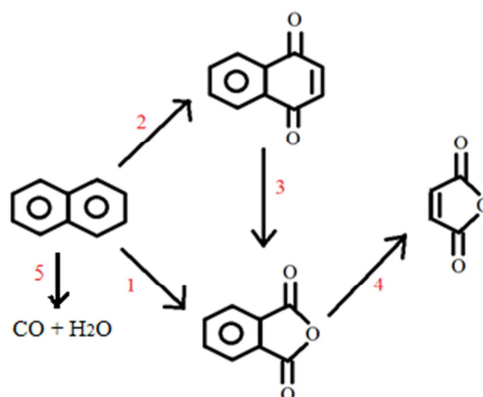
Source: Chauvel and Lefevbre (1989).³⁹

This process uses naphthalene as raw material, which is injected as liquid in the base of the fluidized bed reactor, where the vanadium pentoxide and titanium dioxide catalyst is fluidized by air. Liquid naphthalene is immediately vaporized and dispersed in the bed, and oxidizes in the uniform temperature ranging between 340°C and 385°C. The mixture containing phthalic anhydride is then condensed and sent to a heat treatment under vacuum to decompose impurities with can dye the final product, while the gas stream is scrubbed and then sent to incineration.³⁹

6.1.1 – Chemical Reactions

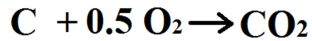
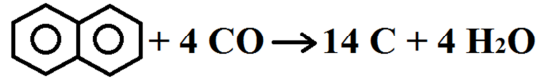
DEMARIA, LONGFIELD and BUTLER (1961)⁴¹, performed a kinetics study of the naphthalene over vanadium oxides catalyst and concluded that there are four main reactions in the process (figure 6.3): 1 - the naphthalene oxidation to phthalic anhydride, 2 - naphthalene oxidation to naphthoquinone, 3 - the naphthoquinone oxidation to phthalic anhydride and 4 - the phthalic anhydride oxidation to maleic anhydride (figure 6.3). In means of kinetics, reaction 5 (naphthalene decomposition) is not important, however, its contribution to the formation of carbon monoxide is significant, and it is considered in this work.

Figure 6.3 – Simplified reactions network of the naphthalene oxidation.



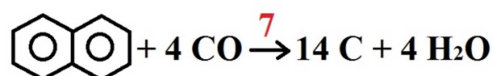
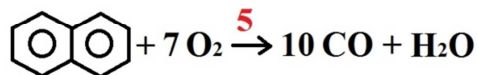
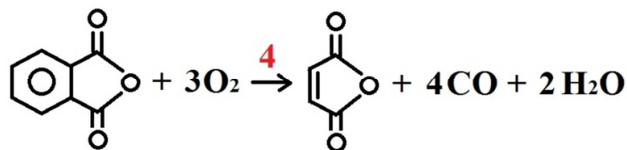
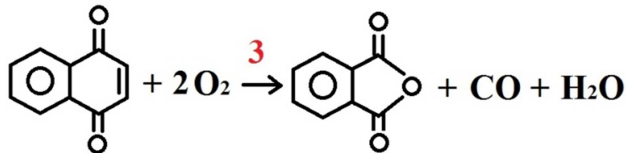
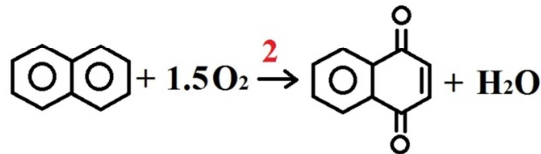
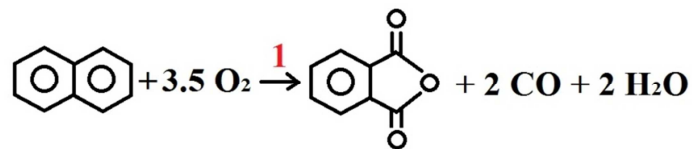
A common way of catalytic deactivation for hydrocarbon chemical reactions under high temperatures is the coke deposition (figure 6.4). Although previous works do not present any studies about coke formation for naphthalene oxidation, it is reasonable to consider it as part of the reactions set.

Figure 6.4 – Reactions of coke formation and consumption.



Coke formation may occur from carbon monoxide dimerization and from naphthalene reduction with carbon monoxide. Then, coke reacts with oxygen gas to form carbon dioxide.

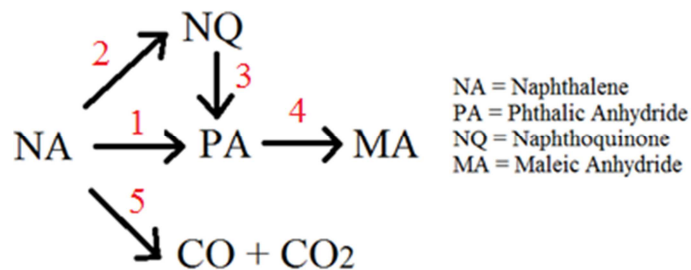
Figure 6.5 – More detailed reactions network of the naphthalene oxidation.



6.1.2 – Chemical Kinetics

One of the first kinetic studies regarding naphthalene oxidation was published in 1956 by D'ALESSANDRO and FARKAS.⁴² They analyzed the chemical reactions over vanadium pentoxide catalyst in packed bed and fluidized bed reactors of bench scale. After analysis over obtained data, they concluded the chemical reactions are connected through the following network, expressed in figure 6.6.

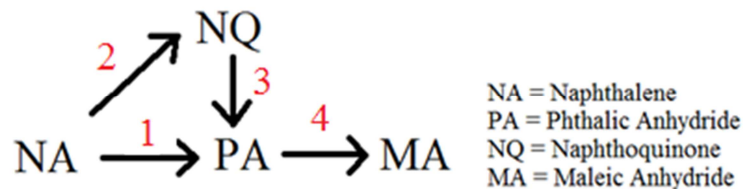
Figure 6.6 – Reactions network as described by D'ALESSANDRO and FARKAS (1956)⁴².



This chemical reaction network was later confirmed in 1961 by DeMaria, Longfield and Butler⁴¹. However, the latter work pointed that the direct oxidation of naphthalene to CO and CO₂ as low reaction rate. Their paper also performed regression of data obtained in a fluidized bed reactor of bench scale, with two different catalysts, in order to fit a pseudo-first order model for the reactions.

In 1962, PETERSON⁴³, performed a non-linear estimation for a pseudo-first order kinetic model considering the main four reactions of the network proposed before (figure 6.7).

Figure 6.7 – Reactions network used on the estimation by PETERSON (1962)⁴³.



$$r_1 = k_1 C_{NA} \quad (6.1)$$

$$r_2 = k_2 C_{NA} \quad (6.2)$$

$$r_3 = k_3 C_{NQ} \quad (6.3)$$

$$r_4 = k_4 C_{PA} \quad (6.4)$$

The Arrhenius equation ⁴⁴ was used to describe the pseudo-first order rate constants in equation (6.1) to (6.4).

$$k = k_0 e^{-\frac{E_a}{R} \left(\frac{1}{T} - \frac{1}{T_0} \right)} \quad (6.5)$$

In equation (6.5), k_0 is the pre-exponential factor (s^{-1}), $\frac{E_a}{R}$ is the ratio of activation energy per ideal gas constant (K), and T_0 is the reference temperature of the kinetics data, which is 597.371 K. Values of the pre-exponential factors and ratio of activation energy per ideal gas constant for each reaction considered are described in the table (6.1).

Table 6.1 – Kinetics data obtained by PETERSON (1962) ⁴³.

Reaction	k_0 (s^{-1})	$\frac{E_a}{R}$ (K)
1	4.03	8.41
2	3.15	6.34
3	3.51	4.01
4	0.014	22.7

In 1969, Carberry and White ⁴⁵, provided the activation energy for the chemical reactions network described by DEMARIA, LONGFIELD and BUTLER (1961) ⁴¹, and this allowed to perform a non-linear regression to fit the data to a modified Arrhenius model (equation (6.6))⁴⁶. Such statistical regression is described by MONTGOMERY and RUNGER (1999) ³³, WALPOLE et al. (2007) ⁴⁷ and ROSS (2004) ⁴⁸.

$$k = k_0 T^n e^{-\frac{E_a}{RT}} \quad (6.6)$$

Table 6.2 – Pseudo-first order constants for 320°C and 370°C and activation energy for reactions for both catalysts.

Reaction	Catalyst A		Catalyst B	
	k (s^{-1})	E_a (kcal kmol ⁻¹)	k (s^{-1})	E_a (kcal kmol ⁻¹)
1(at 320°C)	0.25	38	0.11	20
1(at 370°C)	3.5	38	0.42	20
2(at 320°C)	0.25	38	0.11	20
2(at 370°C)	3.5	38	0.42	20
3(at 320°C)	0.4	50	0.45	12
3(at 370°C)	12	50	1	12
4(at 320°C)	0.0095	20	0.0016	43
4(at 370°C)	0.035	20	0.03	43

Table 6.3 – Kinetic data obtained by non-linear regression of data from CARBERRY and WHITE (1969) ⁴⁵.

Reactions	$k_0(\text{s}^{-1})$	n	$\frac{E_a}{R}$ (K)
1	$7.174 \cdot 10^8$	1.638573	19123.4063
2	$7.174 \cdot 10^8$	1.638573	19123.4063
3	$3.209 \cdot 10^{14}$	1.269029	25162.37671
4	$4.35 \cdot 10^7$	-0.818279	10064.95069

In 1989, DUTTA and SUCIU ⁴⁹, performed simulations of a reactor running the naphthalene oxidation and provided the following kinetics models considering the reactions network described by PETERSON (1962) ⁴³:

$$r_1 = k_1 C_{NA} C_O \quad (6.7)$$

$$r_2 = k_2 C_{NA} C_O \quad (6.8)$$

$$r_3 = k_3 C_{NQ} \quad (6.9)$$

$$r_4 = k_4 C_{PA} C_O^{0.8} \quad (6.10)$$

$$k = k_0 e^{-\frac{E_a}{RT}} \quad (6.11)$$

In equation (6.7) to (6.10), the indexes NA, NQ, PA and O represent naphthalene, naphthoquinone, phthalic anhydride and oxygen respectively.

Table 6.4 – Kinetics data described by Dutta and Suciú (1989) ⁴⁹.

Reaction	k_0	E_a (kJ mol ⁻¹)
1	$1.7 \cdot 10^9$	84
2	$1.7 \cdot 10^9$	84
3	$3.4 \cdot 10^7$	84
4	$8.4 \cdot 10^6$	84

Although, DUTTA and SUCIU (1989) ⁴⁹ declare in their paper that due to the lack of kinetics data on the literature they assumed the value of the activation energy the same for all four reactions and equal to 84 kJ mol⁻¹ as a reasonable value.

The kinetic model described by DEMARIA, LONGFIELD and BUTLER (1961) ⁴¹ was the base for the data shown by CARBERRY and WHITE (1969) ⁴⁵, which was the base for the regression performed for this work. However, such kinetics model was based only on the four main reactions, the same described by PETERSON (1962) ⁴³, and was developed under the hypothesis that the oxygen content is kept constant along the fluidized bed height. This hypothesis does not match the reality, as described in paper by the authors ⁴¹. The model also considers the gas flow as ideal.

Then, a kinetic model which was developed under non-realistic hypothesis and ideal gas flow must not be expected to describe accurately a system modelled under

non-ideal gas flow (the fluidized bed reactor for the phthalic anhydride production). Therefore, the kinetics model obtained by regression must be only an initial estimation to a more realistic kinetic model, which is obtained as a calibration of the reactor developed model with experimental inlet and outlet data of the industrial scale reactor.

6.1.3 – Case Thermodynamics

Heat transfer calculations are performed with aid of a dimensionless parameter called *Prandtl number*, which is dependent on a thermodynamic property called *heat capacity*. Molar heat capacity is calculated by means of equations of state, and in the case of ideal gas behavior, it is calculated by empirical equations.

However, as the reactor operates under relative high temperature and pressure around 2 atm, the ideal gas behavior is feasible. Ideal gas heat capacity model, equation 6.12, was taken from Aspen Tech Manual⁵⁰ and coefficients were taken from Aspen PlusTM database:

$$C_p(i) = C_{1i} + C_{2i} \left(\frac{C_{3i}/T}{\text{Sinh}\left(\frac{C_{3i}}{T}\right)} \right)^2 + C_{4i} \left(\frac{C_{5i}/T}{\text{Cosh}\left(\frac{C_{5i}}{T}\right)} \right)^2 \quad (6.12)$$

Nevertheless, for the purpose of simplicity to perform the algebraic integration of the heat capacity, all data was fit to a fourth degree polynomial equation by multiple linear regression³³:

$$C_p(i) = A_{0i} + A_{1i}T + A_{2i}T^2 + A_{3i}T^3 + A_{4i}T^4 \quad (6.13)$$

In equation (6.13), $C_p(i)$ represents the molar heat capacity of the i -th substance ($\text{kJ kmol}^{-1} \text{K}^{-1}$), and T represents the temperature ($^{\circ}\text{C}$). The coefficients for the equation (6.13) are found in the table (6.5):

Table 6.5 – Coefficients for heat capacity equation.

Substance	A_{0i}	A_{1i}	A_{2i}	A_{3i}	A_{4i}
N₂	29.172	-0.0017	$2 \cdot 10^{-5}$	$2 \cdot 10^{-8}$	$5 \cdot 10^{-12}$
Ar	20.786	0	0	0	0
O₂	29.147	0.0059	$2 \cdot 10^{-5}$	$-3 \cdot 10^{-8}$	$1 \cdot 10^{-11}$
CO	29.161	-0.0012	$2 \cdot 10^{-5}$	$-3 \cdot 10^{-8}$	$9 \cdot 10^{-12}$
CO₂	36.118	0.0504	$-7 \cdot 10^{-5}$	$6 \cdot 10^{-8}$	$-3 \cdot 10^{-11}$
H₂O	33.413	0.0051	$2 \cdot 10^{-5}$	$-1 \cdot 10^{-8}$	$5 \cdot 10^{-12}$
NA	115.67	0.5821	-0.0006	$4 \cdot 10^{-7}$	$-1 \cdot 10^{-10}$
PA	98.474	0.3283	0.0001	$-7 \cdot 10^{-7}$	$5 \cdot 10^{-10}$

MA	104.81	0.3289	-0.0007	$9 \cdot 10^{-7}$	$-5 \cdot 10^{-10}$
NQ	142.71	0.5428	-0.0006	$3 \cdot 10^{-7}$	$-9 \cdot 10^{-11}$

$$\int_{T_{ref}}^T C_p(i) dT = A_{0i}(T - T_{ref}) + \frac{A_{1i}}{2}(T^2 - T_{ref}^2) + \frac{A_{2i}}{3}(T^3 - T_{ref}^3) + \frac{A_{3i}}{4}(T^4 - T_{ref}^4) + \frac{A_{4i}}{5}(T^5 - T_{ref}^5) \quad (6.14)$$

The ideal gas enthalpy is calculated by the equation (6.14).

The chemical reactions involved in the naphthalene oxidation are highly exothermic. Standard heats of formation of each substance are found in table (6.6).

Table 6.6 – Standard heat of formation of the substances.

Substance	ΔH_f^0 (J kmol ⁻¹) x 10 ⁻⁷
N₂	0
Ar	0
O₂	0
CO	-11.053
CO₂	-39.351
H₂O	-24.1814
NA	15.058
PA	-29.765 *
MA	-53.829 *
NQ	-9.75

Source: All taken from NIST database except the ones marked *, which were calculated by Joback method described by PERRY (1999) ⁵¹.

Based on the standard heats of formation of the substances and the stoichiometry of the network reactions, the standard heats of reactions are calculated by the difference between the standard heats of formation of the products and reactants for each reaction, and are shown at the table (6.7).

The naphthalene oxidation to phthalic anhydride releases $115.2918 \cdot 10^4$ kJ kmol⁻¹, the naphthalene oxidation to naphthoquinone releases $48.9894 \cdot 10^4$ kJ kmol⁻¹, the naphthoquinone oxidation to phthalic anhydride releases $66.3024 \cdot 10^4$ kJ kmol⁻¹ and the phthalic anhydride oxidation to maleic anhydride releases $115.6388 \cdot 10^4$ kJ kmol⁻¹. The naphthalene oxidation to carbon monoxide releases $222.314 \cdot 10^4$ kJ kmol⁻¹. Carbon monoxide dimerization releases $17.245 \cdot 10^4$ kJ kmol⁻¹. Naphthalene reduction with carbon monoxide releases $67.5716 \cdot 10^4$ kJ kmol⁻¹, and the coke combustion releases $39.351 \cdot 10^4$ kJ kmol⁻¹.

Table 6.7 – Standard heats of reactions.

Reaction	$\Delta H_f(\text{kJ kmol}^{-1}) \times 10^{-4}$
1	-115.2918
2	-48.9894
3	-66.3024
4	-115.6388
5	-222.3136
6	-17.2450
7	-67.5716
8	-39.3510

As the chemical reactions do not occur at 25°C and 1 atm, it is required to calculate the energy necessary to bring the reactants of each reaction from the solid temperature to the standard condition, and the energy necessary to take the products of each reaction to the catalyst condition. This task is performed by the integration of the molar heat capacity variation:

$$\Delta C_p(i) = \Delta A_{0i} + \Delta A_{1i}T + \Delta A_{2i}T^2 + \Delta A_{3i}T^3 + \Delta A_{4i}T^4 \quad (6.15)$$

$$\int_{T_{ref}}^{T_s} \Delta C_p(i)dT = \Delta A_{0i}(T_s - T_{ref}) + \frac{\Delta A_{1i}}{2}(T_s^2 - T_{ref}^2) + \frac{\Delta A_{2i}}{3}(T_s^3 - T_{ref}^3) + \frac{\Delta A_{3i}}{4}(T_s^4 - T_{ref}^4) + \frac{\Delta A_{4i}}{5}(T_s^5 - T_{ref}^5) \quad (6.16)$$

Therefore, the heat of reaction is calculated by the sum of the standard heat of reaction and the enthalpy change of the substances:

$$\Delta H_{rxn}(j) = \Delta H_f^0(j) + \int_{T_{ref}}^{T_s} \Delta C_p(i,j)dT \quad (6.17)$$

In equation (6.17) j represents the chemical reaction identification.

6.1.4 – Reactor Geometry

In previous works, JOHNSON, GRACE and GRAHAM (1987)⁵², published a comparison of fluidized bed reactor models with experimental data of inlet and outlet of an industrial scale reactor. The reactor in the paper is a bubbling fluidized bed of 2.13 m diameter, 13.7 m height (7.9 m of expanded bed height), ca. 9% of the bed cross-section occupied by vertical tubes of 7 m depth and distributor of perforated plate with 56 orifices.

The FBR of such reference operated at gas velocity of 0.43 m s^{-1} , and the bed temperature was kept at 636 K ($363 \text{ }^\circ\text{C}$). Catalyst particles had mean diameter of 53 micra , solid density of 1200 kg m^{-3} , unity sphericity, thermal conductivity of $18 \text{ W m}^{-1} \text{ K}^{-1}$, heat capacity of $880 \text{ J kg}^{-1} \text{ K}^{-1}$, and minimum fluidization velocity of $7.7 \cdot 10^{-4} \text{ m s}^{-1}$.

Table 6.8 – Geometry parameters of the reactor.

Parameter	Value
Height	13.7 m
Diameter	2.13 m
Expanded bed height	7.9 m
Number of orifices	52
Diameter of orifices	11.1 mm
Number of tubes	135
Inner tube diameter	45 mm
Outer tube diameter	55 mm
Height of tubes	7 m

Source: JOHNSON, GRACE and GRAHAM (1987).⁵²

Table 6.9 – Operating conditions of the reactor.

Parameter	Value
Gas velocity	0.43 m s^{-1}
Operation temperature	636 K

Source: JOHNSON, GRACE and GRAHAM (1987).⁵²

Air used for the fluidization was 1.56 kg m^{-3} of density, viscosity of $3.2 \cdot 10^{-5} \text{ Pascal seconds}$, Diffusivity of $2.65 \cdot 10^{-6} \text{ m}^2 \text{ s}^{-1}$ and thermal conductivity of $0.1052 \text{ W m}^{-1} \text{ K}^{-1}$.

Table 6.10 – Particle parameters of the reactor.

Parameter	Value
Mean diameter	$53 \text{ }\mu\text{m}$
Solid density	1200 kg m^{-3}
Sphericity	1
Thermal conductivity	$18 \text{ W m}^{-1} \text{ K}^{-1}$
Heat capacity	$880 \text{ J kg}^{-1} \text{ K}^{-1}$
Minimum fluidization velocity	$7.7 \cdot 10^{-4} \text{ m s}^{-1}$

Source: JOHNSON, GRACE and GRAHAM (1987).⁵²

Table 6.11 – Air parameters of the reactor.

Parameter	Value
Gas density	1.56 kg m^{-3}
Gas viscosity	$3.2 \cdot 10^{-5} \text{ Pa s}$
Diffusivity	$1.06 \cdot 10^{-4} \text{ m}^2 \text{ s}^{-1}$
Thermal conductivity	$0.1052 \text{ W m}^{-1} \text{ K}^{-1}$

Source: JOHNSON, GRACE and GRAHAM (1987).⁵²

7 - RESULTS AND DISCUSSION

7.1 – Model Calibration

For the model calibration, the Excel spreadsheet was run offline, which means, uncoupled with the Aspen PlusTM Flowsheet. The purpose of the calibration is the fit of the kinetic parameters to experimental data.

7.1.1 – Input-Output data fit

As explained in section 6.1.2, all kinetics models available today were obtained under unrealistic hypothesis and ideal flow pattern, so such models are not expected to describe accurately a reactor with non-ideal flow pattern for fluidization. Furthermore, this thesis considers the reactions network a set of 8 reactions and not 4 reactions as the previous models.

Mathematical models may be classified by several ways, and one of them is to separate models into two general classes: phenomenological models (which are based on physical theory) and empirical models (so called black-box). Both for physical and for black-box models, input-output data are necessary to fit unknown coefficients.⁵³

Then, it is necessary to perform at least one experiment in the modeled reactor to calibrate the model. In other words, at least one experiment is necessary to fit kinetics parameters in order to match the model output to the reactor outlet, so the model may be used in other operation conditions with a certain degree of confidence. However, in academic research sometimes it is not possible to perform experiments and experimental data from literature are necessary for such task. The main drawback is that such experimental inlet-outlet data for industrial chemical reactors are rare in academic literature.

Although the difficulties to find experimental inlet-outlet data for industrial reactors, the paper by JOHANSSON, GRACE and GRAHAM (1987)⁵² has such data and this was the reason the phthalic anhydride BFB reactor was chosen as the case study.

Table 7.1 – Reactor experimental data.

Substance	Flow (kmol h ⁻¹)	
	In	Out
N₂	192.3	192.3
Ar	2.2	2.2
O₂	51.7	25.5
CO	0	2.95
CO₂	0	11.58
H₂O	3.2	14.94
NA	5.29	<0.1
NQ	0	0.068
PA	0	4.64
MA	0	0.168

Source: JOHANSSON, GRACE and GRAHAM (1987)⁵².

In the industrial practice, simple mathematical models are usually used to fit experimental data. Therefore, for the calibration, a pseudo-first order power law kinetic model was assumed for each chemical reaction, and the rate constant was assumed as following a modified Arrhenius equation.

$$r_1 = k_1 F_{d,NA} \left(\frac{V_{cat}}{Q_t} \right) \quad (6.1)$$

$$r_2 = k_2 F_{d,NA} \left(\frac{V_{cat}}{Q_t} \right) \quad (6.2)$$

$$r_3 = k_3 F_{NQ,f} \left(\frac{V_{cat}}{Q_t} \right) \quad (6.3)$$

$$r_4 = k_4 F_{PA,f} \left(\frac{V_{cat}}{Q_t} \right) \quad (6.4)$$

$$r_5 = k_5 F_{d,NA} \left(\frac{V_{cat}}{Q_t} \right) \quad (6.5)$$

$$r_6 = k_6 F_{CO,f} \left(\frac{V_{cat}}{Q_t} \right) \quad (6.6)$$

$$r_7 = k_7 F_{CO,f} \left(\frac{V_{cat}}{Q_t} \right) \quad (6.7)$$

$$r_8 = k_8 F_{Coke} \left(\frac{V_{cat}}{Q_t} \right) \quad (6.8)$$

In equations (6.1) and (6.8), $F_{d,NA}$ represents the diffused molar flow rate of naphthalene. In equation (6.3), $F_{NQ,f}$ represents the molar flow rate of formed naphthoquinone. In equation (6.4), $F_{PA,f}$ is the molar flow rate of formed phthalic anhydride. In equations (6.6) and (6.6), $F_{CO,f}$ represents the molar flow rate of formed carbon monoxide, and in equation (6.8), F_{Coke} represents the molar flow rate of coke formed on the catalyst surface. All molar flow rates are in expressed in kmol s⁻¹.

$$F_{NQ,f} = r_2 \quad (6.9)$$

$$F_{PA,f} = r_1 + r_3 \quad (6.10)$$

$$F_{CO,f} = 2r_1 + 2r_3 + 4r_4 + 10r_5 \quad (6.11)$$

$$F_{Coke} = 0.5 \cdot r_6 + \frac{14}{4} \cdot r_7 \quad (6.12)$$

For reactions 1 to 4, the values of the pre-exponential factors and activation energies obtained by the previous fit were accepted as constant. Moreover, only the temperature exponents for the modified Arrhenius model were varied to fit the reactor experimental data.

For reaction 5, the values of $1.2 \cdot 10^8 \text{ s}^{-1}$ and $1.5 \cdot 10^5 \text{ J mol}^{-1}$ were assumed for the pre-exponential factor and activation energy. For reactions 6 and 7, the pre-exponential factors were assumed as $1 \cdot 10^8 \text{ s}^{-1}$, and for reaction 8, $1.3 \cdot 10^6 \text{ s}^{-1}$. Activation energy for reactions 6,7 and 8 were assumed as assumed as 75284 J mol^{-1} , 86258 J mol^{-1} and 57845 J mol^{-1} . All such values were assumed based on kinetics of similar reactions. An optimization procedure by random search was performed to the fit the parameters. Results are in tables (7.2) and (7.3).

Table 7.2 – Optimized parameters for modified Arrhenius model.

Reaction	Temperature exponent (-)
1	1.84817
2	1.19
3	0
4	-0.2937
5	1.4
6	-0.2037
7	-0.2632
8	-0.0003

Table 7.3 – Comparison between model and experimental output.

Substance	Output flow (kmol h^{-1})	
	Experimental	Model
N₂	192.3	192.3
Ar	2.2	2.2
O₂	25.5	25.50935
CO	2.95	2.95029
CO₂	11.58	11.56482
H₂O	14.94	14.94026
NA	<0.1	1.08E-01
PA	0.068	0.06804
MA	4.64	4.64031
NQ	0.168	0.16810

The parameters obtained in this fit are, from now on, the kinetic model used in this work.

7.1.2 – Internal Distributions

Before coupling of the spreadsheet in Aspen Plus™, other simulation was performed with the recent operation conditions and the just fitted kinetic parameters in order to analyze whether the internal distributions of the calculated model makes physical sense.

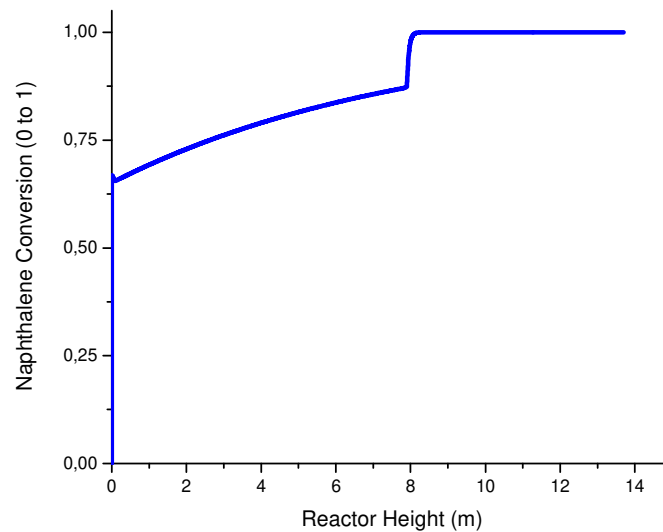
As black-box models are empirical equations with unknown parameters fit to input-output data, such equations are not attached to physical modeling. Therefore, the distributed behavior of the variables into the modeled device may not have real world correspondence. However, for physical models it is not true.

As phenomenological models are based on physical theory, internal distributions (pressure, temperature, molar flow distributions and so on) must present physically consistent behavior. Otherwise, it has no higher advantage over a black-box model.

However, it is important to warn that internal distributions of physical models must not be considered to be the real behavior of the reactive system inside the reactor. This consideration must be done due to the lack of data collection along the reactor height or length, so such distributions cannot be validated even though they present consistent behavior.

Results from the simulation show that at the reactants inlet and at the freeboard the chemical reactions occur with much more intensity than at the bubbling bed. Although the internal distribution of conversion may not be validated due to the lack of experimental data from the industrial reactor, such behavior is expected for such reactors, as described by HO (2003)¹². At the distributor exit the mass transfer is much more intense than in the bed, and at the freeboard the gas-particle contact is much more efficient.

Figure 7.1 – Naphthalene conversion versus reactor height.



As such result is similar to the expected one, it is reasonable to assume the model as physically reliable.

7.2 – Simulations after Coupling in Aspen Plus™

Once the model in the Excel spreadsheet was calibrated and present physical consistency, it was in coupled in Aspen Plus™ following the procedure explained in chapter 5. Later, simulations were performed according to a planning.

7.2.1 – Simulations Planning

For simulations after incorporation, the operating temperature of the bed T_{oper} and the superficial velocity of gas U_0 were the variables chosen to be changed. The industrial reactors operate at a range of bed temperature from 340°C to 385°C, and at a range of gas superficial velocity of the inlet air stream from 0.3 m s⁻¹ to 0.6 m s⁻¹.

The gas superficial velocity is associated with a volume flow rate, which is associated to a mass flow rate. The range from 0.3 m s⁻¹ to 0.6 m s⁻¹ is equivalent to a mass flow rate range of 9347.4 kg h⁻¹ to 18694.8 kg h⁻¹. These ranges of temperature and mass flow rate were divided in ten subdivisions, with temperature increment of 5°C and 1038.6 kg h⁻¹, resulting in a total of one hundred combinations of bed temperature and mass flow rate. As seen in table (7.4).

Table 7.4 – Values of bed temperature, gas superficial velocity and mass flow rate.

Temperature (°C)	Gas Superficial Velocity (m s ⁻¹)	Mass flow rate (kg h ⁻¹)
340	0.3	9347.4
345	0.333	10386
350	0.366	11424.6
355	0.4	12463.2
360	0.432	13501.8
365	0.465	14540.4
370	0.498	15579
375	0.531	16617.6
380	0.564	17656.2
385	0.6	18694.8

These combinations were simulated one-by-one and the molar flow rates of phthalic anhydride, maleic anhydride, naphthoquinone, naphthalene, carbon monoxide and carbon dioxide at the outlet gas stream were recorded, resulting in six different table. From these tables, important results were obtained.

7.2.2 – Final Results

For simulations after incorporation in Aspen Plus™, results obtained were: molar flow rates of phthalic anhydride, maleic anhydride and naphthoquinone, naphthalene conversion, selectivity of phthalic anhydride over naphthoquinone and over maleic anhydride, and molar flow rates of carbon monoxide and dioxide. All such results are related to the bed temperature and gas superficial velocity.

In this work, conversion is defined according to HIMMELBLAU and RIGGS (1989)¹, by the following equation (7.13):

$$X_{NA} = \frac{F_{NA,in} - F_{NA,out}}{F_{NA,in}} \quad (7.13)$$

In equation (7.13), X_{NA} is the conversion of naphthalene (0 to 1), $F_{NA,in}$ is the molar flow rate of naphthalene that flows in the reactor (kmol h⁻¹), and $F_{NA,out}$ is the molar flow rate of naphthalene that flows out the reactor (kmol h⁻¹).

Selectivity is also defined according to HIMMELBLAU and RIGGS (1989)¹, as the molar flow rate of the desired product (in this case, the phthalic anhydride) divided by the molar flow rate of the undesired product (in this case, maleic anhydride and naphthoquinone):

$$S_{PA/NQ} = \frac{F_{PA,out}}{F_{NQ,out}} \quad (7.14)$$

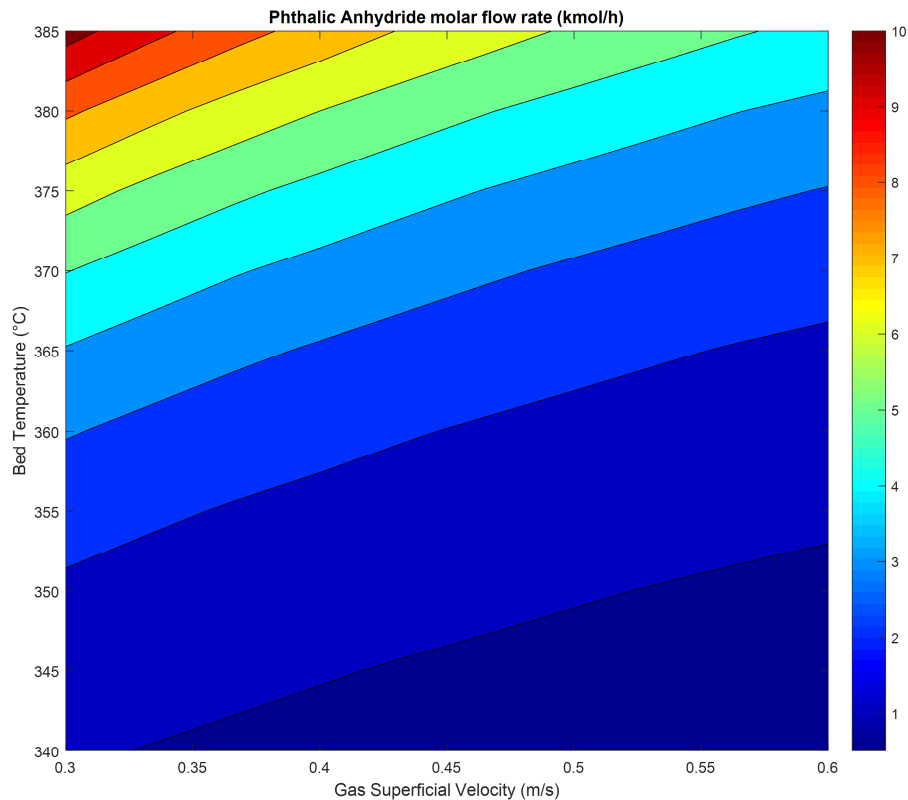
$$S_{PA/MA} = \frac{F_{PA,out}}{F_{MA,out}} \quad (7.15)$$

In equations (7.14) and (7.15), $S_{PA/NQ}$ is the selectivity of phthalic anhydride over naphthoquinone (kmol kmol^{-1}), $S_{PA/MA}$ is the selectivity of phthalic anhydride over maleic anhydride (kmol kmol^{-1}), $F_{PA,out}$, $F_{NQ,out}$ and $F_{MA,out}$ are the molar flow rate of phthalic anhydride, naphthoquinone and maleic anhydride that flows out the reactor, respectively (kmol h^{-1}).

7.2.2.1 – Phthalic Anhydride:

It was noticed that the maximum production of phthalic anhydride occurs at the maximum temperature and minimum gas velocity, as expected for a Bubbling Fluidized Bed Reactor. The lower the gas velocity, lower the gas bypass through bubbles, and higher the residence time of gas in the bed of particles. Therefore, more reactant diffuses to the catalyst particles and more product substances are formed. As expressed in figure 7.2.

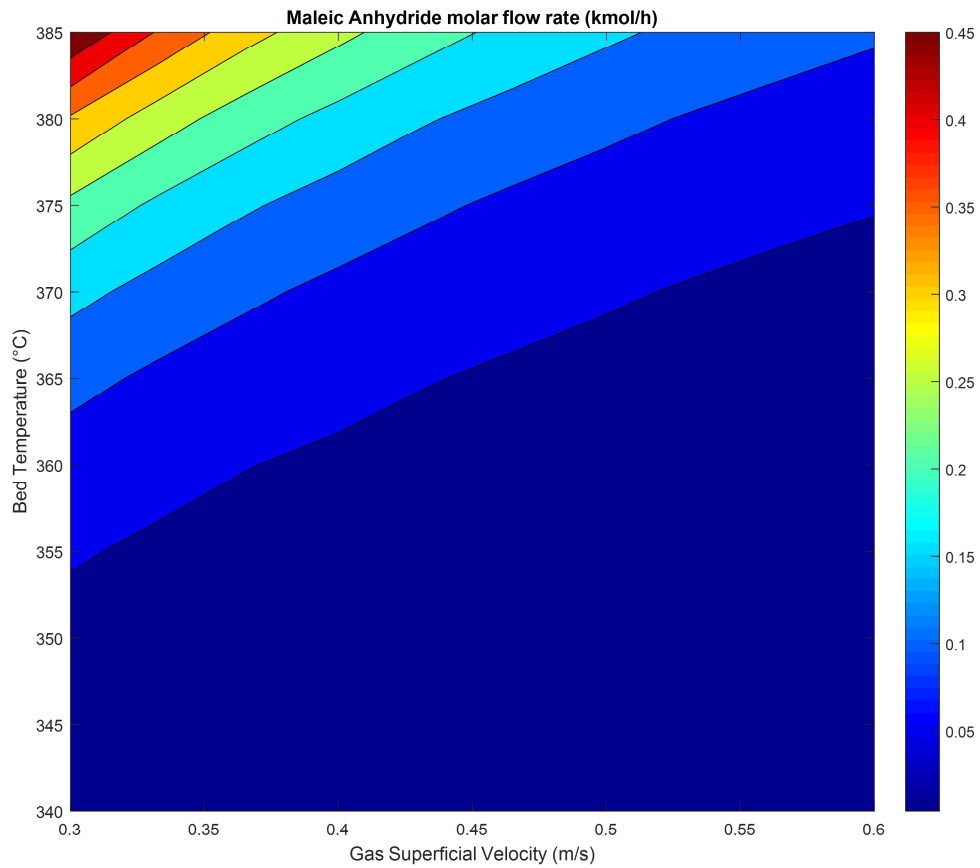
Figure 7.2 – Molar flow rate of phthalic anhydride at the reactor exit versus bed temperature and gas superficial velocity.



7.2.2.2 – Maleic Anhydride:

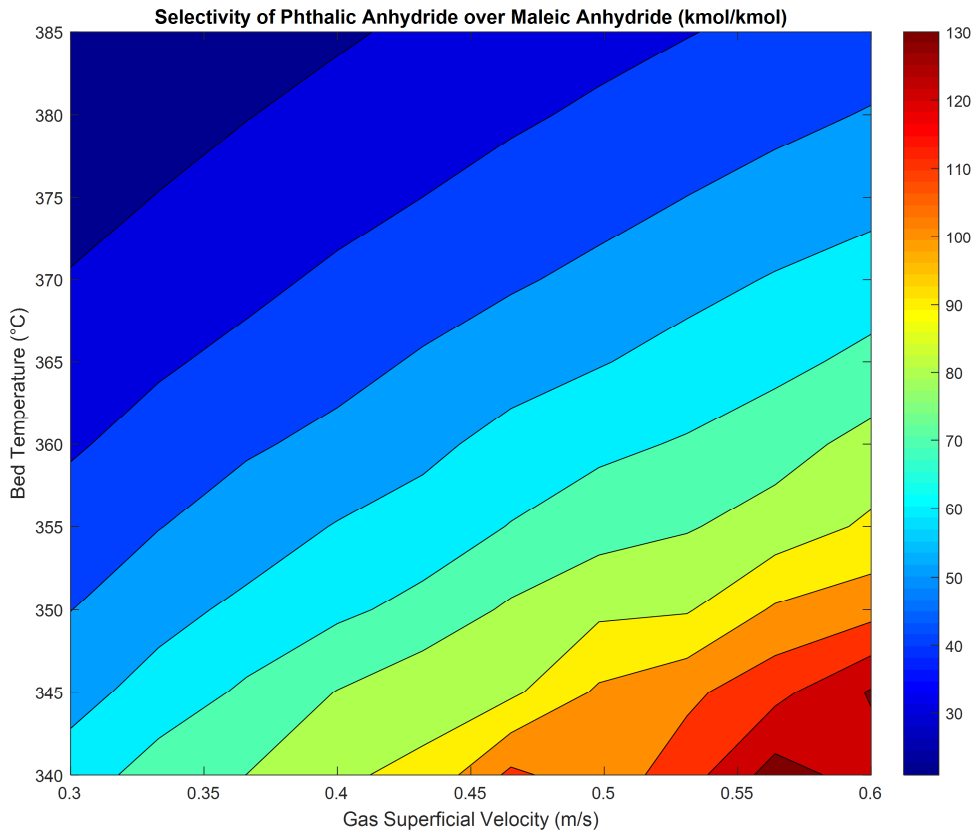
Maleic anhydride is formed through the decomposition of phthalic anhydride, so, higher the amount of phthalic anhydride, more maleic anhydride will be formed. Therefore, the maximum production of maleic anhydride coincides with the same point of the maximum production of phthalic anhydride. Figure 7.3 express this result.

Figure 7.3 – Molar flow rate of maleic anhydride at the reactor exit versus bed temperature and gas superficial velocity.



As phthalic and maleic anhydrides present the same tendency of production, *i.e.* maximum production at higher temperature and lower gas velocity, the selectivity of phthalic anhydride over maleic anhydride is expected to show the opposite behavior. The minimum and maximum values for molar flow rates are $0.502 \text{ kmol h}^{-1}$ and $10.425 \text{ kmol h}^{-1}$ for phthalic anhydride and $0.004 \text{ kmol h}^{-1}$ and $0.497 \text{ kmol h}^{-1}$, so, the behavior is really the expected, as can be seen in the figure 7.4.

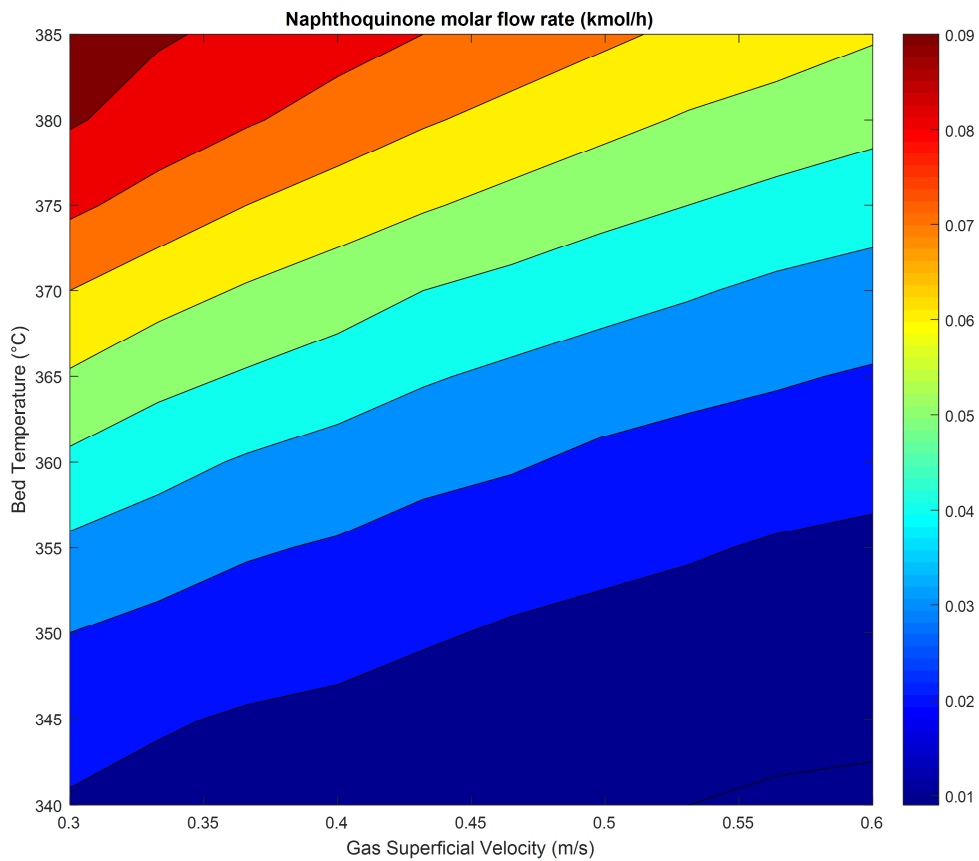
Figure 7.4 - Selectivity of phthalic anhydride over maleic anhydride.



7.2.2.3 – Naphthoquinone:

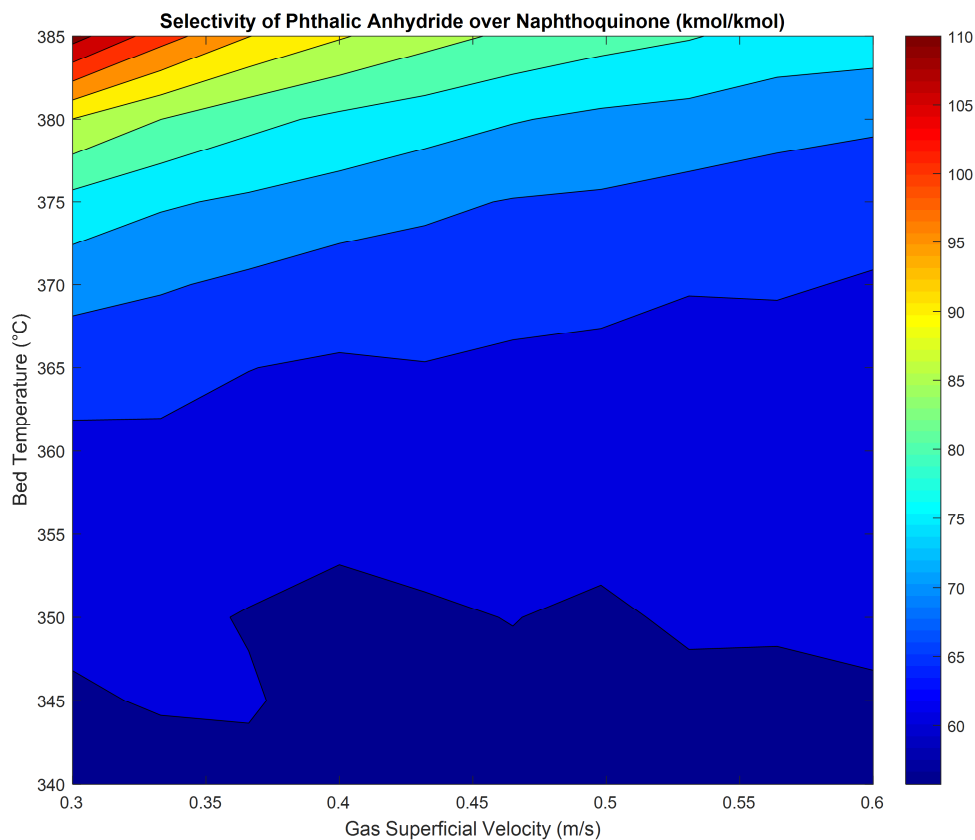
Naphthoquinone is formed by a competitive reaction to the direct formation of phthalic anhydride from naphthalene, and this competitive reaction has, in part, the same kinetic parameter (pre-exponential factor and activation energy) of the phthalic anhydride direct formation. So, it is expected to notice a similar behavior for the molar flow rate of naphthoquinone at the reactor exit, a maximum zone at the higher temperature and the lower gas velocity, as figure 7.5 express.

Figure 7.5 – Molar flow rate of naphthoquinone at the reactor exit versus bed temperature and gas superficial velocity.



However, as naphthoquinone also decomposes to form phthalic anhydride, and the activation energy for such decomposition is higher than the one for the naphthoquinone formation ($\frac{E_a}{R} = 25162.37$ K for naphthoquinone decomposition against $\frac{E_a}{R} = 19123.40$ K for naphthoquinone formation), such decomposition is more temperature-sensitive, and therefore occurs with more intensity than the naphthoquinone formation. The main result from this phenomenon is that the order of magnitude for the molar flow rate of naphthoquinone at the reactor exit is *ca.* one hundred lower than the molar flow rate of phthalic anhydride at the same point. Figure also express such difference. This difference is also reflected in the selectivity of phthalic anhydride over the naphthoquinone, by figure 7.6.

Figure 7.6 – Selectivity of phthalic anhydride over naphthoquinone.

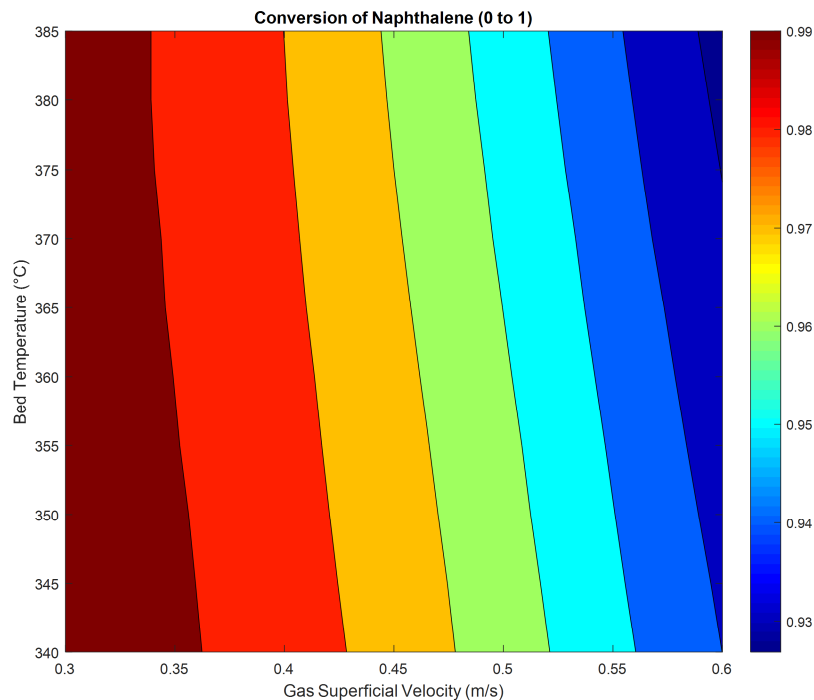


7.2.2.4 – Naphthalene conversion:

It is noticed that the conversion of naphthalene is very high. As gas velocity increases, more gas bypasses through bubbles and the reactant conversion is expected to be lower. Figure 7.7 shows such expected behavior. However, it must be emphasized that even under high gas velocity and low temperature (region where the conversion is expected to be the lower within the operational conditions of the reactor) the conversion is in the order of 92.5 to 93%.

Other noticed behavior is that the conversion seems to be less sensitive to temperature under lower gas velocities than under high gas velocities. This may be explained by the residence time of gas, which is higher under low gas velocities and provide a better mass transfer to catalyst particles. Under high gas velocities, mass transfer is less effective and temperature dependence of the reactions rate become more significant. Also is noticeable that higher the temperature, lower the conversion, because the chemical reactions are exothermic, so as much more heat is transferred out the reactor better for the conversion.

Figure 7.7 – Conversion of naphthalene.

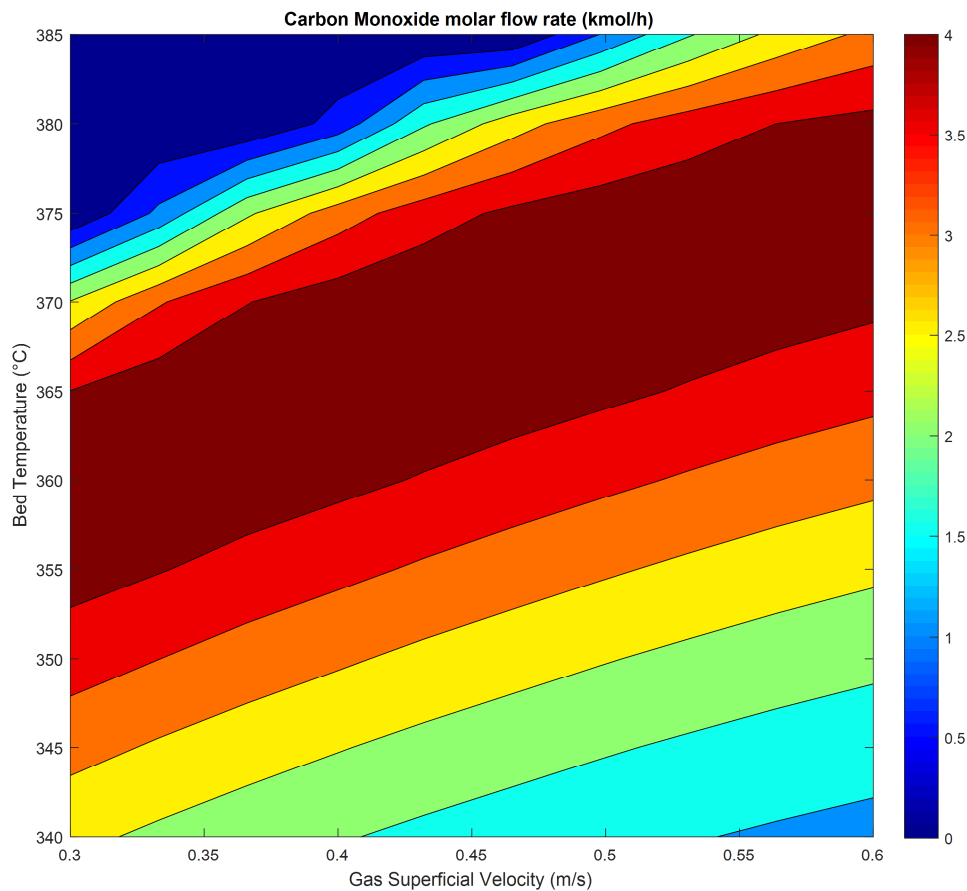


7.2.2.5 – Carbon Monoxide:

The presence of carbon monoxide in the atmosphere represent hazard for the environment. A photochemical reaction between carbon monoxide and oxygen gas produces ozone in the troposphere, the lower layer of the atmosphere from sea level to around 14 km altitude. Tropospheric ozone causes health problems.

In this sense, the amount of carbon monoxide produced must be fully burned to be released as chimney gas. Figure 7.8 shows the production of carbon monoxide according to the bed temperature and superficial gas velocity.

Figure 7.8 – Carbon monoxide at the reactor exit versus bed temperature and gas superficial velocity.

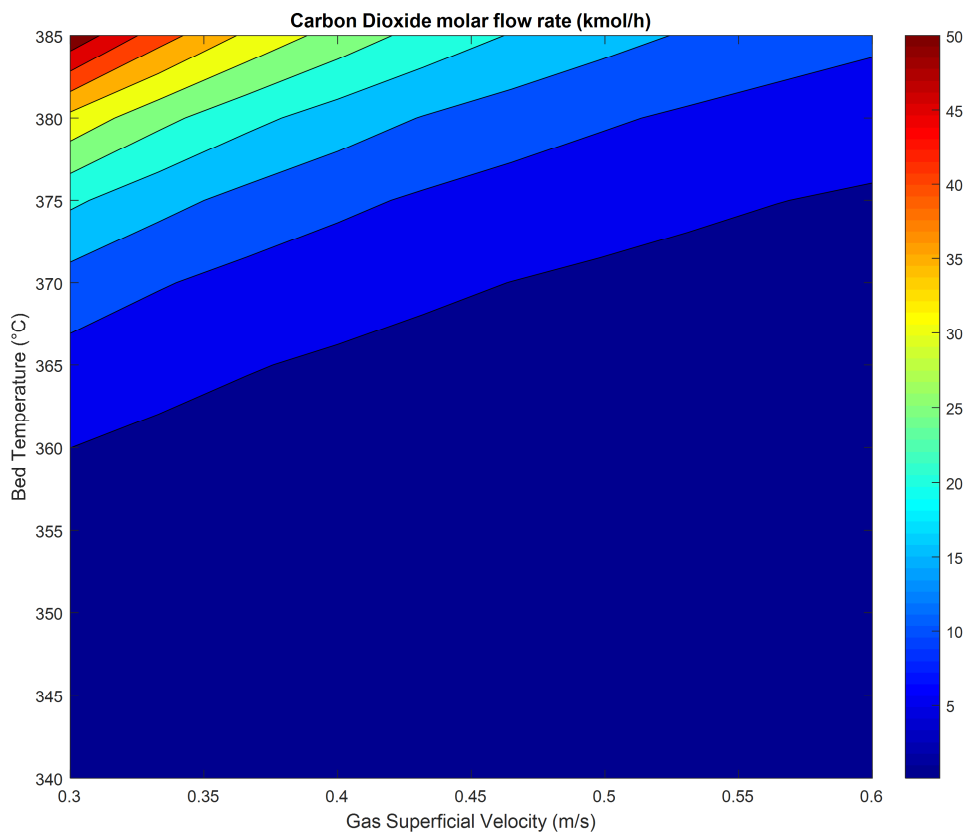


The figure 7.8 shows that higher the bed temperature and lower the gas velocity, the consumption of the produced carbon monoxide is complete.

7.2.2.6 – Carbon Dioxide:

It is environmentally important to know how much carbon dioxide is produced and may be, by consequence, released to the atmosphere. Figure 7.9 shows the carbon dioxide molar flow rate at the reactor exit with different bed temperatures and gas velocities.

Figure 7.9 – Carbon dioxide at the reactor exit versus bed temperature and gas superficial velocity.



As expected, the maximum production of carbon dioxide is at the condition of total consumption of carbon monoxide. Under lower temperature, at any gas velocity, carbon dioxide production is virtually null, indicating that the chemical reaction of oxidation of carbon monoxides is not very much affected by the gas velocity but has moderate sensibility to temperature.

7.2.2.7 – Temperature Distribution:

The gas temperature grows fast in the first meter of bed until the stability at the average bed temperature, which is the operation temperature of 636 K, controlled by the heat exchange system.

7.2.2.8 – Bed Pressure Drop:

The pressure drop along the bed height was linear, showing similar behavior to the fluidized bed pressure drop according to BASU (2006) ¹⁰.

Figure 7.10 – Temperature distribution along reactor height.

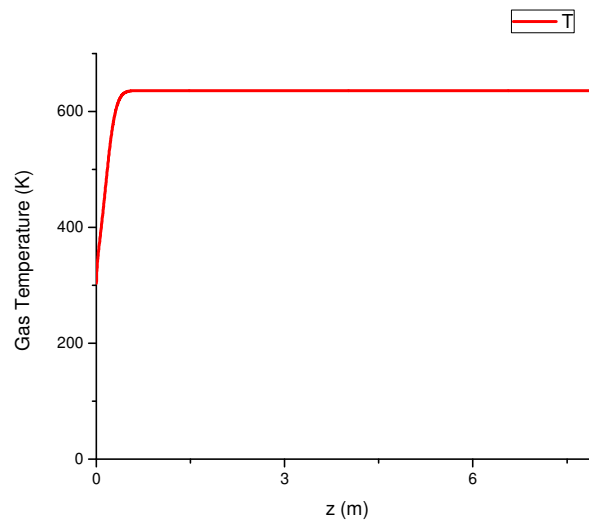
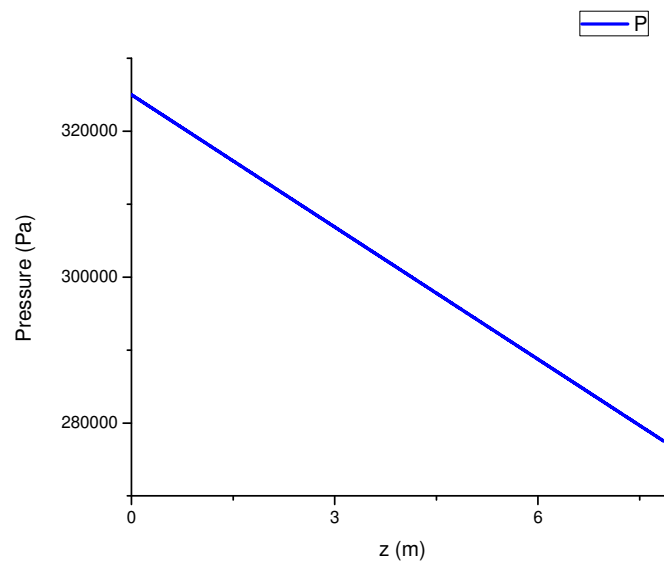


Figure 7.11 – Pressure distribution along reactor height.

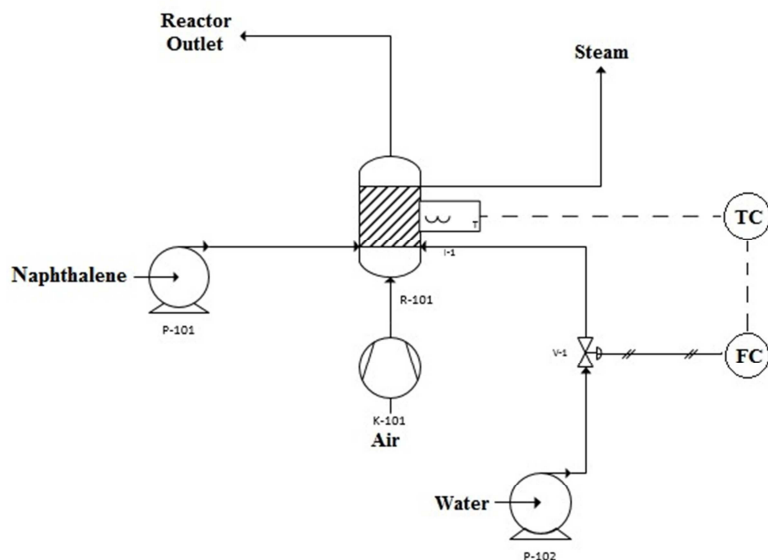


These results indicate that the best operational conditions for this bubbling fluidized bed reactor (for the phthalic anhydride production via naphthalene oxidation) is a lower superficial velocity (between 0.3 and 0.35 m s⁻¹) and higher bed temperature (between 375°C and 385°C).

Although the reduction of the gas superficial velocity trends to increase conversion, this reduction must be performed with caution, because the gas velocity may get equal or lower than the minimum fluidization velocity of the reactor catalyst and the bed loses its fluid-like behavior. This may provoke non-effective heat transfer and the reactive (and flammable) mixture of naphthalene and air may ignites and start a confined explosion (naphthalene explosive limits is 5.9% and 0.9% for upper and lower limits respectively) ⁵⁴.

Increase in the bed temperature is done by setting the control system for a higher set point. There are many different strategies to control the reactor temperature, and one very common is the cascade control (figure 7.12). Set point may be tuned from the Programmable Logic Controller (PLC) or from the DCS (Distributed Control System), according to the system which is installed in the chemical plant. Usually, the control valve is a diaphragm valve and in this case (cooling system), the valve shall be a Fail-Open valve. Other control features are important, however, they are not scope of this thesis.

Figure 7.12 – Cascade control of bed temperature.



The time spent by the user module in the execution of the reactor model coupled with the Aspen PlusTM was between thirty five to forty seconds. This is a short time frame compared to other kinds of computer simulations, such as Computational Fluid Dynamics (CFD) and Molecular Thermodynamics. However, compared to Flowsheeting simulations, this is a considerable amount of time, and in flowsheets with recycles connected to the reactor module (user module) this may become even higher due to the iterative nature of the sequential-modular strategy of process simulators.

8 – CONCLUSIONS

Conclusions were taken based on the two objectives of the thesis: the first, about the development of a detailed model for bubbling fluidized bed chemical reactor and implementation using programming language and software widely used in industrial environment (Microsoft Excel/VBA), and the second, about the coupling of the developed model coded in VBA/Excel in a commercial process simulator of wide usage in the chemical industry (Aspen PlusTM).

About the development of the reactor model, it may be concluded that:

- Modeling based on the reactor fluid dynamical behavior may give feasible physical results and more accurate than models based on ideal flow.
- Sequential-modular approach provides numerical solutions less difficult to be achieved and allow relatively satisfactory solutions for complex systems. Therefore, for practical reason, sequential-modular approach must be the first option on modeling chemical reactors with complex behavior.
- Implementation using software and programming language widely spread and available in industrial environment increases possibility of code reuse and application on other reactive systems running in same type of reactor, under same fluidization regime. Although run of VBA programs are not as fast as C++ or FORTRAN programs, Excel spreadsheets are more suitable to be a practical tool for plant engineers than other programming languages and softwares.
- Modeling also shown to be useful for kinetic parameters fit, because the accounting for non-ideal flow and usage of multiple chemical reactions allow the obtaining of values closer to real data than using ideal flow models and simplified chemical reactions schemes.

About the coupling of the Excel spreadsheet with Aspen PlusTM, it may be concluded that:

- Procedure of coupling is relatively easy and may be applied in the coupling of other models describing process unit as complex as the reactor modeled in this thesis.
- Usage of the model combined with the process simulator shown to be useful, because:
 1. It provides a better understanding of the reactor influence over the whole chemical plant.
 2. It allows engineers to have a more realistic overview of the plant performance.
 3. It provides an interesting tool for the design and retrofit of chemical plants with similar reactors.
- Although there is still the need for input of specific thermodynamics data for the set of chemical species of interest into the Excel spreadsheet, there is also the possibility to use CAPE OPEN standards to bypass this problem.
- The execution time of the model may become an important problem to be solved for complex flowsheets with recycle streams at the reactor.

The model developed in this thesis presents an alternate choice for chemical reactor simulation, because beside the specific model developed, the methodology applied may be replied with success for other kinds of complex chemical reactors.

9 – SUGGESTIONS FOR FUTURE WORKS

Bubbling Fluidized Bed Reactors are very indicated for highly exothermic chemical reactions because due to their intense solid mixing, the bed temperature is virtually uniform, which facilitates the heat transfer with external surroundings through inbed tubes. In this work, the focus was the chemical reactions and the reactor exit composition prediction, and therefore, the main suggestion for a future work is the study of the heat exchange with surfaces for the bed temperature control system.

Once the methodology applied is based on fluid dynamics analysis, a future possibility is the usage of Computational Fluid Dynamics (CFD) as a starting point to better understand the reactive flow and then create mathematical models for chemical reactors even closer to the real physical behavior.

Usage of dynamic link libraries with functions for complex calculations and written in programming languages of faster execution (such as C++ or FORTRAN) may provide great increase of efficiency and speed for the model calculations.

Other suggestion is about the model calibration. In this thesis, a random search algorithm was used to optimize temperature exponents. It is suggested for future works to apply an optimization method, such as Generalized Reduced Gradient or Simulated Annealing for the model calibration step.

About the need for thermodynamics data input, it is suggested for future works the usage of CAPE OPEN standards as a try to perform thermodynamics calculations calling Aspen PlusTM own methods and database from the VBA code.

Studies on the fractional conversion and selectivity variations with the catalyst diameter and sphericity may open discussion and research about possible ways to improve catalyst performance on fluidized bed reactors.

In the scope of design of fluidized bed reactors, an optimization study of the bed height influence over conversion and selectivity may be of industrial and academic interest.

REFERENCES

- (1) – HIMMELBLAU, D.M., RIGGS, J.B. **Basic Principles and Calculations in Chemical Engineering**. 5th Edition, Prentice Hall, 1989.
- (2) - BIEGLER, L.T., GROSSMANN, I.E., WESTERBERG, A.W. **Systematic Methods of Chemical Process Design**. Prentice Hall, 1997.
- (3) – LEVENSPIEL, O. **Chemical Reaction Engineering**. 3rd Edition. John Wiley & Sons, 1999.
- (4) - KUNII, D., LEVENSPIEL, O. **Fluidization Engineering**, 2nd Edition. Butterworth-Heinemann, 1991.
- (5) – FOGLER, H.S. **Elements of Chemical Reaction Engineering**. 4th Ed. Prentice Hall, 2006.
- (6) – FURUSAKI, S. **Reactor Types and Their Applications**. In: Chemical Reactor and Reactor Design, Chapter 4.1, John Wiley & Sons, 1997.
- (7) – CARBERRY, J.J. **Chemical and Catalytic Reaction Engineering**. Dover Publications, 2001.
- (8) – RICHARDSON, J.F., PEACOCK, D.G. **Coulson & Richardson's Chemical Engineering**, vol. 3, 3rd Edition, 1994.
- (9) – LUYBEN, W.L. **Chemical Reactor Design and Control**. John Wiley & Sons, 2007.
- (10) – BASU, P. **Combustion and Gasification in Fluidized Beds**. Taylor & Francis, 2006.
- (11) - GELDART, D. Types of Gas Fluidization. **Powder Technology**, vol. 7, pp. 285-292, 1973.
- (12) – HO, T.C. **Modeling**. In: Handbook of Fluidization and Fluid-Particle Systems. Chapter 9, Marcel Dekker, 2003.
- (13) – SOTUDEH-GHAREBAAGH, R., LEGROS, R., CHAOUKI, J., PARIS, J. Simulation of circulating fluidized bed reactors using ASPEN PLUS. **Fuel**, vol. 77, issue 4, pp. 327-337, 1998.
- (14) – NIKOO, M.B., MAHINPEY, N. Simulation of biomass gasification in fluidized bed reactor using ASPEN PLUS. **Biomass and Bioenergy**, vol. 32, issue 12, pp. 1245-1254, 2008.

- (15) – ABDELOUAHED,L. AUTHIER,O., MAUVIEL,G., CORRIOU,J.P., VERDIER,G., DUFOUR,A. Detailed Modeling of Biomass Gasification in Dual Fluidized Bed Reactors under Aspen Plus. **Energy & Fuels**, vol. 26, issue 6, pp. 3840-3855, 2012.
- (16) – BEHESHTI, S.M., GHASSEMI, H., SHAHSAVAN-MARKADEH, R. Process simulation of biomass gasification in a bubbling fluidized bed reactor. **Energy Conversion and Management**, vol. 94, pp.345-352, 2015.
- (17) – KAUSHAL,D., TYAGI.R. Advanced simulation of biomass gasification in a fluidized bed reactor using ASPEN PLUS. **Renewable Energy**, vol. 101, pp.629-636, 2017.
- (18) - DAVIDSON, J.F., HARRISON,D. **Fluidized Particles**. Cambridge Press, 1963.
- (19) - ROWE, P.N., PARTRIGDE, B.A., LYALL, E. Cloud formation around bubbles in gas fluidized beds. **Chemical Engineering Science**, vol. 19, issue 12, p. 973-985, 1964.
- (20) - WERTHER, J. Hydrodynamics and Mass Transfer between the Bubble and Emulsion Phases in Fluidized Beds of Sand and Cracking Catalyst. In: **Fluidization IV**, p. 93, Engineering Foundation, 1983.
- (21) - MURRAY, J.D. On the mathematics of fluidization. Part 2: Steady motion of fully developed bubbles. **Journal of Fluid Mechanics**, vol. 22, issue 1, p. 57-80, 1965.
- (22) - TOEI, R., MATSUNO,R., KOJIMA,H., NAGAI,Y., NAKAGAWA, K., YU, S. Behaviours of Bubbles in Gas-Solid Fluidized-Bed. **Kagaku Kogaku**, vol. 29, issue 11, p. 851-857, 1965.
- (23) - HORIO, M., NONAKA, A. A Generalized Bubble Diameter Correlation for Gas-Solid Fluidized Beds. **AIChE Journal**, vol. 33, issue 11, p. 1865-1872, 1987.
- (24) - RÜDISÜLI, M., SCHILDHAUER, T.J., BIOLLAZ, S.M.A., WOKAUN, A., VAN OMMEN, J.R. Comparison of bubble growth obtained from pressure fluctuation measurements to optical probing and literature correlations. **Chemical Engineering Science**, vol. 74, p. 266-275, 2012.
- (25) - CHAPRA, S.C., CANALE, R.P. **Numerical Methods for Engineers**. 5th Edition, McGraw-Hill, 2006.

- (26) - BOYCE, W.E., DiPRIMA, R.C. **Elementary Differential Equations and Boundary Value Problems**. 7th Edition, John Wiley and Sons, 2000.
- (27) - HOFFMAN, J.D. **Numerical Methods for Engineers and Scientist**. 2nd Edition, Marcel Dekker, 2001.
- (28) - ERGUN, S. Fluid Flow Through Packed Columns. **Chemical Engineering Progress**, vol. 48, issue 2, p. 89-94, 1952.
- (29) - ABRAHAMSEN, A.R., GELDART, D. Behavior of Gas-Fluidized Beds of Fine Powders. Part II: Voidage of the Dense Phase in Bubbling Beds. **Powder Technology**, vol. 26, issue 1, p. 47-55, 1980.
- (30) - SCHNITZLEIN, M.G., **Hydrodynamics of a fast fluidized bed characterized by its pressure signals**. Ph.D. Thesis, City University of New York (CUNY), 1987.
- (31) - HAIDER, A., LEVENSPIEL, O. Drag Coefficient and Terminal Velocity of Spherical and Nonspherical Particles. **Powder Technology**, vol. 58, issue 1, p. 63-70, 1989.
- (32) - KUNII, D., LEVENSPIEL, O. Entrainment of Solids from Fluidized Beds I. Hold-up of Solids in the Freeboard, II. Operation of Fast Fluidized Beds. **Powder Technology**, vol. 61, issue 2, p.193-206, 1990.
- (33) - MONTGOMERY, D.C., RUNGER, G.C. **Applied Statistics and Probability for Engineers**, 2nd Edition, John Wiley and Sons, 1999.
- (34) - McCABE, W.L., SMITH, J.C., HARRIOTT, P. **Unit Operations of Chemical Engineering**. 5th Edition, Mc-Graw Hill, 1993.
- (35) - GOMIDE, R. **Operações Unitárias**, vol. 3: separações mecânicas. 1980.
- (36) - MACINTYRE, A.J. **Ventilação Industrial e Controle da Poluição**. LTC-Livros Técnicos e Científicos Editora, 1990.
- (37) - GELDART, D., ABRAHAMSEN, A.R. Homogeneous Fluidization of Fine Powders Using Various Gases and Pressures. **Powder Technology**, vol. 19, pp. 133-136, 1978.
- (38) - ASPEN TECH, **Aspen Plus User Models**. V. 7.3, March 2011.
- (39) - CHAUVEL, A. LEFEBVRE, G. **Petrochemical Processes: Technical and Economic characteristics**. Vol. 2: Major Oxigenated, Chlorinated and Nitrated Derivatives. Institut Français du Pétrole Publications, 1989.

- (40) - PHTHALIC ACIDS AND OTHER BENZENE POLICARBOXYLIC ACIDS. In: **Kirk-Othmer Encyclopedia of Chemical Technology**. 4th Edition, Vol. 18: PAPER – PIGMENT DISPERSIONS, 1998.
- (41) - DeMARIA, F., LONGFIELD, J.E., BUTLER, G. Catalytic Reactor Design. **Industrial and Engineering Chemistry**, vol. 53, issue 4, p. 259-266, 1961.
- (42) - D'ALESSANDRO, A.F., FARKAS, A. The kinetics of catalytic oxidation of naphthalene. **Journal of Colloid Science**, vol. 11, p. 653-670, 1956.
- (43) - PETERSON, T.I. Kinetics and mechanism of Naphthalene oxidation by non-linear estimation. **Chemical Engineering Science**, vol. 17, p. 203-219, 1962.
- (44) - ARRHENIUS, S. Über die Reaktionsgeschwindigkeit bei der Inversion von Rohrzucker durch Säuren. **Zeitschrift für Physikalische Chemie**, vol. 4, issue 1, p. 226-248, 1889.
- (45) - CARBERRY, J.J., WHITE, D. On the Role of Transport Phenomena in Catalytic Reactor Behavior. **Industrial and Engineering Chemistry**, vol. 61, issue 7, p. 27-35, 1969.
- (46) - LAIDLER, K.J. A Glossary of Terms Used in Chemical Kinetics, Including Reaction Dynamics. **Pure and Applied Chemistry**, vol. 68, issue 1, p. 149-192, 1996.
- (47) - WALPOLE, R.E., MYERS, R.H., MYERS, S.L., YE, K. **Probability and Statistics for Engineers and Scientist**. 8th Edition, Pearson, 2007.
- (48) - ROSS, S.M. **Introduction to Probability and Statistics for Engineers and Scientists**. 3rd Edition, Elsevier Academic Press, 2004.
- (49) - DUTTA, S., SUCIU, G.D. Unified Model Applied to the scale-up of Catalytic Fluid Bed Reactors of Commercial Importance. In: **Fluidization VI**. Editors: J.R. Grace, L.W. Shemilt, M.A. Bergougnou. 1989.
- (50) – ASPEN TECH, **Aspen Physical Property System**: physical property models. V8.4, 2013. Chapter 2: Thermodynamic Property Model, p.228.
- (51) - PERRY, R.H., GREEN, D.W. **Perry's Chemical Engineers' Handbook**. 7th Edition, McGraw-Hill, 1999.
- (52) - JOHNSON, J.E., GRACE, J.R., GRAHAM, J.J. Fluidized –Bed Reactor Model Verification on Reactor of Industrial Scale. **AIChE Journal**, vol. 33, issue 4, p. 619-627, 1987.

- (53) - EDGAR, T.F., HIMMELBLAU, D. M., LASDON, L.S. – **Optimization of Chemical Processes**. 2nd Edition, McGraw-Hill, 2001.
- (54) – CDH FINE CHEMICAL, **Material Safety Data Sheet**: Naphthalene. CAS n° 91-20-3.
- (55) - BERGMAN, T.L., LAVINE, A.S., INCROPERA, F.P., DEWITT, D.P. **Fundamentals of Heat and Mass Transfer**. 7th Edition, John Wiley and Sons, 2011.
- (56) - PRITCHARD, P.J. **Fox and McDonald's INTRODUCTION TO FLUID MECHANICS**, 8TH Edition, John Wiley and Sons, 2011.
- (57) - KUNDU, P.K., COHEN, I.M. **Fluid Mechanics**. 4th Edition, Academic Press, 2008.
- (58) - MUNSON, B.R., YOUNG, D.F., OKIISHI, T.H., HUEBSCH, W.W. **Fundamentals of Fluid Mechanics**. 6th Edition, John Wiley and Sons, 2009.
- (59) - BIRD, R.B., STEWART, W.E., LIGHTFOOT, E.N. **Transport Phenomena**. 2nd Edition, John Wiley and Sons, 2002.
- (60) - SINHA, A.P., PARAMESHWAR DE. **Mass Transfer**: Principles and Operations. PHI Learning, 2012.
- (61) - BAEHR, H.D., STEPHAN, K. **Heat and Mass Transfer**. 3rd Edition, Springer, 2006.
- (62) - ASANO, K. **Mass Transfer**: From Fundamentals to Modern Industrial Applications. Wiley-VCH, 2006.
- (63) - RANZ, W.E., MARSHALL, W.R. Evaporation from Drops, Part I and Part II. **Chemical Engineering Progress**, Vol. 48. Issue 3, p. 141-146, Issue 4, p. 173-180. 1952.
- (64) - SCALA, F. Mass Transfer around Active Particles in Fluidized Beds. In.: **Mass Transfer in Multiphase Systems and its Applications**. Editor: Mohamed El-Amin, Intech, 2011.
- (65) - RANZ, W.E. Friction and transfer coefficients for single particles and packed beds. **Chemical Engineering Progress**, vol. 48, p. 247-253, 1952.
- (66) - GELPERIN, N.I., EINSTEIN, V.G., In: **Fluidization**. Editors: J.F. Davidson and D. Harrison, p. 471-517, Academic Press, 1971.
- (67) - KOTHARI, A.K. M.S. thesis, Illinois Institute of Technology, 1967.

- (68) - MISSEN, R.W., MIMS, C.A., SAVILLE, B.A. **Introduction to Chemical Reaction Engineering and Kinetics**. John Wiley & Sons, 1999.
- (69) - COKER, A.K. **Modeling of Chemical Kinetics and Reactor Design**. Gulf Professional Publishing, 2001.
- (70) - BRAUNER, N., SHACHAM, M. Using Power-law Rate Expression Parameters for Discrimination Among Mechanistic Models In Rate Data Regression. **Chemical Engineering Communications**, vol. 155, issue 1, p.1-18, 1996.
- (71) - SMITH, J.M., VAN NESS, H.C., ABBOTT, M.M. **Introduction to Chemical Engineering Thermodynamics**. 6th Edition, McGraw-Hill, 2001.
- (72) - CASTELLAN, G. **Fundamentos de Físico-Química**. LTC, 1986.
- (73) - VAN DER WAALS, J. D. **Over de continuïteit van den gas- en vloeistofoestand**. 1873. 154 p. Thesis (Doctorate) – Universiteit Leiden, 1873.
- (74) - REDLICH, O., KWONG, J.N.S. On the Thermodynamics of Solutions V: An Equation of State. Fugacities of Gaseous Solutions. In: SYMPOSIUM ON THERMODYNAMICS AND MOLECULAR STRUCTURE OF SOLUTIONS – 114TH MEETING OF THE AMERICAN CHEMICAL SOCIETY, Portland, Oregon, September 13th and 14th 1948.
- (75) - SOAVE, G. Equilibrium constants from a modified Redlich-Kwong equation of state. **Chemical Engineering Science**, vol. 27, issue 6, p. 1197-1203, 1972.
- (76) - PENG, D.Y., ROBINSON, D.B. A New Two-Constant Equation of State. **Industrial and Engineering Chemistry Fundamentals**, vol. 15, issue 1, p.59-64, 1976.
- (77) - TSONOPOULOS, C., HEIDMAN, J.L. From Redlich-Kwong to Present. **Fluid Phase Equilibria**, vol. 24, issue , p.1-23, 1985.
- (78) - SANDLER, S.I. **Chemical, Biochemical and Engineering Thermodynamics**. 4th Edition, John Wiley and Sons, 2006.
- (79) - PRAUSNITZ, J.M., LICHTENTHALER, R.N., GOMES DE AZEVEDO, E. **Molecular Thermodynamics of Fluid-Phase Equilibria**. 3rd Edition, Prentice Hall, 1999.
- (80) - DE HEMPTINNE, J.C., LEDANOIS, J.M., MOUGIN, P. BARREAU, A. **Select Thermodynamic Models for Process Simulation: A Practical Guide Using Three Steps Methodology**. IFP Energies Nouvelles Publications, 2012.

- (81) - STRYJEK, R., VERA, J.H. PRSV: An improved Peng-Robinson Equation of State for Pure Compounds and Mixtures. **The Canadian Journal of Chemical Engineering**, vol. 64, issue 2, p.323-333, 1986.
- (82) - ELLIOTT, J.R., LIRA, C.T. **Introductory Chemical Engineering Thermodynamics**. 2nd Edition, Prentice Hall, 2012.
- (83) - WOOD, A. **Introduction to Numerical Analysis**. Addison Wesley Longman, 1999.
- (84) - PITZER, K.S., LIPPMANN, D.Z., CURL Jr., R.F., HUGGINS, C.M., PETERSEN, D.E. The Volumetric and Thermodynamic Properties of Fluids II. Compressibility Factor, Vapor Pressure and Entropy of Vaporization. **Journal of American Chemical Society**, vol. 77, issue 13, p.3433-3440, 1955.

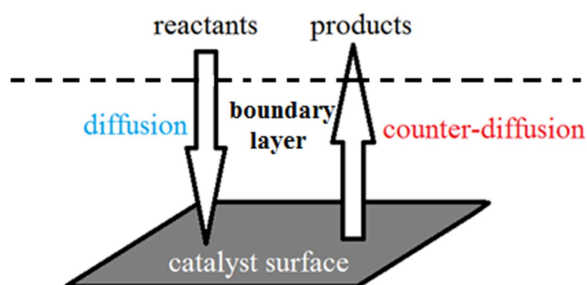
APPENDICE A – Particle-to-gas Heat and Mass Transfer

Particle-to-gas Mass Transfer

Mass transfer is a phenomenon that occurs as a result of a concentration gradient in the mixture, and may happen according to different mechanisms: diffusion and advection. Diffusion occurs due to random motion of fluid molecules while advection occurs due to a bulk fluid of motion.⁵⁵

As fluid flows over the catalyst particle, a thin layer of fluid is formed over the body, the boundary layer.^{56, 57, 58} To react, substances from the bulk flow must flow to and from the catalyst surface through the boundary layer, so heat and mass transfer must occur over the particles.⁵⁹

Figure A1– Diffusion and counter-diffusion of substances through the boundary layer.



Transfer of substances at the surface occurs only by diffusion.⁵⁵ The rates of both diffusion and advection depend on the concentration gradient. So, rates of mass transfer are generally expressed in terms of mass transfer coefficient.⁶⁰

$$N_i = k_d \cdot (C_i - C_{i,s}) \quad (\text{A1})$$

In equation (A1), N_i is the molar flux of the i -th substance ($\text{kmol s}^{-1} \text{m}^{-2}$), k_d is the convection mass transfer coefficient (m s^{-1}), C_i represent the concentration of the i -th substance in the bulk flow and $C_{i,s}$ at the catalyst surface.

Under industrial operating conditions, chemical reactions are usually controlled by mass transfer, instead of by chemical kinetics, due to the high solid temperature, which provides high reaction rates. This means that under the usual conditions, chemical reactions are not the limiting step of the process, and usually the concentrations of reactants substances on the catalyst surface is small enough to be

negligible or considered null. In this way, for reactants species, equation (A1) can be resumed to:

$$N_{reactant} = k_d \cdot C_{reactant} \quad (A2)$$

Or in terms of molar flow rate:

$$F_{i,d} = k_d \cdot \frac{S_{cat}}{q} \cdot F_{i,b} \quad (A3)$$

In equation (A3), $F_{i,d}$ represents the molar flow rate of the i -th reactant which diffuses to the catalyst surface (kmol s^{-1}), S_{cat} is the catalyst surface (m^2), q is the gas volume flow rate and $F_{i,b}$ is the molar flow rate of the i -th reactant in the bulk flow (kmol s^{-1}).

It is proposed that only reactant species diffuse to catalyst surface, while only product species and excess of reactants counter-diffuse from catalyst surface.

Mass and heat transfer coefficients are often described in terms of dimensionless groups. If any transport phenomenon can be accurately described by a set of dimensionless groups, the model developed also describes other systems under similar conditions.⁶⁰ Therefore, many correlations for heat and mass transfer coefficients were developed for many different set of conditions and environments.

One of the correlations for heat and mass transfer in fluidized beds was described by BAEHR and STEPHAN (2006)⁶¹:

$$Ar = \frac{d_p^3 \rho_g (\rho_s - \rho_g) g}{\mu^2} \quad (A4)$$

$$Re_p = 19.14 \cdot \left[\left(1 + \frac{Ar^{1.8}}{12.84} \right)^{0.5} - 1 \right]^{1.8} \quad (A5)$$

$$Sh_{lam} = 0.664 \cdot Re_p^{0.5} \cdot Sc^{0.333} \quad (A6)$$

$$Sh_{turb} = \frac{0.037 \cdot Re_p^{0.8} \cdot Sc}{1 + 2.443 \cdot Re_p^{-0.1} (Sc^{0.666} - 1)} \quad (A7)$$

$$Sh_m = 2 + (Sh_{lam}^2 + Sh_{turb}^2)^{0.5} \quad (A8)$$

$$k_d = \left(\frac{Diff}{d_p} \right) \cdot Sh_m \quad (A9)$$

Equations (A4) to (A9) are valid in the range of $1 \leq Re_p \leq 10^6$, $0.7 \leq Sc \leq 70000$. In equations (A4) to (A9), Ar represents the Archimedes number, Re_p is the particle Reynolds number, Sh_{lam} , Sh_{turb} and Sh_m are respectively the laminar, turbulent and mean Sherwood numbers and $Diff$ is the gas diffusivity ($m^2 s^{-1}$).

Other correlation described by ASANO (2006)⁶², deals with a principle known as void function, which is a kind of correction function of single particle heat and mass transfer to fluidized beds. The single particle transfer is described by correlation published by RANZ-MARSHALL (1952)⁶³:

$$Sh_{particle} = 2 + 0.6 \cdot Re_p^{0.5} \cdot Sc^{0.333} \quad (A10)$$

$$Sh_{FB} = \frac{Sh_{particle}}{1 + 1.32 \cdot \epsilon_{sd}^{0.76}} \quad (A11)$$

In equation (A11), ϵ_{sd} represents the fraction of the bed occupied by solids.

Furthermore, another important work on mass transfer in fluidized beds is the one described by SCALA (2011)⁶⁴, in which a model based on experimental data from carbon monoxide catalytic oxidation on Pt catalyst was developed:

$$Sh = 2 \cdot \epsilon_{mf} + 0.7 \cdot \left(\frac{Re_{mf}}{\epsilon_{mf}} \right)^{0.5} \cdot Sc^{0.333} \quad (A12)$$

Particle-to-gas Heat Transfer

Due to the temperature uniformity of fluidized beds, they are recommended for highly exothermic catalytic reactions.⁴ The mean temperature of the bed is usually controlled by internal tubes for heat exchange, so there is a temperature gradient between the particles and the gas. Once chemical reactions occur on catalyst surface and the solids are at a different temperature than the measured in the bed, it is necessary to calculate the temperature of the particles in order to evaluate the products distribution.

Basically, the energy balance over the particle results in:

$$\dot{Q} = \Delta H_{rxn} \quad (A13)$$

In equation (A13), \dot{Q} represents the rate of heat exchanged between particles and gas and $\Delta\dot{H}_{rxn}$ is the thermal charge of the set of chemical reactions.

The rate of heat exchange between particles and gas can be estimated by the following equation:

$$\dot{Q} = h \cdot S_{cat}^{total} \cdot (T_s - T_{oper}) \quad (A14)$$

And finally:

$$T_s = T_{oper} + \frac{\Delta\dot{H}_{rxn}}{h \cdot S_{cat}^{total}} \quad (A15)$$

In equation (3.102), T_s is the solid temperature (K), T_{oper} is the operation temperature of the bed (K), h is the heat transfer coefficient ($W m^{-2} K^{-1}$) and S_{cat}^{total} the total catalyst surface (m^2).

The total catalyst surface is estimated by the multiplication between the total number of particles in the bed and the surface of one single particle:

$$S_{cat}^{total} = N_p^{total} \cdot S_{cat} \quad (A16)$$

$$N_p^{total} = \frac{6 \cdot \epsilon_{sd} A_{cs} H_{max}}{d_p \varphi_s} \quad (A17)$$

$$S_{cat} = \pi d_p^2 \quad (A18)$$

Many investigators studied the particle-to-gas heat transfer in fluidized beds, and many correlations for heat transfer coefficient were developed. RANZ (1952)⁶⁵, provided the equations (A19) and (A20) for heat transfer in a single sphere and in a packed bed respectively:

$$Nu_{sph} = 2 + 0.6 \cdot Re_p^{0.5} Pr^{0.333} \quad (A19)$$

$$Nu_{PB} = 2 + 1.8 \cdot Re_p^{0.5} Pr^{0.333} \quad (A20)$$

For fluidized beds, heat transfer coefficient falls between the values for packed beds and those for single particles.⁶¹ KUNII and LEVENSPIEL (1991)⁴ used data from GELPERIN and EINSTEIN (1971)⁶⁶ and KOTHARI (1967)⁶⁷ to provide the following model:

$$\text{for } Re_p > 100 : Nu_{FB} = 0.5 \cdot (Nu_{sph} + Nu_{PB}) \quad (A21)$$

$$\text{for } Re_p \leq 100 : Nu_{FB} = 0.03 \cdot Re_p^{1.3} \quad (A22)$$

$$h = Nu_{FB} \cdot \left(\frac{k_g}{d_p} \right) \quad (\text{A23})$$

A more recent model described by BAEHR and STEPHAN (2006)⁶¹ estimates the heat transfer coefficient based on the external flow over a sphere:

$$Ar = \frac{d_p^3 \rho_g (\rho_s - \rho_g) g}{\mu^2} \quad (\text{A24})$$

$$Re_p = 19.14 \cdot \left[\left(1 + \frac{Ar^{\frac{1}{1.8}}}{12.84} \right)^{0.5} - 1 \right]^{1.8} \quad (\text{A25})$$

$$Nu_{lam} = 0.664 \cdot Re_p^{0.5} \cdot Pr^{0.333} \quad (\text{A26})$$

$$Nu_{turb} = \frac{0.037 \cdot Re_p^{0.8} \cdot Pr}{1 + 2.443 \cdot Re_p^{-0.1} (Pr^{0.666} - 1)} \quad (\text{A27})$$

$$Nu_{FB} = 2 + (Nu_{lam}^2 + Nu_{turb}^2)^{0.5} \quad (\text{A28})$$

ASANO (2006)⁶², also described the heat transfer in fluidized beds in terms of a void function:

$$Nu_{particle} = 2 + 0.6 \cdot Re_p^{0.5} \cdot Pr^{0.333} \quad (\text{A29})$$

$$Nu_{FB} = \frac{Nu_{particle}}{1 + 1.32 \cdot \epsilon_{sd}^{0.76}} \quad (\text{A30})$$

APPENDICE B – Chemical Reactions Approach

Chemical reactions are usually separated between single reactions (only one reaction occurs in the system) and multiple reactions. The latter case is the most frequent.⁵

Multiple reactions may be ordered in two primary types: parallel reactions and series reactions. In parallel reactions, the reactant specie simultaneously forms two or more different products, while in series reactions the just formed product react and form other product, and this pattern repeats on and on. Furthermore, series-parallel combinations of chemical reactions often occur.³

The rate of formation or consumption of products and reactants depend on some environmental and operational conditions, such temperature, pressure and concentrations.^{68,69} Mathematical structure of the rate law varies, however, homogeneous reactions usually follow a simple power law function, and catalytic reactions usually follow a Langmuir-Hinshelwood model due to the phenomena of adsorption and desorption associated to the chemical reactions. Power law and Langmuir-Hinshelwood models are described in equations (B1) and (B2) respectively as shown by BRAUNER and SHACHAM (1996)⁷⁰.

$$r = k \cdot \prod_{i=1}^{N_{comp}} x_i^{n_i} \quad (\text{B1})$$

$$r = k \cdot \frac{\prod_{i=1}^{N_{comp}} x_i^{n_i}}{\left[A_0 + \sum_{i=1}^{N_{comp}} x_i^{m_i} \right]^n} \quad (\text{B2})$$

In industrial practice, kinetic models are often fit to power law equations, even for chemical reactions which follow Langmuir-Hinshelwood kinetics, due to the mathematical simplicity behind power law model.

Once the reactant species diffuse to the catalyst surface, they are adsorbed, chemical reactions occur, product species are desorbed and diffuse back to bulk flow. Diffusion of reactants is calculated in this paper through mass transfer models. However, formation and consumption of species is calculated by kinetic model of the chemical reactions such species are involved:

$$F_{form/cons}(i) = r_i^{net} \quad (\text{B3})$$

$$r_i^{net} = \sum_{j=1}^{N_{rxn}} \nu_{ij} \cdot r_j \quad (\text{B4})$$

In equation (B3), r_i^{net} is the net reaction rate of the i-th specie (kmol s^{-1}), and in equation (B4), N_{rxn} is the number of chemical reactions, ν_{ij} is the stoichiometric coefficient of the i-th specie at the j-th reaction (positive for product and negative for reactant), and r_j is the rate law for the j-th reaction (kmol s^{-1}). After the calculation of the molar flow rates of formation or consumption for all species, the molar flow rate of counter-diffusion of species is calculated by equation (B5):

$$F_{cd}(i) = F_d(i) + F_{form}(i) - F_{cons}(i) \quad (\text{B5})$$

APPENDICE C - Solids Distribution

The volume of bed is calculated multiplying the reactor cross-section by the bed maximum height (the height reached after bed expansion):

$$V_{bed} = A_{cs} \cdot H_{max} \quad (C1)$$

The maximum height of the bubbling fluidized bed is divided in a number of intervals of constant size Δz , so the number of height intervals is:

$$N_z = \frac{H_{max}}{\Delta z} \quad (C2)$$

Other important number of intervals to be calculated is the number of divisions of the cloud gas path, which means the number of catalytic CSTRs the cloud represents and can be calculated by the following equation:

$$N_s = \frac{S}{\Delta s} \quad (C3)$$

In fluidized beds, particles are dispersed in the emulsion phase and in the system bubble-cloud-wake. In the bubble-cloud-wake system, there are more particles in the cloud and in the wake, so the amount of particles in the bubble is negligible compared to those in the other two zones. The volume of bed occupied by the system bubble-cloud-wake is calculated by the following equation:

$$V_{bcw} = \delta \cdot V_{bed} \quad (C4)$$

In equation (C4), δ is the bubble volume fraction (m^3 of bubbles / m^3 of bed).

The volume of bed occupied by the emulsion is therefore:

$$V_e = (1 - \delta) \cdot V_{bed} \quad (C5)$$

The cloud volume is calculated multiplying the volume of the system bubble-cloud-wake by the cloud volume fraction:

$$V_{cloud} = f_c \cdot V_{bcw} \quad (C6)$$

The wake volume is calculated multiplying the volume of the system bubble-cloud-wake by the wake volume fraction:

$$V_{wake} = f_w \cdot V_{bcw} \quad (C7)$$

Considering the wake with the same void fraction of the bed under minimum fluidization, the volume of particles in the wake is calculated by the following equation:

$$V_{cat-wake} = (1 - \epsilon_{mf}) \cdot f_w \cdot V_{bcw} \quad (C8)$$

The number of particles in the wake at one interval Δz is estimated dividing the volume of particles in the wake by the volume of a single particle and by the number of divisions of the bed height:

$$Np_{wake\Delta z} = \frac{V_{cat-wake}}{\frac{1}{6}\pi(\varphi_s d_p)^3 \cdot N_z} \quad (C9)$$

The volume of particles in the cloud at one interval Δz and one interval Δs is estimated by the following equation:

$$V_{cat-cloud\Delta z,\Delta s} = \frac{\gamma_c V_{bcw}}{N_z N_s} \quad (C10)$$

In equation (C10), γ_c represents the volume of solids in cloud per volume of the system bubble-cloud-wake, and is calculated by the following equation:

$$\gamma_c = (1 - \epsilon_{mf})(f_c + f_w) \quad (C11)$$

The number of particles in the cloud at one interval Δz and one interval Δs is estimated by the following equation:

$$Np_{cloud\Delta z,\Delta s} = \frac{V_{cat-cloud\Delta z,\Delta s}}{\frac{1}{6}\pi(\varphi_s d_p)^3} \quad (C12)$$

The volume of solids in the emulsion phase is the emulsion phase volume multiplied by the complement of the emulsion porosity:

$$V_{cat-emulsion} = V_e \cdot \epsilon_{sd} \quad (C13)$$

The number of particles in emulsion phase is the volume of solids in the emulsion phase divided by the volume of a single particle:

$$Np_{emulsion\Delta z} = \frac{V_{cat-emulsion}}{\frac{1}{6}\pi(\varphi_s d_p)^3 N_z} \quad (C14)$$

The molar flow rate of diffusing species to the catalyst particle depends on the catalyst surface, and in the cloud, wake and emulsion zones, the catalyst surface is the number of particles in such zone multiplied by the surface of a single particle:

$$S_{catwake} = Np_{wake} \cdot \pi(\varphi_s d_p)^2 \quad (C15)$$

$$S_{catcloud} = Np_{cloud\Delta z,\Delta s} \cdot \pi(\varphi_s d_p)^2 \quad (C16)$$

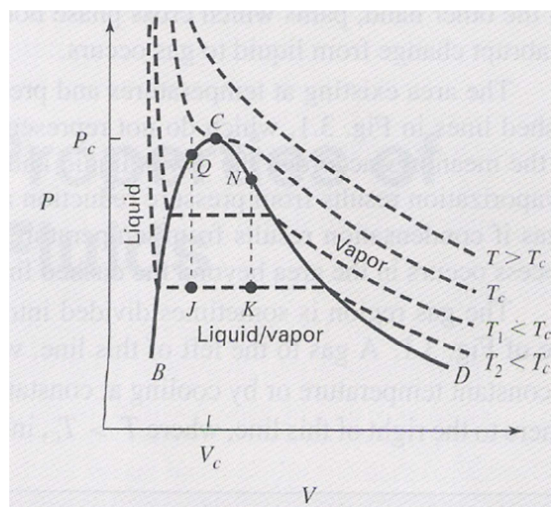
$$S_{catemulsion} = Np_{emulsion\Delta z} \cdot \pi(\varphi_s d_p)^2 \quad (C17)$$

APPENDICE D – Thermodynamics

Heat and work necessary to perform important tasks in industrial processes, such as heating, cooling, gas compression and so on, are calculated by thermodynamic properties, such as enthalpy and entropy. Thermodynamic properties are calculated based on molar volume as function of temperature and pressure, the so called PVT behavior (P for pressure, V for volume and T for temperature). PVT behavior is mathematically described by expressions called *Equations of State (EOS)*.⁷¹

The Pressure-Volume (P V) diagram, figure D1, shows a two-phase region, described by the vapor pressure curve (solid curve). This zone represents the co-existence of liquid and vapor phases. At left, the liquid zone, and at right, the vapor zone. Liquid shows itself “incompressible” because even for a high pressure change, the volume change is almost negligible. On the curve shown in figure A1, at the point Q the fluid is *saturated liquid*, while at the point N the fluid is *saturated vapor*. At points J and K the fluid is a mixture of saturated liquid and saturated vapor, however, at point J there is more liquid than vapor, and at point K there is more vapor than liquid. The mass fraction of saturated vapor of the fluid inside the two-phase zone is called *Quality* of the vapor. Point C is the *critical point*, where liquid and vapor phases are indistinct, with T_c and P_c the critical temperature and pressure respectively.

Figure D1 – General PV diagram for a pure substance.



Source: Smith, Van Ness and Abbott (2001).⁷¹

At the temperature of 0°C (273 K), the product of the multiplication between pressure and volume for all gases ($P \cdot V$) tends to a limit value of 22711.8 cm³ bar mol⁻¹ when pressure approaches zero. As the pressure gets approximate zero, gas molecules are separated by infinite distances, in a way that its volume is not significant in comparison to the total gas volume and the long distances between molecules turn the intermolecular forces negligible. All gases in such condition is called *ideal gas*.⁷¹

$$R = \frac{(P \cdot V)_{lim}}{273} \quad \therefore \quad R = 83.14 \frac{cm^3 bar}{mol K} \quad (D1)$$

The equation of state which describes the ideal gas behavior is called *ideal gas equation of state*:

$$P = \frac{n \cdot R \cdot T}{V} \quad (D2)$$

The approximation of ideal gas is in many cases good, being very used in many practical situations and has higher accuracy as higher the temperature, in relation to the critical temperature, and as lower the pressure, in relation to the critical pressure. However, the critical point is sometimes not simple to find for a mixture of gas or liquid, so, ideal gas behavior is usually assumed plausible at high temperature and low pressure.⁷²

Cubic equations of state are the simplest equations capable of representing liquid and vapor behavior.⁶³ Therefore, these equations are the most utilized to represent real fluid. The first cubic EOS developed was the Van der Waals equation, equation (D3), developed by Johannes Diderik Van der Waals in 1873 and was based on the volume occupied by molecules and the interaction forces between them.⁷³

$$P = \frac{RT}{\bar{V} - b} - \frac{a}{\bar{V}^2} \quad (D3)$$

$$a = \frac{27}{64} \cdot \frac{R^2 T_c^2}{P_c} \quad (D4)$$

$$b = \frac{1}{8} \cdot \frac{R T_c}{P_c} \quad (D5)$$

In equation (D3), P is the pressure (Pa), T is the temperature (K), R is the ideal gas constant (Pa m³ mol⁻¹ K⁻¹), \bar{V} is the molar volume (m³ mol⁻¹), b is the molecular

volume ($\text{m}^3 \text{mol}^{-1}$) and a is the attractive parameter ($\text{Pa m}^6 \text{mol}^{-2}$). In equations (D4) and (D5), T_c and P_c are the critical temperature and pressure respectively.

A more accurate EOS based on Van der Waals was developed by Otto Redlich and Joseph Neng Shun Kwong in 1949, the Redlich-Kwong equation, equation (D6).⁷⁴

$$P = \frac{RT}{\bar{V} - b} - \frac{a}{T^{0.5} \cdot \bar{V} \cdot (\bar{V} + b)} \quad (\text{D6})$$

In order to improve the predictions of Redlich-Kwong EOS for Vapor-Liquid Equilibrium (VLE), an Italian-man called Giorgio Soave proposed in 1972 a modification, considering the attractive parameter as function of temperature. Soave's modification also included a parameter called *acentric factor* (ω). The equation is nowadays known as Soave-Redlich-Kwong (SRK) EOS.⁷⁵

$$P = \frac{RT}{\bar{V} - b} - \frac{a(T)}{\bar{V} \cdot (\bar{V} + b)} \quad (\text{D7})$$

$$a(T) = a_c \cdot \alpha(T_r) \quad (\text{D8})$$

$$\alpha(T_r) = [1 + \alpha_{SRK} \cdot (1 - T_r^{0.5})]^2 \quad (\text{D9})$$

$$\alpha_{SRK} = [1 + (0,480 + 1,574\omega - 0,176\omega^2)(1 - T_r^{0.5})]^2 \quad (\text{D10})$$

$$a_c = 0.42748 \cdot \frac{R^2 T_c^2}{P_c} \quad (\text{D11})$$

$$b = 0.08664 \cdot \frac{RT_c}{P_c} \quad (\text{D12})$$

In equation (D9), T_r is the reduced temperature (-). Reduced temperature and reduced pressure are defined as the quotient of the variable (temperature or pressure) by the critical value:

$$T_r = \frac{T}{T_c} \quad (\text{D13})$$

$$P_r = \frac{P}{P_c} \quad (\text{D14})$$

A more accurate EOS was proposed by Ding-Yu Peng and Donald Robinson in 1976, known as the *Peng-Robinson EOS* (PR).⁷⁶

$$P = \frac{RT}{\bar{V} - b} - \frac{a(T)}{[\bar{V} + (1 - \sqrt{2})b] \cdot [\bar{V} + (1 + \sqrt{2})b]} \quad (\text{D15})$$

$$a(T) = a_c \cdot \alpha(T_r) \quad (\text{D16})$$

$$\alpha(T_r) = [1 + \alpha_{PR} \cdot (1 - T_r^{0.5})]^2 \quad (D17)$$

$$\alpha_{PR} = [1 + (0,37464 + 1,54226\omega - 0,26992\omega^2)(1 - T_r^{0.5})]^2 \quad (D18)$$

$$a_c = 0,45724 \cdot \frac{R^2 T_c^2}{P_c} \quad (D19)$$

$$b = 0,07779 \cdot \frac{R T_c}{P_c} \quad (D20)$$

PR model provides VLE results similar than the ones provided by SRK model. However, for liquid phase it provides better predictions.⁷⁷

The generic cubic equation of state has the following form:

$$P = \frac{RT}{(V - b)} - \frac{a(T)}{(V + \varepsilon b)(V + \sigma b)} \quad (D21)$$

With parameters:

$$a(T) = \Psi \alpha(T_r) \frac{R^2 T_c^2}{P_c} \quad (D22)$$

$$b = \Omega \frac{R T_c}{P_c} \quad (A23)$$

All parameters for the generic cubic EOS are found in the table (D1) and equations (D22) and (D23).

Table D1 – Parameter for the generic cubic EOS.

Equação	$\alpha(T_r)$	σ	ε	Ψ	Ω
VdW	1	0	0	27/64	1/8
RK	$T_r^{-0.5}$	1	0	0,42748	0,08664
SRK	α_{SRK}	1	0	0,42748	0,08664
PR	α_{PR}	$1 + \sqrt{2}$	$1 - \sqrt{2}$	0,45724	0,07779

Source: Smith, Van Ness and Abbott (2001).⁷¹

For multicomponent mixtures, the parameters $a(T)$ and b are calculated by empirical expressions proposed to relate mixture parameters to pure-species parameters. Such expressions are called *mixing rules* and the simplest ones are a linear mixing rule for b and a quadratic mixing rule for $a(T)$ ⁷¹, described by equations (D24) and (D25).^{71, 78}

$$a(T) = \sum_i \sum_j y_i y_j a_{ij} \quad (D24)$$

$$b = \sum_i y_i b_i \quad (D25)$$

Parameter a_{ij} is calculated by the so called *combining rule*, equation (A26)^{78, 79}:

$$a_{ij} = (a_i \cdot a_j)^{0.5} (1 - K_{ij}) \quad (D26)$$

In equation (D26), K_{ij} is the *binary interaction parameter*, an adjustable parameter used to adjust the combining rule to fit more closely to experimental data.⁵⁸ Equations (D24) to (D25) are called Van der Waals mixing rules.^{71, 78}

Although high pressure and low temperature can provide deviations from the ideal behavior, the nature of the chemical substances can also provide. Cubic EOS with Van der Waals mixing rules are satisfactory only for mixtures of simple and chemically similar substances, such as hydrocarbons or hydrocarbons with inorganic gases.^{63, 70} The non-ideal behavior also rises from the interactions between molecules. Rare gases almost do not interact and the presence of heteroatoms in the molecules leads to non-ideal behavior due to the intermolecular forces (hydrogen bonds, dipole-dipole forces, and so on).⁸⁰

Based on such non-idealities originated from chemical structure, in 1986 an EOS for the inclusion of polar substances was developed as modification of the Peng-Robinson equation. It is called *Peng-Robinson Stryjek-Vera* (PRSV), and is based on the modification of the polynomial fit for the acentric factor and the inclusion of a pure-substance adjustable parameter.⁸¹ The model is described by equations (D27) and (D28) substituting the Peng-Robinson model equations (D17) and (D18) respectively.

$$\alpha_{PRSV} = k_p + k_{PRSV} \cdot [1 + T_r^{0.5}](0.7 - T_r) \quad (D27)$$

$$k_p = 0.378893 + 1.4897153 \cdot \omega - 0.17131848 \cdot \omega^2 + 0.0196554 \cdot \omega^3 \quad (D28)$$

The thermodynamic behavior of real fluids is different from the one of ideal gas, because real fluids condense, vaporize, freeze and melt. However, several real fluids behavior as ideal gas under usual process conditions.⁸² Although, many processes occur under conditions that the ideal gas behavior is not valid, such as high pressure or low temperature or both, and the deviation of the ideal gas must be calculated.

Using the generic cubic EOS and performing algebraic manipulations, the calculation of the compressibility factor can be done by the equation (D29) for gas and vapor and by equation (D30) for liquid.⁶³

$$Z = 1 + B - A \cdot \frac{(Z - B)}{(Z + \varepsilon B)(Z + \sigma B)} \quad (\text{D29})$$

$$Z = B + (Z + \varepsilon B) \cdot (Z + \sigma B) \cdot \left(\frac{1 + B - Z}{A} \right) \quad (\text{D30})$$

$$A = \frac{a(T)P}{(RT)^2} \quad (\text{D31})$$

$$B = \frac{bP}{RT} \quad (\text{D32})$$

Equations (D29) and (D30) are solved numerically by the fixed-point (successive substitutions) method described by Wood (1999)⁸³. The initial estimative for the equation (D29) is equal to 1, because this is the value of Z for an ideal gas, and for the equation (D30) is equal to the value of B , from, equation (D32).

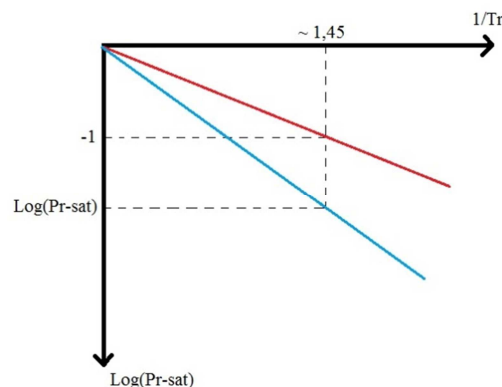
The deviation from the ideal gas behavior can be measured by the compressibility factor Z , which is equal to one for ideal gases and function of temperature, pressure and composition for real fluids.

It is experimentally observed that the decimal logarithm of the reduced saturation pressure (quotient between the saturation pressure and the critical pressure) has a linear variation with the inverse of the reduced temperature.⁸⁴

$$\log P_r^{sat} = S \cdot \left(\frac{1}{T_r} \right) \quad (\text{D33})$$

Different fluids present different angular coefficients S for this line. However, it was noticed that for some simple fluids (such as rare gases), this line inclination is the same, and that for the reduced temperature of 0.7 ($\frac{1}{T_r} \sim 1.45$), the decimal logarithm of the reduced saturation pressure is equal to -1, as shown in figure D2. Therefore, such gases are reference for the definition of the acentric factor.⁸⁴

Figure D2 – Log (Pr-sat) versus (1/Tr).



The acentric factor is defined as the difference, under the reduced temperature of 0.7, between the decimal logarithm of the reduced saturation pressure of the reference gases and of the interest fluid, described by equation (A34).⁸⁴

$$\omega = -1 - \log(P_r^{sat})_{T_r=0,7} \quad (\text{D34})$$

The basic premise of the three-parameter theorem of the corresponding states is that *all fluids having the same value of acentric factor, at the same reduced temperature and reduced pressure, have about the same compressibility factor, and all deviate from ideal gas behavior to about the same degree.*⁷¹

One of the most used generalized correlations based on the theorem of the corresponding states is the Pitzer Correlations for the Second Virial Correlation, described by equations (D35) to (D39):

$$Z = Z^0 + \omega Z^1 \quad (\text{D35})$$

$$Z^0 = 1 + B^0 \frac{P_r}{T_r} \quad (\text{D36})$$

$$Z^1 = B^1 \frac{P_r}{T_r} \quad (\text{D37})$$

$$B^0 = 0,083 - \frac{0,422}{T_r^{1,6}} \quad (\text{D38})$$

$$B^1 = 0,139 - \frac{0,172}{T_r^{4,2}} \quad (\text{D39})$$

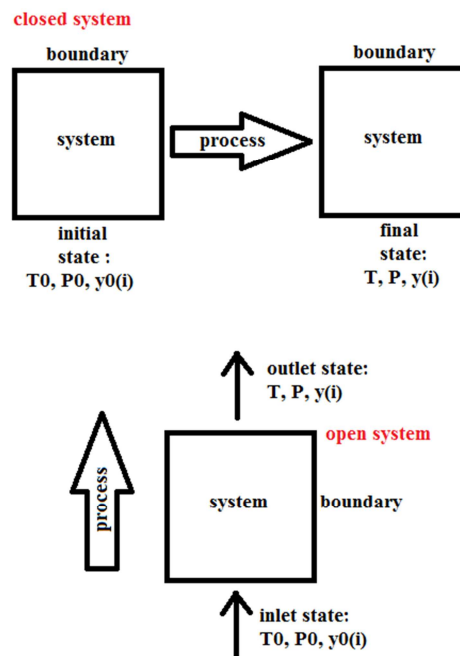
Results from this correlation are not exact, however, for the ranges of temperature and pressure of industrial processes, these results have enough accuracy for engineering calculations.⁷²

The worst pitfall from such correlations is that the knowledge of the critical properties for multicomponent mixture with varying composition (such as the fluid inside a chemical reactor) is somewhat difficult to estimate, and such properties (critical temperature, critical pressure and acentric factor) are essential for the compressibility factor calculation.

A thermodynamic *system* is the control volume with the fluid or fluid-solid set under investigation, which may be *closed* (if no matter is allowed to enter or to exit) or *open* (with flows in and out). The *boundaries* for a closed system is usually only the heat transfer surfaces, and for an open system it is added the inlet and outlet streams, and the *surroundings* is everything out of the system boundaries. The

system properties, such as temperature, pressure, composition and so on, when known, define a thermodynamic *state*, which is described quantitatively by *state functions*. State functions depend only on the current state, and some examples of state functions are the internal energy, enthalpy and entropy. A *state change* occurs when the initial and final (for closed systems) or inlet and outlet (for open systems) states are different, and the way this change is performed in the system is called *process*, and is described quantitatively by *process functions*. Process functions depend on the path the change is done and the best known examples are heat and work.

Figure D3 – Thermodynamic closed and open systems.



The free movement of molecules in the fluid volume implies in constant collisions between them and the boundaries of the system, which provokes forces over these boundaries. Such forces are distributed along the surfaces and this ratio is called *pressure* (P). The molecules can move with more or less intensity, more or less velocity, this implies that molecules have a quantity of energy that allow them to move and such energy is called *internal energy* (U). A qualitative measure of the internal energy is the *absolute temperature* (T), higher temperature more energy. Although, quantitatively, internal energy cannot be directly measured, so its absolute value is unknown. However, if a reference state is adopted, the internal energy change from the reference state to the current state can be calculated.

Heat and work are process functions and represent flows of energy across the system boundaries, one being transferred through a temperature difference (heat, Q) and other being transferred through the action of a mechanical force (work, W), that can be used to change the system volume (expansion or compression work), to transport matter in and out the system (flow work) or to turn a shaft in the system (shaft work).

The first law of thermodynamics says that *the total quantity of energy is constant, and when energy disappears in one form it appears simultaneously in other forms*. This means that the energy variation in a system (represented by changes in state functions) is equal to energy variation in the surroundings (represented by changes in process functions).[van ness]. The mathematical representation of the first law of thermodynamics is known in the engineering field as *Energy Balance*.¹

The differential form of the first law of thermodynamics is the equation (D40):

$$dU = \delta Q - \delta W \quad (\text{D40})$$

Entropy is a state function related to the degree of molecular disorder and its thermodynamic definition is the ratio of the heat transferred by the system temperature, equation (D41).⁷²

$$dS = \frac{\delta Q}{T} \quad (\text{D41})$$

Mathematically, work can be expressed by the product of pressure by volume:

$$W = P \cdot V \quad (\text{D42})$$

So, differential of work results in equation (D43):

$$\delta W = PdV + VdP \quad (\text{D43})$$

Combining equations (D41), (D42) and (D43) and considering a closed system with constant composition, it results:

$$dU = TdS - PdV \quad (\text{D44})$$

Enthalpy (H) is defined as the internal energy plus mechanical work:

$$H = U + P \cdot V \quad (\text{D45})$$

Gibbs energy and Helmholtz energy, equations (D46) and (D47) respectively, are related to the spontaneity of processes.⁷²

$$G = H - T \cdot S \quad (\text{D46})$$

$$A = U - T \cdot S \quad (\text{D47})$$

In differential forms, equation (D45) to (D47) are:

$$dH = TdS + VdP \quad (D48)$$

$$dG = -SdT + VdP \quad (D49)$$

$$dA = -SdT - PdV \quad (D50)$$

Equations (D44), (D48), (D49) and (D50) are called *Fundamental Property Relations*.

71

The fundamental property relations are exact differential, so their cross partial derivatives, according to the Schwarz's theorem, must be equal, and this leads to the Maxwell's Relations:

$$\left(\frac{\partial T}{\partial V}\right)_S = -\left(\frac{\partial P}{\partial S}\right)_V \quad (D51)$$

$$\left(\frac{\partial T}{\partial P}\right)_S = \left(\frac{\partial V}{\partial S}\right)_P \quad (D52)$$

$$\left(\frac{\partial S}{\partial V}\right)_T = \left(\frac{\partial P}{\partial T}\right)_V \quad (D53)$$

$$-\left(\frac{\partial S}{\partial P}\right)_T = \left(\frac{\partial V}{\partial T}\right)_P \quad (D54)$$

With these relations, state function can be expressed as functions of temperature and pressure.

Enthalpy as a function of temperature and pressure is:

$$H = f(T, P) \quad (D55)$$

$$dH = \left(\frac{\partial H}{\partial T}\right)_P dT + \left(\frac{\partial H}{\partial P}\right)_T dP \quad (D56)$$

The term $\left(\frac{\partial H}{\partial T}\right)_P$ is defined as heat capacity at constant pressure and means the energy need to change a specified quantity of matter in one degree of temperature.

$$C_p = \left(\frac{\partial H}{\partial T}\right)_P \quad (D57)$$

Differentiating the fundamental property relation for enthalpy in relation to pressure at constant temperature, it is obtained:

$$\left(\frac{\partial H}{\partial P}\right)_T = T \cdot \left(\frac{\partial S}{\partial P}\right)_T + V \quad (D58)$$

And from Maxwell's Relations, equation (D54) is inserted in equation (D58) and result in:

$$\left(\frac{\partial H}{\partial P}\right)_T = V - T \cdot \left(\frac{\partial V}{\partial T}\right)_P \quad (D59)$$

And combining equations (D59), (D57) and (D56):

$$dH = C_p dT + \left[V - T \cdot \left(\frac{\partial V}{\partial T} \right)_P \right] dP \quad (D60)$$

Equation (D60) is used to calculate the enthalpy change from a state to other. The first term of the right side is the ideal gas enthalpy and the second is the departure enthalpy. When the ideal gas EOS is used to substitute the volume, the pressure-dependent term becomes zero and only the temperature-dependent term rest. So, for an ideal gas, the enthalpy change can be calculated by:

$$dH = C_p dT \quad (D61)$$

$$H^{ig} = \int_{T_{ref}}^T C_p dT \quad (D62)$$

For ideal gas multicomponent mixture, the specific heat capacity ($\text{J mol}^{-1} \text{K}^{-1}$) can be calculated by a mean specific heat capacity:

$$C_p = \sum_i n_i C_p(i) \quad (D63)$$

In equation (D63), n_i is the number of moles of the i -th substance in the mixture, and $C_p(i)$ is the specific heat capacity of the i -th substance. Specific heat capacity of ideal gas usually is expressed by empirical equations with coefficients fit for several substances. Therefore, for an ideal gas mixture in an open system, the enthalpy is calculated by:

$$\dot{H}^{ig} = \sum_i F_i \int_{T_{ref}}^T C_p(i) dT \quad (D64)$$

In equation (D64), F_i is the molar flow rate of the i -th substance.

Departure enthalpy accounts for non-idealities, and for a generic cubic EOS, it is developed as:

$$H^{dep} = RT \cdot (Z - 1) + \frac{T \cdot \frac{da(T)}{dT} - a(T)}{b \cdot (\sigma - \varepsilon)} \ln \left[\frac{Z + \sigma B}{Z + \varepsilon B} \right] \quad (D65)$$

$$\frac{da(T)}{dT} = \sum_i \sum_j y_i y_j \frac{da_{ij}}{dT} \quad (D66)$$

$$\frac{da_{ij}}{dT} = 0.5 \cdot (1 - K_{ij}) \cdot \left(a_j \cdot \frac{da_i}{dT} + a_i \cdot \frac{da_j}{dT} \right) \quad (D67)$$

$$\frac{da_i}{dT} = ac_i \cdot \frac{d\alpha(T_r)}{dT} \quad (D68)$$

$$ac_i = \Psi \cdot \frac{R^2 T_{ci}^2}{P_{ci}} \quad (D69)$$

$$\frac{d\alpha(T_r)}{dT} = f(EOS) \quad (D70)$$

$$H(T,P) = H^{ig} + H^{dep} \quad (D71)$$

For cases which the ideal gas approximation is plausible, the equation (D64) is used, and for cases of high pressure, which ideal gas is not applicable, the equation (D65) to (D71) must be used to calculate the real gas enthalpy.

Chemical reactions can be carried out in many different conditions, and tabulation of heat effects for all such conditions is impossible. So, heat effects of chemical reactions in several conditions are calculated from data for reactions occurring in a standard condition, which is usually 25°C and 1 atm. Heats of reaction calculated at standard conditions are called *Standard Heats of Reactions* (ΔH_{298}°). Standard heats of reaction are calculated from *Standard Heats of Formation* ($\Delta H_{f,298}^\circ$).⁷¹

$$\Delta H_{298}^\circ = \sum_i v_i \Delta H_{f,298,i}^\circ \quad (D72)$$

In equation (D72), v_i is the stoichiometric coefficient for the i -th substance which is present in the chemical equation.

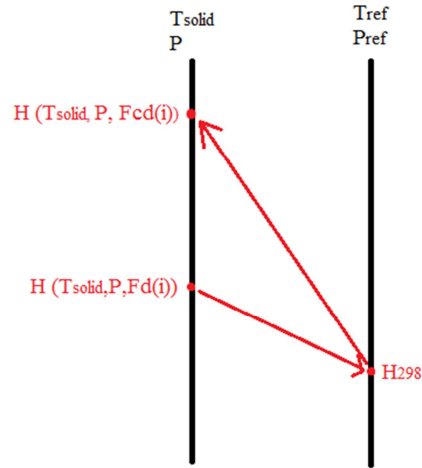
Although industrial reactions seldom are carried out under standard conditions, initial and final temperature are usually different, usually excess of reactants are used, multiple chemical reactions are often, and many other features of real world is present, calculation of heat effects is still based on the standard heat of reaction. However, enthalpy calculations must be performed.

For a reactant mixture in conditions of temperature and pressure different from the standard conditions, it is necessary to calculate the energy required to take it to the standard conditions, through enthalpy change from the current state to the standard temperature and pressure. Next, the chemical reactions are performed at the standard conditions and therefore the energy involved is ΔH_{298}° . After products are formed, the enthalpy change from standard temperature and pressure to the final state is calculated.

For the model proposed in this work, after adsorption of reactants on the catalyst surface, substances stay in equilibrium with solid and the molecules temperature is the solid temperature, so the initial temperature is also the solid

temperature (T_{solid}) and pressure is the bed pressure at the current height. After reactions, the products are also at solid temperature and pressure of current height.

Figure D4 – Calculation path for heat of reactions.



$$H_{rxn} = \Delta H_{298}^{\circ} - H_{reactants} + H_{products} \quad (D73)$$

$$H_{reactants} = H(T_{solid}, P_z, F_d(i)) \quad (D74)$$

$$H_{products} = H(T_{solid}, P_z, F_{cd}(i)) \quad (D75)$$

Equation (D73) is the one used in this work to calculate enthalpy change.

APPENDICE E – VBA program structure

The model developed in this thesis was implemented in VBA and coupled in Aspen Plus™ by a Microsoft Excel template spreadsheet. Excel spreadsheets contains tables, called *Worksheets* or simply *sheets*, with cells addressed by rows (identified by numbers) and columns (identified by letters), and the sheets contained in a spreadsheet are usually identified by numbers, e.g., Sheet 1, Sheet 2, and so on. Aspen Plus™ template spreadsheet, after first run into the flowsheet (as procedure described on chapter 5), writes in the spreadsheets at least four sheets, called respectively *Aspen_Input* (with data from the inlet streams connected to the user module), *Aspen_IntParams* (with integer parameters), *Aspen_RealParams* (with decimal parameters), and *Aspen_Output* (with data to be read by Aspen Plus™ after user module is run).

The code for the Bubbling Fluidized Bed Reactor consists of functions and subroutines programmed inside modules. The modules contained in VBA code are: *AspenHooks*, *Reactor*, *ReactorGeometry*, *Fluidization*, *FluidDynamics*, *HeatAndMassTransfer*, *SolidsDistribution*, *Kinetics*, and *Thermodynamics*.

Module *AspenHooks* contains several functions and subroutines. However, the most important are the function *ahGetValue* (used to retrieve data from the sheet cells), function *AspenCalculate* (used to call the main reactor subroutine) and subroutine *ahSetValue* (used to write data on sheet cells). Function *ahGetValue* has the following syntax:

$$\text{variable_name} = \text{AspenHooks.ahGetValue}([\text{sheet_name}], i, j)$$

sheet_name may be *Aspen_Input*, *Aspen_IntParams* or *Aspen_RealParams* according to the sheet the data to be assigned is from. *i* and *j* are integer number describing the row and column of the cell which the data is available for input. When Aspen Plus™ writes sheets, the first column does not contain data to be retrieved. However, column number *j* must be counted as one for column two, two for column three and so on.

Data is written on sheet cells by subroutine *ahSetValue* with the following syntax:

Call AspenHooks.ahSetValue([Aspen_Output], i, j, variable_name)

Statement *call* is used to call subroutines to run. Letters *i* and *j* indicates the row and column numbers respectively, with *j* counting as one to column two, two for column three, and so on. And finally, *variable_name* is the name of the variable whose value will be written on the cell at row *i* and column *j* in the sheet *Aspen_Output*. Inside the function *AspenCalculate*, the main reactor module is called by the following statement:

Call Reactor.reactor_subroutine_name()

reactor_subroutine_name is the name for the reactor programmed subroutine, which reads input data from sheets by *ahGetValue* function, performs calculations by calling functions from other modules following the model described in chapter 4, writes output data on *Aspen_Output* sheet by subroutine *ahSetValue* and is located in the *Reactor* module.

All other modules contains functions and numerical procedures described on previous chapters and appendices, and are grouped according to their scope (function to calculate bubble diameter is located in the *Fluidization* module, function to calculate enthalpy is located in the *Thermodynamics* module, function to calculate mass transfer coefficient is located in the *HeatAndMassTransfer* module, and so on). Such functions located in other modules can be called by the following general statement:

variable_name = module_name.function_name (list of parameters)

In order to simulate the same reactor modeled in this thesis with a different set of reactions and a different set of chemical species, it is necessary to change species parameters (critical temperature, critical pressure, acentric factor, binary interaction coefficients, etc.) in *Thermodynamics* module, and change kinetics parameters (pre-exponential factors, activation energies, temperature exponents, etc.) and kinetic models (power law, Langmuir-Hinshelwood, Eley-Rideal, etc.) in *Kinetics* module.